Perylene Diimide Derived Nanofibres and their Applications

Thesis submitted in accordance with the requirements of
The University of Liverpool
for the degree of
Doctor in Philosophy
By Alexandra Ho

30th July 2020

UNIVERSITY OF LIVERPOOL

Abstract

This thesis describes the synthesis and supramolecular structural directing methods of a perylene diimide derivative (PDI) for applications in aqueous metal-ion sensing and as a precursor for carbon nanofibres as electrode materials for supercapacitors. Perylene diimide derivatives are receiving increasing attraction due to their thermal stability and chemical inertness as well as their interesting electronic properties. Initially used as industrial grade pigments, more recent applications make use of its n-type semi-conductivity which rises due to the high electron affinity of rylene dyes.

In order to exploit their interesting potential applications, the initial insolubility of perylene-based molecules requires modification through substitution with primary amines (N-substitution). The soluble PDI was investigated for its susceptibility to pH-triggered self-assembly into fibres as well as fibre production through electrospinning using polyethylene glycol as a carrier polymer. Collected fibres could be carbonized at 800°C yielding carbon nanofibres (CNFs).

PDI which could be dissolved in alkali aqueous conditions was sensitive to the presence of metal ions through UV-Vis absorbtion techniques. Dilute solutions of metal salts were added in microlitre-scale increments to cuvettes filled with PDI solution to record the UV-Vis response. PDI solutions provided a turn-off fluorescent sensor which was sensitive to the presence of metal cations within solution at low concentrations (2.5 nM) for iron (III) and copper (II) solutions. Further investigation is required into the effect of counter-ions.

CNFs produced from ordered PDI molecules were assembled as an electrode for cyclic voltammetry capacitance testing. Using polyvinylidene fluoride (PVDF) as a binder in N-methyl pyrrolidone (NMP), CNFs were adhered to a carbon electrode surface and cycled in an acid, alkali, and neutral electrolyte. Brunauer Emmett Teller analysis showed

microporous materials with surface areas ~300$m^2.g^{-1}$ and Raman spectroscopy was employed using I_D/I_G ratios as a measure of degree of graphetisation. Supramolecular CNFs demonstrated capacitances up to 247 $F.g^{-1}$ (1 $mV.s^{-1}$) while CNFs produced through electrospinning gave capacitances up to 427 $F.g^{-1}$ (1 $mV.s^{-1}$). Both materials demonstrated pseudocapacitive behaviour rather than that of pure electrochemical double-layer.

Acknowledgements

Firstly, I would like to thank my supervisors Dr. Haifei Zhang and Dr. Li Xu for their unending patience and compassion. Dr. Li provided excellent ideas and a consistent presence despite his own struggles and Haifei provided support when I needed it and freedom to explore ideas otherwise. I would also like to mention the wonderful research groups from both Liverpool and A*STAR. Ming Yan and Siew Yee filled an unfamiliar lab and country with smiles and were both always willing to lend a helping hand. Hripsime, Yonghong, and Dan made the office in Liverpool a much funnier environment than it had any right to be.

Secondly, I would like to mention both Singapore and Liverpool friends alike. Lizzie, Will, Kenny, Lefteris, Dallas, and Bryony, you all kept me sane and social in a foreign country and I hope our friendships continue on. Tish, John and Penny, I couldn't ask for better friends. Sean, you provided company when I was down and the support to get back up, thank you for existing. A special thanks to Uli for her aggressive encouragement to explore and play and work to the fullest capacity, you are a lifelong friend and I will come to bother you in any country you end up in. Josh deserves unique thanks for providing an ear to listen as well as helping hands when I needed them most. Your steadfast commitment and support is a gift I cherish.

Finally, I'd like to thank my parents and sister, Elizabeth. Mum, Dad, you've never pushed me to do anything, but you set an example of what hard work, intelligence, and perseverance can achieve. I'm grateful for everything you sacrificed so that I could get to where I am today, thank you.

Nomenclature

BC – Bacterial Cellulose

BET – Brunauer Emmett Teller

BJH – Barrett Joyner Halender

CHNX – Elemental Analysis

CMC – Critical Micelle Concentration

CNF – Carbon Nanofibre

CS – Coronene Tetracarboxylate

CVD – Chemical Vapour Deposition

DMF – Dimethyl Formamide

DMSO – Dimethyl Sulfoxide

DMV – Dodecyl Methyl Viologen

EDLC – Electric Double-Layer Capacitor

(FE)SEM – (Field Emission) Scanning Electron Microscopy

FTIR – Fourier-Transform Infrared Spectroscopy

FWHM – Full-Width Half Maximum

GA – Gluteraldehyde

GdL – Gluocono-δ-Lactone

Hb – Haemoglobin

HOPG – Highly Ordered Pyrolytic Graphite

MOF – Metal-Organic Framework

NMP – N-Methyl Pyrrolidone

NTR – Nitroreductase

PAN – Polyacrylonitrile

PBI – Perylene Bisimide Derived Molecule

PCL – Polycaprolactone

PDI – Perylene Diimide Derivative

PEDOT – Poly(3,4-ethylenedioxythiophene)

PEG/PEO – Polyethylene Glycol/Oxide

PET – Polyethylene Terephthalate

PLA – Polylactic Acid

PMMA – Poly(Methyl Methacrylate)

PSS – Polystyrene Sulfonate

PTCDA – Perylene Tetracarboxylic Acid Dianhydride

PVA – Poly(Vinyl Alcohol)

PVDF – polyvinylidene fluoride

S/MWCNT – Single-/Multi- Walled Carbon Nanotubes

THF – Tetrahydrofuran

Contents

Chapter 1 Introduction

Synthetic polymers are conventional macromolecules that permeate our everyday life as well as our technology. They consist of small molecules connected by covalent bonds to form extended structures. While these materials have many uses, they also have their own downsides, including difficulty of degradation, which can affect potential toxicity issues in biocompatible applications.

Supramolecular chemistry has shown itself capable of constructing macromolecules of greater variety using building blocks of almost any size, connected through non-covalent linkages such as; hydrogen bonding, and electrostatic interactions. Living systems are known to incorporate supramolecular structures within key areas such as; cell cytoskeletons, in which proteins fold and unfold dynamically within a membrane; as well as the reversible formation of hydrogen bonds within DNA double helices for transcription and translation of genes.

Perylene Diimide Derivatives (PDIs) are multi-aromatic molecules with an extended π system and are utilised in many fields including sensing,[1–22] light-emitting diodes,[23–27] and pigments.[28–30] Due to the strong hydrophobicity of perylene modifications must be made to the molecule to facilitate use in conventional chemical processes. These modifications can be achieved using methods covered in the next section.

1.1 Molecular Synthesis

Chemical and physical properties of PDIs can be altered significantly through three main routes. Side-group functionalisation at the N,N' imide positions, "bay" (1, 6, 7, 12) positions and also "ortho-" (2, 5, 8, 11) positions. The imide positions are the nodes of the HOMO and LUMO of the molecule thus, substitution at imide positions generally does not

significantly affect the electronic properties of PDIs, maintaining the molecular absorption and emission features. Due to the planarity of perylene molecules and their localised aromatic electron density cloud, aggregation is favoured and molecules are highly insoluble. To facilitate usage in more conventional chemical methods, substitution at the imide positions affects the aforementioned planarity of the molecules and thus N,N' substituted analogues show largely different solubilities.

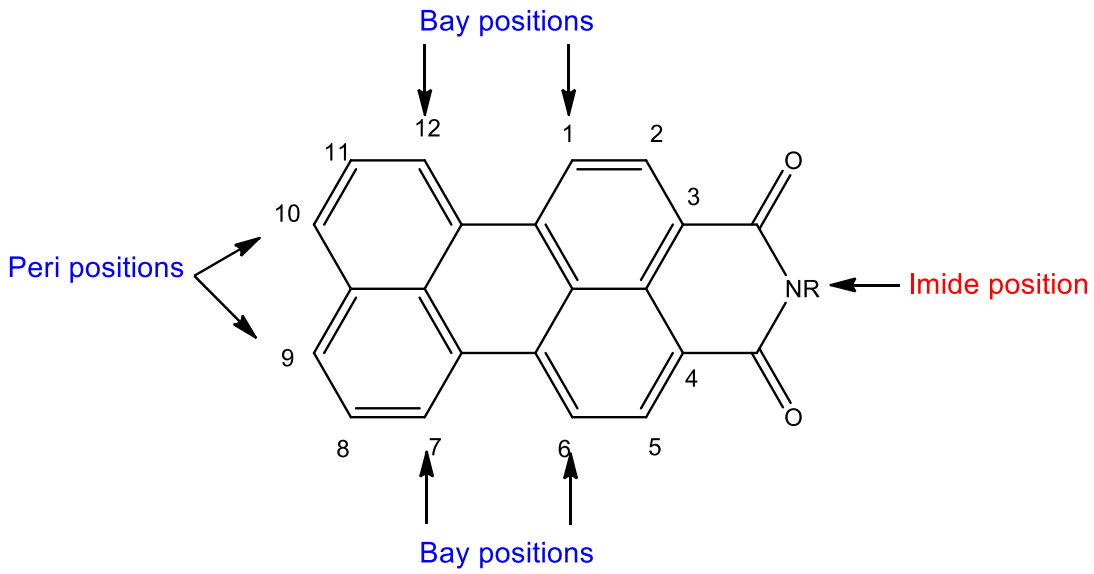

Figure 1.1 Perylene diimide functionalisation positions

In a typical N,N' side chain substitution at the imide position (**Figure 1.1**), commercially available perylene tetracarboxylic acid dianhydride (PTCDA) reacts with primary amines in a high-boiling point solvent (e.g. imidazole or, quinoline).[31,32] Direct imidization is possible with higher yields generally feasible from aliphatic amines than that of aromatic amines. Asymmetric imidization is possible using an asymmetric precursor, perylene monoanhydride monoimide.

Bay-substitution, however, results in changes in the optical and electronic properties of PDIs, as well as significantly disturbing the self-assembly of molecules. This is mostly due to steric effects of substituents which twist the planarity of the central π-system, limiting the crystal packing behaviour induced by π-π stacking.[31,32] Substitution at these positions has

garnered increased interest due to the potential tuning of electronic properties as well affecting their solubility which makes working with these molecules much easier.

1.2 Self-Assembly

Gels were defined by John Ferry (1980) as substantially dilute cross-linked systems which exhibit no flow when in the steady state.[33] The skeleton formed in such gels may be maintained after removal of solvent under supercritical conditions since pores in the gel are free from capillary forces leaving behind porous, ultralight materials which have extremely low density and thermal conductivity. If a nanofibrous gel can be formed, it is possible to produce a 3-dimensional carbon nanofibrous monolith simply through carbonisation.

In the case of PDI molecules, the core, planar, π-conjugated system is particularly prone to stacking into crystal aggregates that have similar interlayer distances to that of graphite (ca. 3.4Å). PDI aggregation can be monitored in-situ through UV-Vis spectroscopy since monomeric PDI molecules in solution usually have three characteristic vibration absorption peaks within the 400-550 nm range. Molecular aggregation usually presents with a bathochromic (red-) shift in absorption peaks attributed to the J-aggregate nature of the assembly which occurs through π- π stacking.[31,32]

Monitoring of self-assembly of supramolecular structures within a solution may be carried out by comparing the mechanism to that of micelle formation. Since these materials are also supramolecular in nature, observation methods are comparable. A commonly used method of isolating the Critical Micelle Concentration (CMC) uses a water non-soluble fluorescent dye with extremely low absorbance at concentrations lower than the CMC. As the concentration of surfactant is increased, the molecules reach CMC and start to self-assemble. The fluorescent dye which becomes encapsulated by the micelles increases its absorbance and can easily be detected.[34]

Since PDI molecules are mostly fluorescent initially, the aforementioned red-shift in absorption peaks may be used to monitor self-assembly. By measuring spectra while varying parameters such as pH or solvent composition, or by recording the rate of change in specific wavelengths, it is possible to generate a curve which may be split into linear segments which cross at the "CMC". This method also allows us to isolate the point at which the self-assembly has completed.

Balancing the inclination for PDIs to π-π stack against solubility may be enhanced by side chains that are either not bulky or flexible. Interactions between side-chain substituents must also be considered during molecular design, since interactions such as H-bonding or solvent-specific electrostatic interactions can significantly influence molecular self-assembly. For example, linear long-chain alkyl substituents such as dodecyl, and octadecyl, etc., were shown to form 1D nanobelts using phase-transfer assembly.[35,36] PDIs containing branched substituents or those with bulky moieties resulted in shorter and wider 1D nanofibers, i.e. ribbons or rods.[31,37–41] Due to the minimal electronic effect of imide substituents, they can be used to tune and improve solubility as well as π- π stacking arrangements allowing the structure-property relationship of PDI assemblies to be studied.

Tuning the solubility of PDIs is important because the most common method of forming 1D nanostructures from these materials, involves solution-processing, which is capable of forming longer 1D nanostructures than those formed upon crystalline substrates or through template supporting. A majority of techniques require PDI to be soluble in common solvents.

1.2.1 Solvent-Phase Interfacial Self-Assembly

There have been extensive efforts made into exploring solution-phase self-assembly of PDI derivatives at interfaces in order to achieve one-dimensional nanostructures with well-

defined morphology. Alternatives include: Crystallisation which, while providing highly ordered materials, have a low rate of sedimentation which may require days or even weeks to generate such an ordered material; Supramolecular interactions may be used to direct self-assembly between a surface and individual molecules typically in a wet-deposition process. A general disadvantage of this method is that irregular arrays can form due to initially strong attachments between molecules which do not allow correction of errors or mismatching during the assembly process. An important alternative to these methods uses liquid-liquid interfaces which makes use of an oil-water interface where interfacial tension is high and the assembly is highly dynamic which enables errors to be corrected rapidly.[42–45]

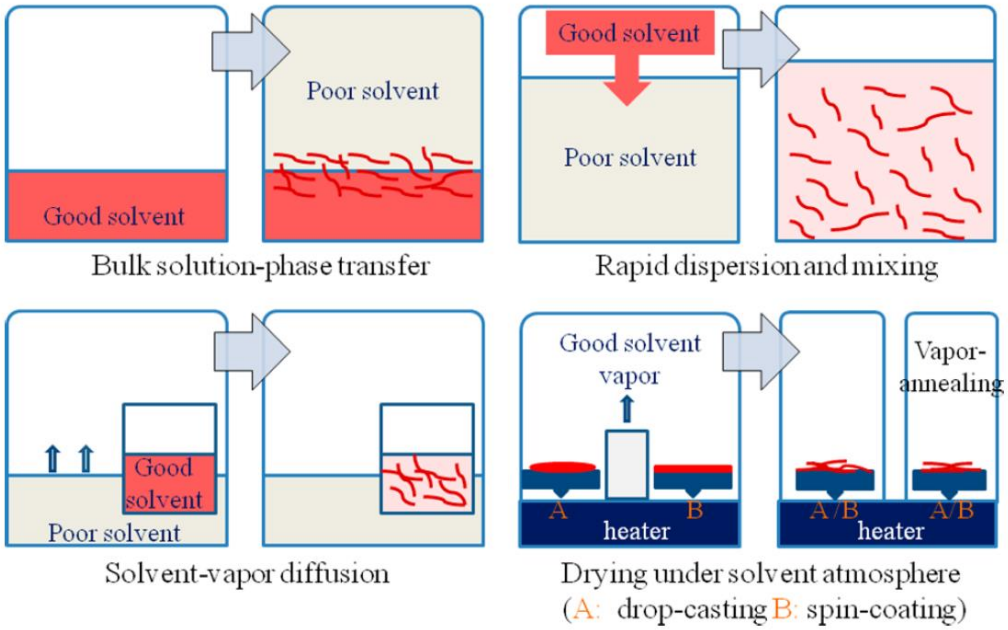

Figure 1.2 Diagrams showing the approaches to relative solvent-phase interfacial self-assembly strategy. Reproduced with permission from Chen. S, et. al.[31] Copyright 2015 American Chemical Society.

Solution processing strategies have since expanded to include a set of approaches depicted in **Figure 1.2** including evaporation-triggered in situ self-assembly on a solid surface, solvent-vapour diffusion, and bisolvent phase-transfer. All of the aforementioned processes involve mass transfer from a good solvent to a poor solvent (or vapour). Solvent components may be optimized and the environmental parameters can be adjusted, (e.g.,

solvent polarity, concentration, pH, temperature, etc.). Good solvents refer to a solvent in which the PDI in question has a high solubility and is usually able to solvate the extended π-conjugated perylene system. Poor solvents refer to those which encourage π-π stacking and/or hydrogen bonding. Successful self-assembly is determined by a balance between solubility of PDI molecules and non-covalent intermolecular interactions.[31]

1.2.1.1 Evaporation-triggered in situ self-assembly

One-dimensional nanofibres can be prepared on appropriate solid substrates, making use of a self-assembly method which balances molecular structure with solvent nature, substrate properties, and post-assembly treatment. Adjusting solvent factors such as volatility, polarity, solubility, and concentration; as well as surface properties including atomic orientation and flatness, provides a tunability to the process which facilitates generation of fibres with different properties.[31]

A study by Grosso, D. et al., shows how evaporation-induced self-assembly can be used to influence mesostructure by adjusting critical parameters which include chemical and processing conditions, the initial sol preparation, and the evaporation.[46] While Tchakalova, et al. detail how evaporation-triggered self-assembly is a hindrance to the fragrance industry, which utilise ethanol-water mixtures, as the non-polar fragrance additives aggregate leading to lower fragrance evaporation.[47]

In 2019 Wu, et al. demonstrated the formation of a microfibrous gel using a ZnO nanofluid, made up of ZnO nanoparticles in a chloroform/methanol/isobutylamine mixed solvent.[48] With solvent evaporation the ZnO nanoparticles underwent a hydration/dissolution reaction with ambient environmental water into layered $Zn(OH)_2$ with isobutylamine intercalated inbetween. The resulting organogel displayed microfibres of width 1-5 μm which further assembled upon lyophilisation to thicker microfibres (2-11 μm) in the xerogel.[48]

1.2.1.2 Solvent-Vapour Diffusion Self-Assembly

An unconventional solvent-exchange crystallisation process was developed by Zang et al. in 2008, which uses a similar approach to bisolvent phase-transfer self-assembly.[35] This vapour diffusion approach was adapted to provide a slower, more controlled crystallisation process. Vapour diffusion solvent exchange is slow enough that gradual and controlled adjustment of the solubility of the molecules can be achieved.[35] Slow decrease in solubility allows for minimal crystalline defects and also allows for molecules with increased branching in their side-chains, to relax into a more favourable configuration for one-dimensional stacking. The speed of solvent exchange is also controllable since it is possible to adjust the temperature, affecting the vapour pressure of the solvents and thus controlling the decrease in solubility of the molecules.

Bai, et al. made use of the nonsolvent vapour method detailed by their group previously to prepare hierarchical microspheres.[49,50] A clean glass slide was placed in a sealed container filled with nonsolved vapour and poly(2,5-dialkoxyphenylene) in solution was dropped onto the glass by microsyringe before allowing the solvent to evaporate leaving behind a thin layer of the self-assembled material. As produced microspheres demonstrated selective Fe^{3+} sensitivity through fluorescent quenching.[49]

1.2.1.3 Bulk Bisolvent Phase-Transfer Self-Assembly

The most generally used method for formation of 1D nanostructures involves the dissolution of PDIs in good solvents and then, through gentle addition of poor solvents to the top of the concentrated solution, allowing interfacial diffusion to occur. As mentioned previously, side-chain substituents greatly influence solubility of PDIs, thus, this method varies depending on side-chain substituents, as to which good and poor solvents to use. While solubility is greatly enhanced by the addition of bulky imide substituents,

substituents that create too much steric hindrance (e.g., 1-nonyldecyl, hexylheptyl) can impede molecular stacking.

A study by Kundu, et al. demonstrated a supramolecular nanofibre as a solid electrolyte. Using coronene tetracarboxylate (CS) and dodecyl methyl viologen (DMV) as alternating donor-acceptor molecules, a cylindrical micelle was formed by injecting DMV in methanol into a pre-prepared aqueous CS solution.[51] The dispersion of nanofibres in solution was drop-cast onto a pair of Ti electrodes and dried, leaving nanofibre bundles across the gap. Using a potential sweep rate of 10 $V.s^{-1}$, an area capacitance of 204 $\mu F.cm^{-2}$ was achieved with a current discharge rate of 3 $mA.cm^{-2}$ which increased with increasing sweep rate up to 268 $mA.cm^{-2}$ at 10 000 $V.s^{-1}$, though there was a predictable decrease in area capacitance to 25 $\mu F.cm^{-2}$.[51]

In 2012, Boobalan, et al. presented highly fluorescent perylene bisimide nanofibres generated using interfacial self-assembly.[36] By substituting PTCDA with 1-dodecylamine, 1D nanofibres were produced by dissolving D-PTCDI in the good solvent, chloroform, and encouraging self-assembly at the interface with the poor solvent, methanol. These fibres were also presented as being able to form highly ordered thin films.[36]

1.2.1.4 pH-Triggered Self-Assembly in Aqueous Solution

As mentioned previously, side chain substituents dramatically affect the solubility of PDIs. Hydrophilic side-chain moieties are usually pH sensitive that is, subject to protonation and deprotonation. As such, self-assembly of these molecules may be triggered by tuning the pH of solutions. The extracellular matrix protein, amelogenin, is formed through self-assembly and plays an important part in the regulation of growth and organisation of enamel crystals during enamel formation. Enamel, unlike bone, does not undergo remodelling after mineralisation and has a structure comprised of bundles of rods of long parallel arrays of calcium phosphate crystals.[52] Research conducted by Wiedemann-Bidlack,

et al. concluded that the self-assembly and formation of higher-order structures of amelogenins *in vivo* is primarily regulated by pH.[53]

PDIs containing carboxylic acid functional groups have presented with this behaviour, Zang, 2013 reported pH-triggered hydrogelation route assembling molecules into well-defined 1D-nanobelts. By N-substitution of 3-aminopropanoic acid, C-PDI-1 was able to be dissolved in aqueous triethylamine, pH ~ 9. With addition of aqueous hydrochloric acid, pH was lowered causing the solution to gradually turn into a solid gel containing fibres 20-30 nm wide.[54] This molecule was later used by Wang, et al. in 2017 as a photocatalyst for degradation of organic pollutants (primarily tested with phenol).[54,55]

1.3 Electrospinning

In electrospinning, polymer nanofibres are formed by the creation and elongation of an electrified fluid jet.[56] It uses an electric potential to draw charged polymer solutions or polymer melts into threads of fibres of the order of hundreds of nanometres. Electrospinning from molten precursors ensures no solvent can be carried over into the final product whereas, solvents may be used during the production of fibres from large and complex molecules which may have prohibitively high melting points. When a sufficiently high voltage is applied to a liquid droplet, the body of the liquid becomes charged and electrostatic repulsion works against surface tension causing the droplet to become stretched. At a critical point, a stream of liquid erupts from the surface of the droplet forming a Taylor cone.

The charge migrates to the surface of the fibre and the mode of current flow changes from ohmic to convective. As the current flow changes, the jet becomes elongated by a whipping process caused by electrostatic repulsion initiated at small bends in the fibre stream until it

is deposited at the grounded collector. This elongation results in thinning of the fibres to the aforementioned nanometre-scale diameters.

Parameters which affect fibre properties include: molecular weight, and molecular weight distribution, as well as the architecture of the polymer. Solution properties; including viscosity, conductivity, and surface tension must be taken into account as well as the applied electric potential, flow rate, and concentration. Since the jet flies through the air towards the collector; the distance between the capillary and collector, as well as ambient parameters including temperature, humidity, and air velocity in the chamber must be taken into consideration. Finally, the motion, and size of the target/collector, and the gauge of the needle must be taken into consideration.

Electrospinning as a technique was first observed in 1897 by Rayleigh, though studied in detail by Zeleny (1914) as electrospraying and Taylor (1969) studied electrically driven jets, laying the groundwork for electrospinning.[57–59] The term electrospinning has come into use relatively recently as a derivative from the term electrostatic spinning.

Despite knowledge of this technique for many years, electrospinning has come into the forefront of scientific focus due to the recent interest in nanotechnology. Electrospinning provides a facile route into fibres on the nano-scale which have a high surface area to mass ratio as a primary characteristic.[56] Presently a number of devices in everyday use, including electrostatic precipitators and pesticide sprayers, work in a similar way to electrospinning that is, making use of strong electrical repulsive forces to overcome the weaker surface tension force in a charged polymer liquid.

Recently, electrospun fibrous mats have been employed as super hydrophobic anti-adhesion membranes used in the repair of tendon injuries. Without a physical barrier, the surgical tenolysis procedure would result in only a temporary return of range of motion due to repeat adhesion of the tendon to the surrounding tissue. Zou, et al. presented a poly-L-

lactic acid (PLA) fibrous mat which incorporated beeswax to encourage the hydrophobic effect, thereby preventing adhesion through tissue migration, while still allowing the exchange of nutrients.[60]

The morphology produced is highly dependent on a combined effect of the electrostatic field and the material properties of the polymer. Charge transport between nozzle tip and collector is linked to the mass flow of the polymer jet caused by the applied voltage.[61] A steep increase in spinning current as a result of increased applied potential can lead to highly beaded structures rather than one-dimensional fibres.[62]

As the conductivity of the solution being electrospun is important, Qin et al. demonstrated that the solution can be adjusted by adding salt to enhance the conductivity and also influence the size of the nanofibres formed.[63] Similarly, the concentration of polymer used greatly affects the morphology of fibres as Chang et al. discovered with capillary break up with too low poly(ethylene oxide) (PEO) concentration using a near-field electrospinning technique, which also highlights the steps that can be taken to reduce the intrinsic instability of electrospinning.[64–66]

There are two standard electrospinning set ups; vertical and horizontal, which may be implemented to achieve different results. A study by Yang, et. at., using PVDF in dimethyl formamide (DMF) at increasing potentials, indicates that vertical electrospinning with the nozzle pointing downwards gives fibres which have thinner diameters, however the size distribution is much greater.[67] Conversely, it is possible to electrospin vertically in an upwards direction giving wider diameter fibres but with a narrow size distribution. Electrospinning horizontally gives fibres distributed between the two aforementioned orientations.

A possible explanation provided for this is that the electric field effect may be strengthened when spinning is conducted in a parallel direction to gravity, resulting in thinner fibres.

Whereas spinning in a direction which is anti-parallel to gravity may weaken the effect of the electric field thereby limiting the extending effect causing thicker fibres. The effect of different electrospinning systems on fibre size distribution was explained as, in the case of gravity acting with the electric field, a larger resultant force between electric field and gravity, thus a bigger disturbance leading to a larger distribution.[67]

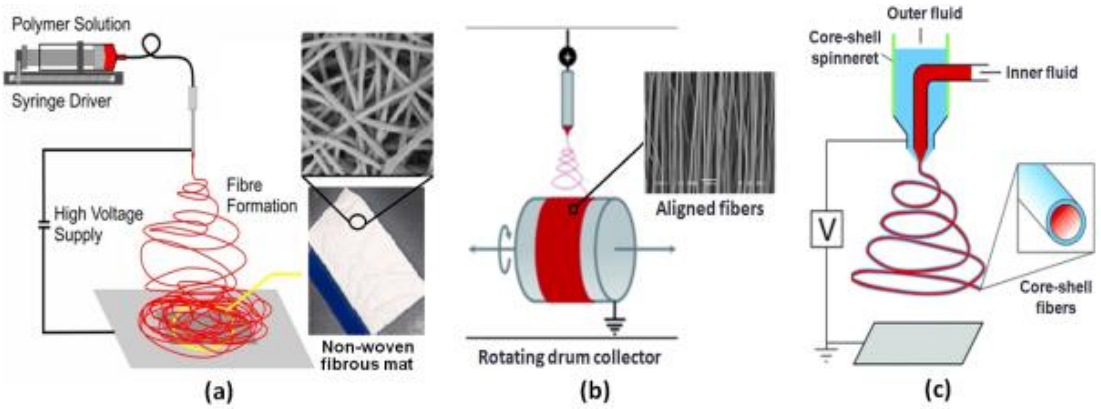

Figure 1.3 Electrospinning set ups to obtain random non-woven fibrous mats **(a)**, aligned fibres **(b)**, and a core-shell spinneret **(c).** Reproduced with permission from Wang. S, et. al.[68]

It is possible to affect the arrangement of fibres by changing the collector at which the fibres arrive. Conventional electrospinning uses a simple flat grounded surface, often aluminium foil which is cheap and easy to remove and replace, and results in non-woven fibrous mats which have found many uses within the medical field[69,70] and food packaging[71,72] applications. Aligned fibres may be obtained through use of a rotating drum collector depicted in **Figure 1.3(b)** which causes fibres to wrap around the drum in one direction.[73–76]

The composition of materials may be expanded to not just purely polymeric fibres. **Figure 1.3(c)** displays coaxial capillaries used to form core-shell fibres. This equipment is useful for encasing a material that would not conventionally spin in a polymer solution which can later be removed through carbonisation leaving behind highly porous fibres.[77–79] Core shell fibres can be produced with a single spinneret by utilising the Kirkendall effect in which diffusion of atoms occurs at carbonisation temperatures.[80,81] The decomposition or

extraction of incorporated pore-forming components (e.g. poly(methyl methacrylate) (PMMA), Pluronic F127, mineral oil, etc.) is another method of obtaining hollow or highly porous carbon nanofibres.[82–84]

Deng, et al. demonstrated co-axial electrospinning using a mixture of multi-walled carbon nanotubes (MWCNTs) and gelatin in trifluoroethanol as the inner solution and a solution of haemoglobin (Hb) in hexafluoroisopropanol as the outer solution.[85] The obtained core-shell nanobelts were cross-linked in gluteraldehyde (GA) vapour. When spun onto a glassy carbon electrode, an electrocatalytic response was demonstrated by the reduction of toxic H_2O_2 with a lower detection limit of 0.0293 μM.[85]

Highly porous fibres can also be produced by spinning cryogenically,[86] and by mixing with metal oxides.[77,87–89] This highlights the most significant advantage of using electrospinning, which is that it becomes facile to incorporate active components (e.g. metal precursors or nanoparticles) or electrically conductive materials (e.g. carbon nanotubes, graphene, etc.) to precursor solutions and fabricate hybrid carbon fibres. Li, et al. presented polycaprolactone (PCL) fibres electrospun onto a cold plate in a vertical electrospinning system resulting in non-woven porous fibre formation.[90] The pores, or pits, were induced by phase separation at freezing temperatures and polygon concaves were formed due to interaction between residual solvent and ice crystals on the surface of the cooled metal collector.[90]

1.4 Carbon Nanofibres

1.4.1 History & Properties of Carbon Nanofibres

The first recorded publication surrounding carbon-based nanofibres (CNFs) is a patent submitted by Hughes and Chambers on the manufacturing of filaments.[91]However, the true

significance of these structures was not fully appreciated until their structure could be analysed through electron microscopy. The first images of carbon nanofibres observed through electron microscopy were obtained by Soviet scientists Radushkevich and Lukyanovich. In 1952, they showed multi-walled carbon filaments 50 nm in diameter formed by carbon monoxide decomposition on an iron substrate.[92] Early research was motivated by the desire to limit their formation as filamentous carbon was considered a nuisance product, often growing and accumulating on metallic catalysts use in petrochemical processing and the conversion of carbon containing gases.

In 1985 buckminsterfullerene, C_{60}, was observed by Kroto et al., a discovery which earned them the Nobel prize in 1997.[93] The discovery was followed by a demonstration by Iijima that carbon nanotubes are formed during arc-discharge synthesis of C_{60}.[94] Two years later Iijima, Ichihashi, and Bethune et al synthesised single-walled carbon nanotubes (SWNTs).[95,96] It was initially suggested that the carbon nanofibres formed through the catalytic chemical vapour deposition method were comprised of a duplex structure, an inner core of amorphous carbon surrounded by graphitic platelets.[97,98] More recently, the structural arrangements of CNFs have been observed to vary significantly when subjected to different reaction conditions including the chemical nature and structure of the catalyst and the composition of the reactants.[99]

As the name suggests, CNFs are defined as nanoscale with respect to their diameters rather than their length. Their small scale provides a promising basis for research into their properties and any modifications that could result in porosity. Multiple processes have since been developed for producing CNFs, aside from chemical vapour deposition (CVD), which provide varying degrees of control over structure, morphology, and dopants, while also providing a potentially greener route for production. These methods include;

controlled freezing/freeze-drying, [100–102] supramolecular self-assembly,[103,104] and electrospinning[79,105,106] of precursor materials followed by carbonisation.

1.4.2 Characteristics

Carbon nanofibres contain hexagonally arranged carbon not-unlike a graphite structure in which each carbon atom is attached to four additional carbon atoms. Carbon atoms within a plane are sp^2 hybridised, with three bonds of length 1.42 Å, while the fourth carbon atom is loosely attached through intermolecular stacking with a distance of 3.35 Å between layers. Delocalised electrons in each carbon layer allow easy transport between units leading to better electrical conductivity. When coupled with large surface area to volume ratios, CNFs are ideal candidates for electrode materials.

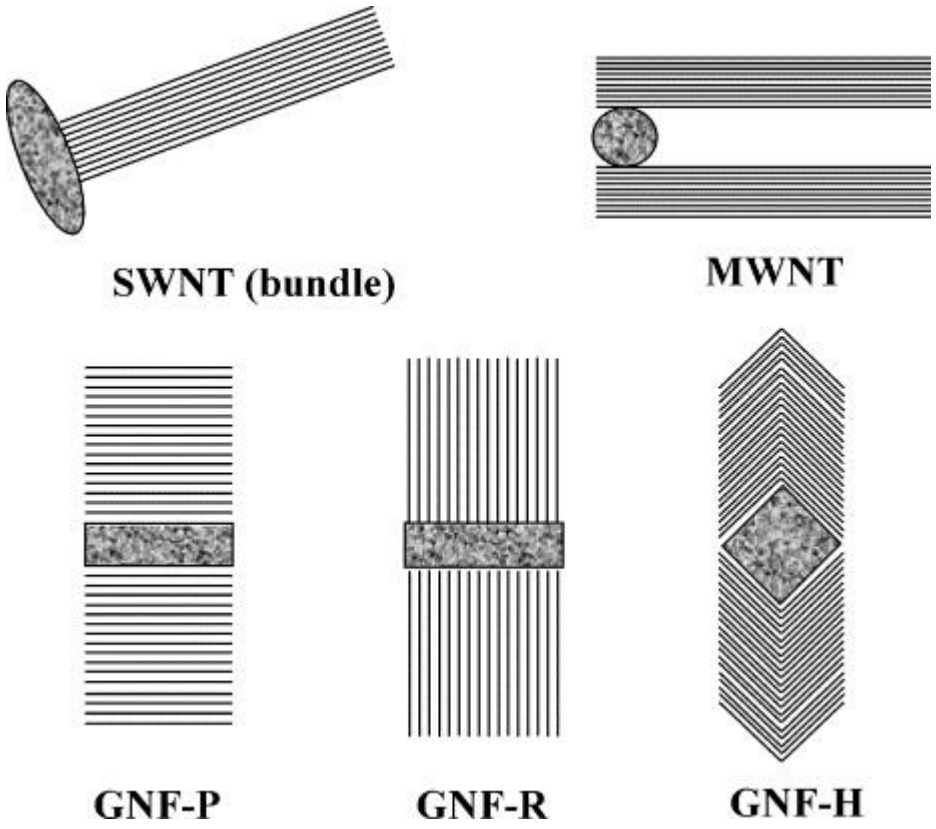

Figure 1.4 Different types of CNFs and CNTs. Reproduced from Serp. P, et. al., with permission from Elsevier Copyright 2003.[107]

There are three main types of CNFs shown in **Figure 1.4**, classified by how their graphene sheets are arranged with respect to the fibre axis. Tubular type CNFs have graphene sheets parallel to the fibre axis while fishbone or herringbone graphene sheets are inclined relative to the axis. Platelet type CNFs have graphene sheets lined up perpendicular to the fibre axis and, like herringbone type CNFs, the surface area is large with exposed edges. Unlike tubular type CNFs, fishbone and platelet type CNFs have visible surface edges with available oxygen groups facilitating interaction with functionalisation materials, making fishbone and platelet type CNFs more prominent material types.[108,109]

Innate chemical inertness of CNFs as well as hydrophobicity encourages functionalising surface groups and can be achieved with oxidising agents. Common oxidising agents, such as HNO_3 incorporate oxygen-containing groups which can provide affixing sites for catalyst particles as well as increasing the acidity and enhancing reactivity of CNFs.[107,108,110,111] Oxidation processes can be conducted in both liquid and gas phase, though better control and homogeneity can be achieved by liquid phase treatment and is preferred over gas phase.[112–114]

1.5 Applications

Table 1.1 Table of materials produced using aforementioned techniques and their applications.

Precursors	Synthetic Conditions	Post-synthetic Treatment	Morphology and Properties	Applications	Ref
ZnO/chloroform-methanol-isobutylamine	Solvent evaporation	Lyophilisation to microfibrillar xerogel	Nanocrystal-organogel Thermo-reversible to 40°C	-	[48]
Poly (2,5,-dialkoxy-phenylene)	Nonsolvent vapour method	-	Hierarchical microspheres	Fluorescent sensing (Fe^{3+})	[49,50]

CS-DMV	DMV/ methanol (10% v/v) injected into aqueous CS	Dropcast onto Ti, dried in vacuo	Cylindrical micelles forming laterally associated fibre bundles	Planar supercap. Voltage window 8 V, 9.5 mF.cm^{-2}	[51,115]
PDI/1-dodecylamine	Interfacial self-assembly chloroform-methanol	Spin coating on glass	Highly ordered uniform thin films	-	[36]
PDI/N-propanoic acid	N-sub of PTCDA with 3-amino-propanoic acid	pH-triggered TEA (834 µL) HCL (27.3 mL, 4.0 M)	H-type π-π stacking into nanofibres	Photo-catalyst for organic pollutants	[54,55]
Bacterial Cellulose/PAN	Solvent exchange, gel phase separation, lyophilisation	200°C, air, 3h, 230°, 6h, activation. Carbonisation 1000°C, CO_2/Ar, 1h	Activated Carbon	Electrode material in EDLC	[116]
Furfuryl alcohol mesoporous silica	Impregnate silica templates, dry at 100°C, 6h	350°C, N_2, 2h. carbonisation at 650, 700 and 900°C, N_2, 2h.	Ordered mesoporous carbon	Electrode material in EDLC, 78 F.g^{-1}	[117]
$FeCl_3$/$NiCl_2.6H_2O$/ Carbon Textile	Hydrothermal autoclave, 100°C, 16-20 h	Calcination 350°C, 2 h	Mesoporous nanocone forest on carbon textile	Flexible supercap. 697 F.g^{-1} (5 mV.s^{-1})	[118]
Graphene oxide/aniline/β-cyclodextrin	One-pot hydrothermal reduction 180°C, 3 h	-	Carbon nanodot-decorated Graphene/ polyaniline composite	Electrode material supercap. 871 F.g^{-1}	[119]
Anthocyanin dye	Extracted from purple sweet potatoes	-	Dye	pH sensor	[120]
PBI/di-isopropylphenyl/ 2-phenylimidazole	N,N'-substitution, bay substitution	-	Dye	pH sensor	[7]
PET	Heavy ion irradiation (Au)	Etching (NaOH/ HCOOH/KCl)	Conical PET nanopore	Protein detection	[121]
Cyanine fluorophore	Organic synthesis	-	Fluorescent probe	Nitro-reductase detection	[122]
$ZrOCl_2$/$CuSO_4$/ BDC	Hydrothermal 150°C, 72 h	-	MOF	Turn on/off fluorescent sensor Pb^{2+}	[123]

Na_2MoO_4/ thioacetamide/ diaminobutane	Hydrothermal 200°C, 24 h	Water dialysis, 1kDa membrane, 48 h	Quantum dots	Turn off Pb^{2+} fluorescent sensor	[52]
PCL	7.5 kV, 0.8 $mL.h^{-1}$ cryogenic collector	-	Porous nanofibres	-	[90]
PLA/Beeswax	Omitted potential, 0.5 $mL.h^{-1}$	-	Super hydrophobic fibrous mats	Peritendinous anti-adhesion	[60]
MWCNT/Gelatin/ Hb	20 kV, 0.6 $mL.h^{-1}$	25% GA, 2 h	Core-shell nanofibres	Biosensor for H_2O_2	[85]
PEO-PMMA/ Chloroform-acetone	10 kV 0.4 $mL.h^{-1}$	Dipped in 60°C deionised water for weeks	Surface roughened PMMA nanofibres	Organic light-emitting diodes	[124]
PAM-PMMA/ DMF	20 kV	280°C (1 h, air), 1000-2800°C (inert)	S_{BET} = 940 $m^2.g^{-1}$	-	[125]
$ZnBr_2$-PAN/ DMF	Omitted	2-methyl imidazole/ methanol dipping, 220°C (3 h, air), 900°C (2 h, Ar)	S_{BET} = 694 $m^2.g^{-1}$	Li-S cathode 636 $mA.h.g^{-1}$ (500 cycles)	[126]
Lignin-PLA/ THF-DMF	7.7 kV 30 $\mu L.min^{-1}$	150°C (14 h, air) 200-250°C (1 h) 900°C (30 min, N_2)	Bio-derived CNFs	Li-ion 611 $mA.h.g^{-1}$ (500 cycles) 186 mA.h	[127]
PEDOT/PSS/PEO/ DMF	8.5 kV, 0.2 $mL.h^{-1}$	Soaking fibres in ethylene glycol to remove PEG	PEDOT:PSS nanofibres on PET substrate	Flexible EDLC, 6 $F.g^{-1}$	[128,129]
B_2O_3/PAN/ PMMA	25 kV, 3.0 $mL.h^{-1}$	Carbonisation 800°C, 1 h	Controllable pore size, porous CNFs	Supercap. Electrodes, 126.31 $F.g^{-1}$	[130]

1.5.1 Energy Storage

As the population of Earth has increased so too have the industrialisation levels and energy demands. These demands have put a great strain on the existing power infrastructure and poses serious implications for the future of a society so dependent on finite energy sources. Until now, energy production methods have largely been fossil fuel combustion and nuclear

fission though, as climate change has garnered increased attention and concern, generating electricity from sustainable sources such as; wind and solar energy, hydroelectricity, and geothermal energy. Generating electricity through sustainable means provides some measure of solution to the problem of green energy however, they are also unpredictable in their generation, i.e. It is not always windy, or a sunny day. As such, renewable sources must be paired with a reliable form of energy storage which can store energy at peak production and release it upon demand.

Several different methods of energy storage exist currently; chemical (e.g. hydrogen[131–133] and liquid nitrogen[134–136]),thermal,[137,138] mechanical energy,[134–136] electrochemical (e.g. batteries[139–143] and fuel cells[144–146]), and electrical (e.g. supercapacitors[147,148,157,158,149–156] and superconducting magnetic energy storage[159–161]). In this section we will evaluate energy storage methods and how carbon-based nanofibres have been applied as useful materials in energy storage applications.

1.5.1.1 Lithium Ion Batteries

Lithium batteries were commercialised in the 1970s and used lithium metal electrodes. Li-Li_xMnO_2 was one of the last systems developed by Tadiran Inc. in Israel for use in mobile phones, however these batteries did not achieve widespread use due to safety problems.[162] Further research into lithium as a power source revealed that lithium could intercalate with transition metal oxides and sulphides could be used as reversible cathode materials for rechargeable Li batteries.[142,163,164] Li-ion batteries are best suited for uses requiring lower power density (0.53 $g.cm^{-3}$)[165] but high cycling durability. The memory effect commonly found in Nickel-Cadmium batteries as well as some Nickel-Metal Hydride batteries is much smaller in Li-ion batteries, that is, Li-ion batteries retain their charge capacity better upon repeated partial charging and discharging.

During the charging process lithium ion are forced to leave the cathode, which is usually lithium-containing metal oxides, by an external electric field and intercalate into a graphite lattice.[165] Apart from protons, no other cations other than the small Li^+ can penetrate into solids by insertion reactions.[140] However the current commercial graphite anode cannot meet increasing performance demands from portable electronic devices with an intrinsic specific capacity of 372 $mA.h.g^{-1}$. Coupled with safety concerns arising from lithium plating and formation of lithium dendrites, an alternative anode material is required.[141,143]

An anode material that was developed by Cho, et al. made use of iron (III) oxide (Fe_2O_3) composite nanofibres which were composed of nanosized hollow iron oxide spheres dispersed in an amorphous carbon matrix. Nanostructured Fe_2O_3 materials are theorised to be able to achieve a capacity of 1005 $mA.h.g^{-1}$, though have previously suffered from capacity fading during cycling. A report of 812 $mA.h.g^{-1}$ was made using bubble-nanorod structured Fe_2O_3-carbon nanofibres after 300 cycles at a current density of 1 $A.g^{-1}$.[166]

By utilising already carbon-containing metal complexes Ren, et al. were able to synthesise carbon nanofibres with encapsulated $CoFe_2O_4$ as an anode material. Ferrocene and Cobaltocene were manually mixed before heating under vacuum at 700°C producing curly nanofibres connecting packed $CoFe_2O_4$ nanocrystallite. Materials provided capacitances up to 705 $mA.h.g^{-1}$ at 100 $mA.g^{-1}$ for 250 cycles, with capacitances increasing with further cycling owing to oxide rearrangement, re-exposing Li_2O formed during early cycles.[167] While a good capacitive response was produced, use of Ferrocene and Cobaltocene early in the synthetic process calls into question environmental concerns, since both molecules require fairly severe syntheses using Grignard reagents as well as the inclusion of Cobalt which has known environmental issues upon disposal.[168,169]

Taking environmental concerns into consideration for material sourcing, Culebras, et al. have developed a Li-ion anode material made from carbon nanofibres developed from

lignin. PLA was mixed into the lignin/dimethylformamide (DMF)/tetrahydrofuran (THF) solutions prior to electrospinning, and the resultant fibres were stabilised at temperatures between 150-250°C for a total of 16 hours before being carbonised at 900°C for 1 hour. Capacitances of up to 611 $mA.h.g^{-1}$ were achieved after 500 cycles between 0.011-3.0 V at a rate of 186 $mA.g^{-1}$.[127]

1.5.1.2 Supercapacitors

As noted by Horn. et al., "Supercapacitors are fundamentally different from traditional (dielectric) capacitors. They are not simply `really good capacitors` as they are sometimes mistaken for".[170] In conventional capacitors two conducting materials are separated by a dielectric, an applied electric potential across the conductors causes electrons to flow and charge accumulates on each conducting plate. The charge remains until the plates are brought into contact again. The storage capability of a capacitor is related to the amount of charge that can be stored at an applied potential and is measured in Farads.

Supercapacitors consist of two electrodes with high surface areas kept separate by an ion-permeable membrane which is used as an insulator to protect the electrodes from short-circuiting.[171,172] The connection between the active electrode material and the surface it is attached to should be ideally without the addition of any other conductive or binding agents to reduce the mass of electrochemically inactive components.[173] An electrolyte, which can be either aqueous or organic, serves as the conductive connection between electrodes across the insulator and is able to enter the pores of the electrodes. Cells must be sealed to ensure stable behaviour over their lifetime.[171,172]

1.5.1.2.1 Electric Double-Layer Capacitors

Before awareness of the pseudocapacitive energy storage mechanism, it was thought that all supercapacitors were electric double-layer capacitors (EDLCs). Double-layer capacitance

is the storage of electrical energy electrostatically, achieved by charge separation in a Helmholtz double-layer[174] at the interface between the surface of a conductor electrode and an electrolyte solution. The separation of charge in a double-layer is a few Angstroms (0.3 – 0.38 nm) and is a surface process as such, the surface characteristics and porosity of the electrode material greatly influence the capacitance of the cell.[175–177]

A study by Phan, et al. highlighted the importance of mesopores and mesopore structure for electrochemical performance, using ordered mesoporous carbon synthesised using nanocasting.[117,178,179] By synthesising the material inside the channels of mesostructured silicates, high specific surface areas could be achieved for these materials. After carbonisation at 900°C, capacitances up to 78 $F.g^{-1}$ were measured and attributed not just to the increased surface area, but the long straight channels leading to lower internal resistance and a larger number of ion-diffusion pathways.[117]

Activated carbons with large surface areas provides good platform materials for double-layer formation since they allow the capture and release of the electrolyte with relatively decreased resistance, though this is dependent on the pore and solvated ion size of the electrolyte.[180–182] However activated carbon manufactured under different conditions may have different porosity and surface conditions, so not all of the BET surface area is electrochemically accessible.[176] EDLCs have demonstrated good cycling stability as well as rate capability however, they generally demonstrate low specific capacitance and energy density.[183,184]

An activated carbon monolith was synthesised by Dobashi, et al. by introducing bacterial cellulose (BC) gel to a polyacrylonitrile (PAN) monolith.[116] The composite formed contained an entangled structure where BC nanofibres entwined around the PAN backbone with no chemical bonds formed between the two materials allowing the composite to retain characteristics of both components. With pre-treatment in air at 200-230°C before

carbonisation at 1000°C in a CO_2/Ar mix the composite structure was retained. With surface areas of 1200-1360 $m^2.g^{-1}$ and excellent rectangular capacitor characteristics, the authors suggest superior EDLC function of BC-PAN activated carbon compared to activated carbon derived from only PAN or commercial activated carbon, though no capacitance value is specifically stated.[116]

EDLC electrode materials have been fabricated using flexible conducting polymers for wearable and portable applications.[185] Cárdenas-Martínez, et.al. managed to deposit fibres formed of poly(3,4-ethylenedioxythiophene) (PEDOT) and polystyrene sulfonate (PSS) onto flexible polyethylene terephthalate (PET) substrates using electrospinning for use as electrodes in flexible and all-solid state supercapacitors.[128] By using an insulating polymer, PEG, as a carrier polymer, conducting PEDOT:PSS mixtures were able to be electrospun into nanofibres with observed measurable conductivities, though only after PEO removal by ethylene glycol soaking.[128,129] Nanofibres and thin films of PEDOT:PSS were produced and tested for their capacitance, with increased capacitance in nanofibres being attributed to a higher accessible active surface area in the one-dimensional structures. Areal capacitances were recorded for nanofibres at 3 $mF.cm^{-2}$ and gravimetric at 6 $F.g^{-1}$ measured at a scan rate of 10 $mV.s^{-1}$ and retaining 92% of the initial capacitance after 1000 charge-discharge cycles.

1.5.1.2.2 Pseudocapacitance

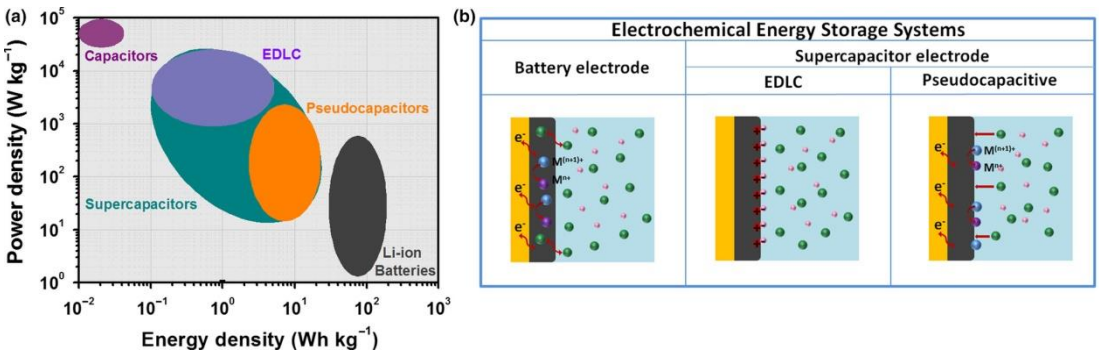

Figure 1.5 a) Ragone plot of different energy storage devices, b) Schematic diagram comparing the fundamental charge storage mechanismsof electrode materials in batteries

and supercapacitors. Reproduced with permission from Jiang. Y, et. al. Copyright 2019 Wiley.[186]

Pseudocapacitance is named to differentiate it from electrostatic capacitance as it arises from reversible Faradaic reactions occurring at the electrode which are depicted in contrast to battery electrodes and EDLC mechanisms in **Figure 1.5**. The capacitive phenomenon occurs through two potential mechanisms; redox reactions, and the deposition of ions to form a monolayer, which cause a charge transfer that is voltage dependent. Functional groups on the surface of a porous electrode material could be oxidised or reduced with the electrode potential. In the case of carbon electrodes, the pseudocapacitance associated with redox reactions of surface functional groups is coupled with the non-Faradaic electric double-layer capacitance.[176]

$$C_{\emptyset} = \frac{q_1 F}{RT} \frac{Kc \pm e^{\left(\frac{-VF}{RT}\right)}}{(1 + Kc \pm e^{\left(\frac{-VF}{RT}\right)})^2} \quad \textbf{(1)}$$

Redox reactions at electrodes occur due to the presence of metal oxides or other heteroatoms and can be observed in the charge/discharge curves which show both double-layer capacitance and overlapping redox reactions.[187] Deposition of ions upon the electrode surface result in a Faradaic charge transfer also, and if the sites are randomly occupied in a fixed lattice, the Langmuir adsorption equation may be used to derive another equation (equation (1), above) describing a pseudocapacitive relationship.[188]

A study by Javed, et al. presented hierarchical mesoporous $NiFe_2O_4$ nanocones as high performance, flexible supercapacitors.[118] Using a hydrothermal method, a $NiFe_2O_4$ nanocone forest was grown upon carbon textile before drying and calcining at 350°C for 2 hours. Capacitances up to 697 $F.g^{-1}$ were presented at a scan rate of 5 $mV.s^{-1}$ within a potential window -0.2 – 0.7 V, and 584 $F.g^{-1}$ for the same scan rate between -0.8 – 0.8 V. With increased scan rate, there was a predictable decrease in measured capacitance which was attributed to less diffusion of electrolyte ions to the interior surfaces at high scan rates.[118,189]

Jeong, et al. synthesised porous CNFs with controllable pore sizes using boron trioxide by dispersing 10 wt.% B_2O_3 in a PAN/PMMA blend in DMF.[130] The solutions were electrospun onto aluminium foil-wrapped rotating drum for aligned fibres before carbonisation. The fibres yielded surface areas of 1065 $m^2.g^{-1}$ and capacitances of 126.31 $F.g^{-1}$ with good capacitance retention, 84% after 3000 cycles. The relative abundance in the initial spinning solution of B_2O_3 was credited with the formation of round-shaped and small-sized pores the authors ascribed to PMMA phase decomposing during thermal decomposition.[130]

Carbon nanodot-decorated graphene/polyaniline composites were produced through in-situ self-assembly of aniline in a dispersion of graphene oxide nanosheeets and β-cyclodextrin in deionised water before in-situ polymerisation to achieve a dark green gel precursor.[119] Graphene oxide was reduced by one-pot hydrothermal reduction at 180°C for 3 h before being washed and dried. Cyclic voltammetry measurements were conducted between -0.7 – 0.3 V and achieved capacitances up to 871 $F.g^{-1}$ at a current density of 2 $A.g^{-1}$, with 73% capacity retention after 10 000 cycles. The supramolecular in-situ self-assembly method was suggested by the authors as a preparation method for graphene-based composite electrode materials for supercapacitors since cyclodextrin can form inclusion complexes with many other small molecules.[119]

1.5.2 Sensing

A sensor is a device which monitors changes in its environment and can transmit information of its findings in an analytically useful signal. Chemical sensors specifically have found many applications in environmental monitoring, food processing, medical devices, and toxic material detection. Previously, methods of characterisation required time-consuming and expensive instrumentation only operable by trained personnel.[190] Ideally chemical sensors exist to bypass the arduous processes and provide a cheap and user-friendly alternative.[190,191]

1.5.2.1 pH Sensing

pH is central in a wide range of fields including chemistry, agriculture, food processing, pharmaceuticals, environmental science, and chemical and biomedical engineering appliations.[19,192–200] For medical applications regular monitoring of pH, for example, at wound sites can quickly and efficiently highlight the presence of bacterial colonies and enzymes. Similarly in food processing, pH values contain information about growth of microorganisms and bacteria, and the denaturisation of proteins.[192,201–204] In addition, water pollution can be monitored effectively using its pH value.[192,205–207]

Glass pH electrodes are the most widely used pH sensors that allow for pH sensing between alkaline and acid conditions. Low detection limits, long term stability, and high reproducibility provides excellent performance, though there are some mechanical fragility issues as well as temperature dependent responses which limits their application in cellular pH sensing.[208] An alternative and complementary technique is optical pH sensing which is based upon absorption or fluorescence changes at different pH values. Fluorescent-based sensors usually provide higher sensitivity at lower concentrations of indicator and have been successfully employed for real-time pH sensing applications.[209–211]

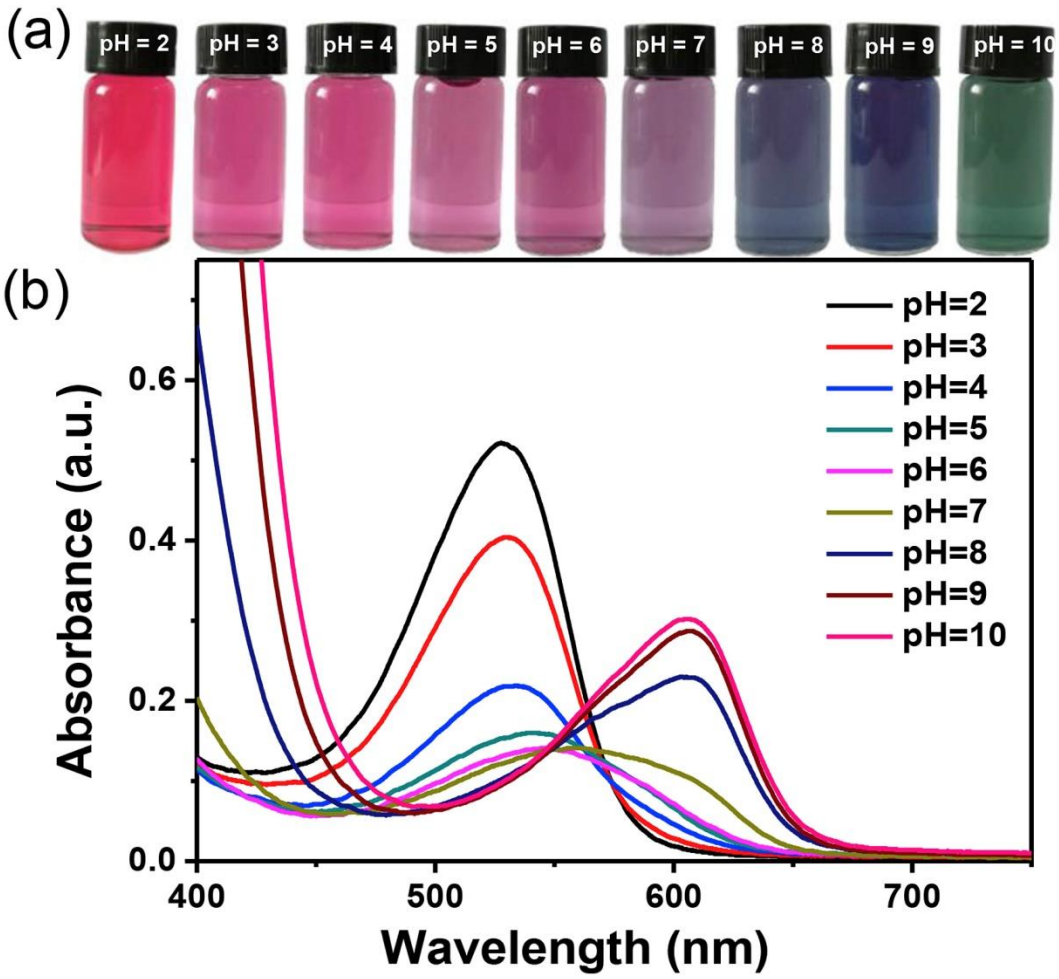

Figure 1.6 Anthocyanin aqueous solutions with different pH values (2–10): (a) optical image and (b) UV–vis absorption spectra. Reproduced with permission from Tang. B, et. al.[120]. Copyright 2019 Elsevier.

Natural dyes have attracted considerable attention due to their abundancy, sustainability, and non-toxicity. Tang, et al. demonstrated pH sensitive anthocyanin solutions extracted from purple sweet potato and measured using UV-Vis absorption. The pH was adjusted using HCl and NaOH between pH 2 and pH 10 with a red-shift associated with the acidic pH while alkaline pH resulted in a blue/green shift as can be seen in **Figure 1.6**.[120] The red colour at acidic pH was due to preference for the flavylium cation while the blue colour was formed by quinonoidal base.[120]

Pfeifer, et al. presented a perylene bisimide derived molecule (PBI) as intrinsically pH-sensitive with a bathochromic shift in the absorption and emission spectra upon deprotonation.[7] The PBI was N,N'-substituted with two isopropylphenyl groups and two

2-phenylimidazole substitutions on the perylene core. Imide substituents accounted for PBI's very high solubility, while the addition of 2-phenylimidazole substituents at bay positions was the cause of the strong bathochromic shift.[7]

1.5.2.2 Organic molecule sensing

Current methods to detect the presence and identity of small molecules include chromatography (gas-, liquid-, and high-performance liquid-), electrochemical methods, enzymatic biosensors, fluorimetry, and colourimetry. As mentioned previously, it is desirable to avoid time-consuming and expensive methods. Another method revolves around nanopore-based sensing which is used to detect single molecules and identify target molecules through current modulations.

Zhang, et al. recently demonstrated a functionalised, conical PET nanopore sensor which was sensitive and selective for specific proteins. 12 μm thick PET foils were irradiated with heavy ions (Au) before etching at room temperature by an asymmetric etching method where the foil was mounted between two isolated containers of an etchant solution, NaOH in a methanol/water mix, and a stopping solution of formic acid/KCl aqueous mix.[212] Functionalisation of the nanopores was achieved by attaching ethylenediamine to the carboxyl group on the conical nanopore's surface.[213] The authors used asymmetric pores to enhance desorption through creation of a bipolar pore with a higher field which increased throughput and residence time which in turn improved resolution in the label free detection and characterisation of proteins.[121]

Nitroreductases (NTRs), hypoxic enzymes, are a key hallmark of aggressive disease in various hypoxic tumour cells. Thus, their detection is of great importance for theranostic and drug development purposes.[214] Zhang, et al. presented a turn-on fluorescent probe synthesised from 2,3,3-trimethyl-3H-indole, *p*-nitrobenzyl bromide, and a benzenaminium chloride.[122,215] UV absorption and fluorescence emission were used to measure NTR-

triggered activation of the probe under physiological conditions (pH 7.4, 37°C) and a lower detection limit was established at 36.9 ng.mL^{-1}.[122]

1.5.2.3 Metal Ion Sensing

Heavy metals, mostly consisting of those with molecular weights between 63.5 and 200.5 g.mol^{-1}, are non-biodegradable and present a significant risk to environmental well-being due to their ubiquitous presence. Some heavy metals are required by living organisms in small quantities however, high amounts tend to accumulate and can cause various diseases and disorders. Fertilisers used in intensive farming are enriched with nitrogen, potassium, and phosphorus, though they often also contain trace amounts of cadmium and lead, both of which are known to cause kidney damage.[216,217] Similarly pesticides containing significant concentrations of metals in the past has led to a rise in concentration to much greater levels than background concentrations.[218,219]

Metal-organic frameworks (MOFs) have a wide variety of potential applications given their flexible synthetic nature of combined metals and organic linkers. A bimetallic MOF was presented by Sreevidya, et al. and investigated for its sensing capabilities of toxic metal ions like lead and chromium. Zirconium oxychloride, copper sulphate pentahydrate, and terephthalic acid (1,4-BDC) were mixed and subjected to a hydrothermal synthesis to achieve the MOF $[Zr/Cu(1,4\text{-}BDC)(H_2O)]_n$. In the presence of Pb^{2+}, the MOF acted as a turn-on fluorescent sensor, but in the presence of Cr^{6+} the MOF acted as a turn-off sensor while maintaining a robust structure.[123]

Meanwhile, Molybdenum disulphide quantum dots were presented as a fluorescent turn-off sensor, also for Pb^{2+} in aqueous medium. Sharma, et al. used a facile hydrothermal synthesis with sodium molybdenate, thioacetamide, and 1,4-diaminobutane as a capping agent before purification through dialysis.[123] The formed quantum dots could detect

concentrations of Pb^{2+}, from lead perchlorate, in a wide dynamic range of 33 µM to 8.0 mM though with a lower limit of detection of 50 µM.

1.6 Processing and Analysis Techniques

1.6.1 Fluorescence Spectroscopy

Fluorescence is the emission of light by a substance after excitation by light or other electromagnetic radiation.[220–222] The emitted light is usually of a longer wavelength than the absorbed radiation and as such, is of a lower energy due to non-radiative relaxation of electrons. Fluorescent materials can often be observed in the visible region after absorbing light in the ultraviolet region. Fluorescence ceases almost immediately after the radiation source stops, unlike phosphorescence which continues to emit light for some time after.

$$S_0 + h\upsilon \rightarrow S_1 \quad \textbf{(2)}$$

$$S_1 \rightarrow S_0 + h\upsilon_{em} + heat \quad \textbf{(3)}$$

Fluorescence occurs when an electron from a molecule, atom, or nanostructure relaxes from its excited singlet state by emitting a photon. Where S_0 is the ground state, S_1 is the excited state, h is Planck's constant, 6.626×10^{-34} $m^2.kg.s^{-1}$, υ is the frequency of light emitted. As mentioned above in equation 2 the relationship between frequency and wavelength may be exploited to calculate the energy of the transition.

It is possible for relaxation from the S_1 state through interaction with a second molecule, for example molecular oxygen, due to its unusual triplet ground state. Other distortions arrive from the sample including: photodecomposition which may decrease the intensity of fluorescence over time, as well as light scattering. Rayleigh light scattering has the same wavelength as the incident radiation and is usually elastic scattering of light by particles much smaller than the wavelength of the radiation. Whereas Raman light scattering results

in a change in the wavelength of light, usually to longer wavelengths, due to excitation to a virtual electronic state. The molecules may relax to a vibrational level other than the ground vibrational state.

At low concentrations fluorescence intensity is generally proportional to the concentration of the excited fluorophore. At greater concentrations the fluorescence generally no longer follows this rule because: the fluorophore solubility is exceeded and insoluble fluorophore aggregates and/or precipitates, the fluorophore absorbs the exciting and possible emitted light, known as the inner filter effect, reducing the amount of light detected, or the fluorophore self-quenches by forming complexes.

1.6.2 Ultraviolet – Visible Spectrophotometry, UV-Vis

UV-Visible spectroscopy relies on electronic energy level transitions due to light absorption.[220,223,224] Molecules containing bonding and non-bonding electrons (*n*-electrons) can absorb energy in the form of light, within the ultraviolet to visible range, to excite electrons to higher anti-bonding molecular orbitals. Lower energy gaps, i.e. the energy gap between the HOMO and the LUMO, may be overcome by absorbing light of longer wavelengths. There are four possible transitions, σ-σ^* > n-σ^* > π-π^* > n-π^*. Peaks at specific wavelengths may be translated to the difference in energy levels using equation **(4)**.

$$\Delta E = h\upsilon = \frac{h.c}{\lambda} \quad \textbf{(4)}$$

Where ΔE is the energy change associated with an electronic transition from a ground state to an excited state (J), h is Planck's constant 6.626 x 10^{-34} $m^2.kg.s^{-1}$, υ is the frequency of light which may be similarly defined by the relationship between the speed of light, c, 2.998 $m.s^{-1}$, and the wavelength in question, λ (nm).

$$A = \varepsilon . c . l \quad \textbf{(5)}$$

UV-Vis may also be used in a quantitative analysis of material using the Beer-Lambert law (equation 4) which states that the absorbance, *A*, of a solution is directly proportional to the concentration, *c* (mol.dm^{-3}), of the absorbing species in the solution and the path length, *l* (cm). Concentration changes of the absorber may be monitored by comparing using known molar extinction coefficients, ε (mol^{-1}.dm^{3}.cm^{-1}) or calibration curves.

1.6.3 Raman Spectroscopy

Raman spectroscopy uses infrared light to observe vibrational, rotational, and other low-frequency modes in a system.[225–229] It provides a structural fingerprint by which molecules can be detected, generated by inelastic or Raman scattering of monochromatic light. Monochromatic light; generated by a laser in the visible, near infrared, or near ultraviolet range interacts with molecular vibrations or other excitations in the system resulting in the energy of the laser photons being shifted up or down. The shift in energy gives information about the vibrational modes in the system.

Spontaneous Raman scattering is weak and is difficult to separate weak inelastically scattered light from the much stronger Rayleigh scattered light. Rayleigh scattering is the predominantly elastically scattered light resulting from the electric polarisability of particles, and may be filtered out by a band stop or pass filter while the rest of the collected light is dispersed onto a detector.

Both Rayleigh and Raman are to photon processes which involve scattering of incident light from a virtual sate. The incident photon is momentarily absorbed by a transition from the ground state into a virtual state and new photon is created and scattered by a transition from this virtual state. Rayleigh scattering is the most likely event to occur and the photon which results is from a transition from the virtual state back to the ground state and is of

the same wavelength and therefore, energy as the incident photon. Raman scattering is far less likely than Rayleigh and the scattered photon results from a transition from the virtual state to the first excited state of the molecular vibration. The description, inelastic scattering arises since the molecule acquires different vibrational energy and the scattered photon has different energy and frequency than the incident photon.

There are two different types of Raman scattering: Stokes and anti-Stokes. Molecules initially in the ground state present Stokes Raman scattering, in which the molecules end up in an excited vibrational state. While molecules that are in a vibrational excited state give rise to anti-Stokes Raman scattering, and terminate in the ground state. Boltzmann population distributions at thermal equilibrium describe ratios between Stokes and anti-Stokes scattering. Stokes Raman lines are more intense than anti-Stokes at ambient temperature, since most molecules are found in the ground state.

1.6.4 Fourier Transform Infrared Spectroscopy, FTIR

Infrared spectroscopy involves the interaction of infrared radiation with matter in a way which can be used to identify and study chemicals.[230,231] The generated infrared spectrum is produced with absorbance (A), or transmittance (%T) vs frequency (cm^{-1}), or wavelength (μm). While the infrared portion of the electromagnetic spectrum is usually divided into three regions; the near-, mid-, and far- infrared, the min-infrared, approximately 4000-400 cm^{-1} (2.5-25 μm) is the primary region used for studying fundamental vibrations and associated rotational-vibrational structure. Molecules absorb frequencies that are characteristic of their structure that is to say, absorptions occur at resonant frequencies which match vibrational frequencies.

Samples contain vibrational modes which are ways in which a molecule can vibrate. Linear molecules have 3N – 5 degrees of vibration, whereas non-linear molecules have 3N – 6

degrees of vibrational freedom. In order for a vibrational mode in a molecule to be infrared active there must be an associated change in the dipole moment, which is independent of the presence of a permanent dipole.

Similar to UV-vis spectroscopy, the objective of infrared spectroscopy is to obtain a spectrum of absorption or emission of light at each wavelength. While UV-Vis spectroscopy makes use of a monochromatic filter to perform a dispersive spectroscopy technique, which measures how much of the light is absorbed for each different wavelength. Fourier-transform infrared spectroscopy (FTIR) shines a beam containing many frequencies of light at once and measures how much of that beam was absorbed by the sample. The beam is then modified to contain a different combination of frequencies, giving a second data point. This process is repeated rapidly over a short time span and then a computer takes all the data and works backwards to infer what the absorption is at each wavelength. Computation processing requires usage of the Fourier transform which converts one domain into its inverse domain.

Attenuated total reflection (ATR) is a technique which is used to directly examine samples in the solid or liquid state without requiring further preparation. ATR uses a beam of infrared light passed through an ATR crystal such that it reflects at least ones off the internal surface in contact with the sample. An oscillating electric and/or magnetic field which does not propagate as an electromagnetic wave but whose energy is spatially concentrated in the vicinity of the source is known as an evanescent wave. An evanescent wave only forms if the ATR crystal is made of an optical material with a higher refractive index than the sample being studied, otherwise light will be lost to the sample. An advantage of ATR-IR over transmission-IR is the limited path length into the sample, which avoids the problem of strong attenuation of the IR signal in highly absorbing media such as aqueous solutions.

1.6.5 Nuclear Magnetic Resonance Spectroscopy, NMR

Nuclear Magnetic Resonance spectroscopy is a widespread technique which uses superconducting magnets to produce a large magnetic field capable of aligning the spins of atomic nuclei and measuring their relaxation. Isotopes which contain odd numbers of protons and/or neutrons have an intrinsic non-zero nuclear spin, the most commonly used nuclei are ^{1}H, and ^{13}C.[232,233]

NMR spectroscopy is used to observe local magnetic fields around atomic nuclei. When placed in a magnetic field, NMR active nuclei absorb electromagnetic radiation at a frequency characteristic of the isotope. The resonant frequency, that is the energy of the radiation absorbed, and the intensity of the signal are proportional to the strength of the magnetic field. Since the majority of molecules in a solution are the solvent molecules and most regular solvents are hydrocarbons or, in the case of ^{1}H NMR, otherwise containing NMR-active protons, to avoid detecting only signals from solvent hydrogens, deuterated solvents are used.

NMR samples typically spin in a sample-holder inside a strong magnet, this is necessary to average out diffusional motion. In order to compensate for inhomogeneity and drift in the magnetic field, the spectrometer maintains a lock on the solvent frequency with a separate lock unit, and high resolution NMR spectrometers use shim coils and currents to adjust the homogeneity of the magnetic field to parts per billion in a volume of cubic centimeters. The idea is to adjust the shim currents so as to cancel any gradients in the NMR sample as accurately as possible.[234]

The sample is then excited using a radio frequency pulse (60-100 MHz) and a nuclear magnetic resonance response is received. The response is a very weak signal in the form of a free induction decay, FID, requiring sensitive receivers to pick up. A Fourier Transform

must be carried out to extract the frequency-domain spectrum from the raw time-domain FID. The signal-to-noise ratio may be improved with repeat acquisitions and averaging.

1.6.6 Elemental Analysis, CHNX

Elemental analysis is used to identify the elemental, and sometimes isotopic composition of samples.[235] For chemists, elemental analysis refers to CHNX analysis which is the determination of mass fractions of carbon, hydrogen, nitrogen, and heteroatoms (X, usually halogens or sulfur). While other spectroscopic techniques; NMR, mass spectrometry, and chromatography have replaced elemental analysis as the primary technique for structural determination, it still provides useful, complementary information, and remains the fastest and most inexpensive method to determine sample purity.

CHNX is most commonly accomplished through combustion analysis, in which the samples are burned in an excess of oxygen and various traps collect the combustion products: carbon dioxide, water, and nitric oxide. Masses of these combustion products can be used to calculate composition of the unknown sample.

1.6.7 Thermogravimmetric Analysis, TGA

Thermogravimetric analysis (TGA) is a method of thermal analysis in which the mass of a sample is measured over time as the temperature is changed.[236,237] While the technique can be used to measure physical phenomena such as phase transitions, absorption, adsorption, and desorption, it can also be employed to observe chemical phenomena including chemisorptions, thermal decomposition and solid-gas reactions (e.g. oxidation or reduction).

Features of thermogravimetric curves which can be identified include: a horizontal portion, where $\frac{dw}{dt} = 0$, indicates constant weight; A curved portion, in which the steepness of the

curve indicates the rate of weight loss; or an inflection at which point $\frac{dw}{dt}$ may be at a minimum but have a non-zero value. This can imply the formation of an intermediate in the decomposition process, however it can also be indicative of an unstable heating rate or thermocouple response.

The heating rate of the furnace affects the steepness of the curved portions, and can also give inaccuracies in T_1, the initial temperature of decomposition and T_f the final temperature of decomposition. Given that with faster heating, f, it has been shown that $(T_f)_f > (T_f)_s$, where s denotes slower heating rates. As such, it is important to have an independent temperature-time record as well as ensuring that the heating rate is not so great to obscure decomposition regions.

1.6.8 N_2 Sorption

Brunauer-Emmett-Teller (BET) theory aims to explain the physical adsorption of gas molecules on a solid surface and provides the basis for the analytical technique used for the measurement of specific surface area of materials.[238,239] Unlike Langmuir theory, which describes monolayer molecular adsorption, BET theory extends to multilayer adsorption using the following assumptions: gas molecules physically adsorb to a solid in infinite layers; gas molecules only interact with adjacent layers; and the Langmuir theory can be applied to each layer.

The Langmuir adsorption model assumes: the adsorbate behaves as an ideal gas at isothermal conditions; the surface containing adsorbing sites is homogeneous; the adsorbate adsorbs into an immobile state; all sites are equivalent; each site can hold one molecule of the adsorbate; and there are no interactions between adsorbate molecules on adjacent sites.

$$\frac{1}{V[\left(^{p^*}/_{p}\right)-1]} = \frac{(c-1).(^{p^*}/_{p})}{c.V_{mono}} + \frac{1}{c.V_{mono}} \quad \textbf{(6)}$$

In which, V is the volume of gas adsorbed (cm^{-3}), p is absolute pressure ($N.m^{-2}$), $p*$ is absolute pressure ($N.m^{-2}$), V_{mono} is the volume of gas adsorbed (cm^{-3}) as a monolayer to the surface of the material, and c is the BET constant.

The resulting BET equation (Eq (6)) was then used to calculate specific surface area using a plot of relative pressure, $\frac{1}{\mathrm{V}[(^{p^*}/_{p})-1]}$, against, $\frac{p}{p^*}$, the linear range from which was identified and used to calculate the volume of gas required to form a monolayer, V_{mono}, on the surface using the slope, $\frac{(c-1)}{c.V_{mono}}$, and y-intercept, $\frac{1}{\mathrm{c}.V_{mono}}$. Using the volume of a monolayer of adsorbant, the area occupied by gas molecules was calculated by assuming the gas behaves ideally. Thus, using the ideal gas equation **(7)** and equation **(8)**, the surface area of the material was calculated.

$$p.V_{mono} = n.R.T \quad \textbf{(7)}$$

Since the gas used is assumed to be obeying ideal conditions, it is possible to use the ideal gas law (equation 7) to calculate the number of moles of N_2 adsorbed onto the surface. Where n is the number of moles, R is the ideal gas constant, 8.314 $J.mol^{-1}.K^{-1}$, and T is temperature in Kelvin.

$$S_A = (n.N_A.A) \quad \textbf{(8)}$$

Using the result calculated using equation 7, the surface area, S_A (m^2) may be calculated using Avogadro's number, N_A, 6.022×10^{23} mol^{-1}, the cross-sectional area of a single molecule of N_2, A, 1.62×10^{-19} m^2 in equation 8. This surface area may be divided by the mass of the sample used to provide the specific surface area for the material.

1.6.9 Field Emission Scanning Electron Microscopy, FESEM

Scanning electron microscopy (SEM) produces images of a sample by scanning the surface with a focused beam of electrons.[240,241] Electrons interact with atoms in the sample producing various signals including: secondary electrons, back-scattered electrons, and characteristic X-rays. Secondary electrons are generated as ionisation products, by the primary radiation, in this case the incident electron beam. Plotting the inelastic mean free path as a function of energy shows

Secondary electron detectors are standard for secondary electron imaging (SEI) which produces high-resolution, details less than 1nm in size, images of sample surfaces since they are emitted from very close to the sample surface. The sensitivity of electrons to the sample surface is best illustrated using a plot of the inelastic mean free path against electron kinetic energy.

Conversely, back-scattered electrons are beam electrons reflected from further within the body of the sample by elastic scattering. While the resolution provided by back-scattered electrons is less than that of SEI, back-scattered electrons are often used in analytical SEM, alongside the spectra from characteristic X-rays, since the intensity of their signal is strongly related to the atomic number of the sample. As such, images born of back-scattered electrons can provide information about the distribution, but not identity, of different elements within a sample. Characteristic X-rays are emitted when the electron beam removes an inner shell electron from an atom within the sample, causing a higher energy electron to fill the shell and release the corresponding amount of energy as X-rays. Measuring the energy or wavelength of these characteristic X-rays can be achieved using Energy-dispersive X-ray spectroscopy (EDX) or Wavelength-dispersive X-ray spectroscopy (WDXS).

1.7 Aims and Objectives

Within this thesis a PDI molecule is presented and characterised for its self-assembly features through monolithic formation by pH-triggering or solvent-exchange mechanisms, and also through electrospinning. Initial work was performed to formulate and optimise solutions which were capable of providing fibres through self-assembly or electrospinning in mild aqueous and ambient conditions to reduce environmental impact. In addition a rapid-response solution-based sensor capable of detection and identification of metal ions in aqueous solutions is presented. Furthermore, a facile route towards a high capacitance electrode is presented with a view towards supercapacitor applications which could provide rapid charging with minimal compromise to capacity.

1.8 References

1 Y. Sun, T. Zuo, F. Guo, J. Sun, Z. Liu and G. Diao, *RSC Advances*, 2017, **7**, 24215–24220.

2 S. K. Yang, X. Shi, S. Park, S. Doganay, T. Ha and S. C. Zimmerman, *Journal of the American Chemical Society*, 2011, **133**, 9964–9967.

3 H.-X. Wang, Y.-H. Lang, H.-X. Wang, J.-J. Lou, H.-M. Guo and X.-Y. Li, *Tetrahedron*, 2014, **70**, 1997–2002.

4 Q. Al-Galiby, I. Grace, H. Sadeghi and C. J. Lambert, *Journal of Materials Chemistry C*, 2015, **3**, 2101–2106.

5 H. Szelke, S. Schübel, J. Harenberg and R. Krämer, *Chemical Communications*, 2010, **46**, 1667.

6 X. Feng, Y. An, Z. Yao, C. Li and G. Shi, *ACS Applied Materials & Interfaces*, 2012, **4**,

614–618.

7 D. Pfeifer, I. Klimant and S. M. Borisov, *Chemistry - A European Journal*, 2018, **24**, 10711–10720.

8 B. Wang and C. Yu, *Angewandte Chemie International Edition*, 2010, **49**, 1485–1488.

9 Y. Che, X. Yang and L. Zang, *Chemical Communications*, 2008, **0**, 1413.

10 P. S. Hariharan, J. Pitchaimani, V. Madhu and S. P. Anthony, *Journal of Fluorescence*, 2016, **26**, 395–401.

11 Y. Liao, J. Weber and C. F. J. Faul, *Macromolecules*, 2015, **48**, 2064–2073.

12 Q. Zhao, S. Zhang, Y. Liu, J. Mei, S. Chen, P. Lu, A. Qin, Y. Ma, J. Z. Sun and B. Z. Tang, *Journal of Materials Chemistry*, 2012, **22**, 7387–7394.

13 D. Sriramulu and S. Valiyaveettil, *Dyes and Pigments*, 2016, **134**, 306–314.

14 N. I. Georgiev, A. R. Sakr and V. B. Bojinov, *Dyes and Pigments*, 2011, **91**, 332–339.

15 R. Zhang, Z. Wang, Y. Wu, H. Fu and J. Yao, *Organic Letters*, 2008, **10**, 3065–3068.

16 S. Sowmiyha, V. V. Kumar, J. Pitchaimani, V. Madhu, R. Thiagarajan, N. S. Subramanian and S. P. Anthony, *Journal of Luminescence*, 2018, **203**, 42–49.

17 F. Criscitiello, A. Scigliano, R. Bianco, M. R. Beccia, T. Biver and A. Pucci, *Colloids and Surfaces A: Physicochemical and Engineering Aspects*, 2017, **516**, 32–38.

18 J. Y. Kim, S. W. Woo, J. W. Namgoong and J. P. Kim, *Dyes and Pigments*, 2018, **148**, 196–205.

19 X. Zhang, S. Rehm, M. M. Safont-Sempere and F. Würthner, *Nature Chemistry*, 2009, **1**, 623–629.

20 K. Sun, C. Xiao, C. Liu, W. Fu, Z. Wang and Z. Li, *Langmuir*, 2014, **30**, 11040–11045.

21 J. M. Seco, E. San Sebastián, J. Cepeda, B. Biel, A. Salinas-Castillo, B. Fernández, D. P. Morales, M. Bobinger, S. Gómez-Ruiz, F. C. Loghin, A. Rivadeneyra and A. Rodríguez-Diéguez, *Scientific Reports*, 2018, **8**, 14414.

22 N. N. Lathiotakis, I. S. K. Kerkines, G. Theodorakopoulos and I. D. Petsalakis, *Chemical Physics Letters*, 2018, **691**, 388–393.

23 F. C. De Schryver, T. Vosch, M. Cotlet, M. Van der Auweraer, K. Müllen and J. Hofkens, *Accounts of Chemical Research*, 2005, **38**, 514–522.

24 E. R. Draper, J. J. Walsh, T. O. McDonald, M. A. Zwijnenburg, P. J. Cameron, A. J. Cowan and D. J. Adams, *Journal of Materials Chemistry C*, 2014, **2**, 5570–5575.

25 C. Huang, S. Barlow and S. R. Marder, *The Journal of Organic Chemistry*, 2011, **76**, 2386–2407.

26 B. Pagoaga, O. Mongin, M. Caselli, D. Vanossi, F. Momicchioli, M. Blanchard-Desce, G. Lemercier, N. Hoffmann and G. Ponterini, *Physical Chemistry Chemical Physics*, 2016, **18**, 4924–4941.

27 R. M. Pinto, E. M. S. Maçôas, A. I. S. Neves, S. Raja, C. Baleizão, I. C. Santos and H. Alves, *Journal of the American Chemical Society*, 2015, **137**, 7104–7110.

28 M. Greene, in *High Performance Pigments*, Wiley-VCH Verlag GmbH & Co. KGaA, Weinheim, Germany, 2009, pp. 261–274.

29 K. Hunger and W. Herbst, in *Ullmann's Encyclopedia of Industrial Chemistry*, Wiley-VCH Verlag GmbH & Co. KGaA, Weinheim, Germany, 2000, pp. 379–423.

30 W. Herbst, K. Hunger, G. Wilker, H. Ohleier and R. Winter, *Industrial Organic*

Pigments, Wiley, 3rd Ed., 2004.

31 S. Chen, P. Slattum, C. Wang and L. Zang, *Chemical Reviews*, 2015, **115**, 11967–11998.

32 F. Würthner, *Chemical Communications*, 2004, **14**, 1564–1579.

33 J. D. Ferry, *Viscoelastic properties of polymers*, Wiley, 1980.

34 U. Wais, A. W. Jackson, T. He and H. Zhang, *Nanoscale*, 2016, **8**, 1746–1769.

35 L. Zang, Y. Che and J. S. Moore, *Accounts of Chemical Research*, 2008, **41**, 1596–1608.

36 G. Boobalan, P. K. M. M. Imran, C. Manoharan and S. Nagarajan, *J. Colloid Interface Sci.*, 2013, **393**, 377–383.

37 N. Wu, C. Wang, B. R. Bunes, Y. Zhang, P. M. Slattum, X. Yang and L. Zang, *ACS Applied Materials and Interfaces*, 2016, **8**, 12360–12368.

38 L. Liu, J. Sjöblom and Z. Xu, *Energy and Fuels*, 2016, **30**, 3742–3751.

39 C. Wang, B. R. Bunes, M. Xu, N. Wu, X. Yang, D. E. Gross and L. Zang, *ACS Sensors*, 2016, **1**, 552–559.

40 Y. Zheng, A. J. Giordano, R. C. Shallcross, S. R. Fleming, S. Barlow, N. R. Armstrong, S. R. Marder and S. S. Saavedra, *Journal of Physical Chemistry C*, 2016, **120**, 20040–20048.

41 G. Dong, L. Yang, F. Wang, L. Zang and C. Wang, *ACS Catalysis*, 2016, **6**, 6511–6519.

42 F. Reincke, S. G. Hickey, W. K. Kegel and D. Vanmaekelbergh, *Angewandte Chemie International Edition*, 2004, **43**, 458–462.

43 A. D. Dinsmore, M. F. Hsu, M. G. Nikolaides, M. Marquez, A. R. Bausch and D. A.

Weitz, *Science*, 2002, **298**, 1006–1009.

44 H. Duan, D. Wang, D. G. Kurth and H. Möhwald, *Angewandte Chemie International Edition*, 2004, **43**, 5639–5642.

45 W. H. Binder, *Angewandte Chemie International Edition*, 2005, **44**, 5172–5175.

46 D. Grosso, F. Cagnol, G. J. de A. A. Soler-Illia, E. L. Crepaldi, H. Amenitsch, A. Brunet-Bruneau, A. Bourgeois and C. Sanchez, *Advanced Functional Materials*, 2004, **14**, 309–322.

47 V. Tchakalova, T. Zemb and D. Benczédi, *Colloids and Surfaces A: Physicochemical and Engineering Aspects*, 2014, **460**, 414–421.

48 H. Wu, Z. Zhang, S. Mann and W. H. Briscoe, *Journal of Colloid and Interface Science*, 2019, **558**, 78–84.

49 W. Bai, R. Yao, N. Lai, X. Shang, Y. Xu and J. Lin, *Reactive and Functional Polymers*, 2018, **122**, 33–41.

50 X. Xiao, W. Bai, L. Cai and J. Lin, *Chemistry Letters*, 2014, **43**, 331–333.

51 S. Kundu, U. Mogera, S. J. George and G. U. Kulkarni, *Nano Energy*, 2019, **61**, 259–266.

52 P. Sharma and M. S. Mehata, *Materials Research Bulletin*, 2020, **131**, 110978.

53 F. B. Wiedemann-Bidlack, E. Beniash, Y. Yamakoshi, J. P. Simmer and H. C. Margolis, *Journal of Structural Biology*, 2007, **160**, 57–69.

54 A. Datar, K. Balakrishnan and L. Zang, *Chemical Communications*, 2013, **49**, 6894–6896.

55 J. Wang, W. Shi, D. Liu, Z. Zhang, Y. Zhu and D. Wang, *Applied Catalysis B:*

Environmental, 2017, **202**, 289–297.

56 D. H. Reneker and A. L. Yarin, *Polymer*, 2008, **49**, 2387–2425.

57 G. Taylor, *Proceedings of the Royal Society A: Mathematical, Physical and Engineering Sciences*, 1969, **313**, 453–475.

58 J. Zeleny, *Physical Review*, 1914, **3**, 69–91.

59 N. Bhardwaj and S. C. Kundu, *Biotechnology Advances*, 2010, **28**, 325–347.

60 J. Zou, M. Lu, S. Chen, C. Cai, Z. Yao, W. Cui, C. Fan and S. Liu, *Materials Science and Engineering C*, 2020, **116**, 111166.

61 T. Subbiah, G. S. Bhat, R. W. Tock, S. Parameswaran and S. S. Ramkumar, *Journal of Applied Polymer Science*, 2005, **96**, 557–569.

62 J. . Deitzel, J. Kleinmeyer, D. Harris and N. . Beck Tan, *Polymer*, 2001, **42**, 261–272.

63 X.-H. H. Qin, E.-L. L. Yang, N. Li and S.-Y. Y. Wang, *Journal of Applied Polymer Science*, 2007, **103**, 3865–3870.

64 C. Chang, K. Limkrailassiri and L. Lin, *Applied Physics Letters*, 2008, **93**, 123111.

65 D. Sun, C. Chang, S. Li and L. Lin, *Nano Letters*, 2006, **6**, 839–842.

66 Y.-S. Park, J. Kim, J. M. Oh, S. Park, S. Cho, H. Ko and Y.-K. Cho, *Nano Letters*, 2020, **20**, 441–448.

67 C. Yang, Z. Jia, Z. Xu, K. Wang, Z. Guan and L. Wang, in *2009 Annual Report Conference on Electrical Insulation and Dielectric Phenomena*, Institute of Electrical and Electronics Engineers, 2009, pp. 204–207.

68 S.-X. Wang, C. C. Yap, J. He, C. Chen, S. Y. Wong and X. Li, *Nanotechnology Reviews*,

2016, **5**, 51–73.

69 A. Das, J. Adhikari and P. Saha, in *Nanocarbon and its Composites: Preparation, Properties and Applications*, Elsevier, 2018, pp. 91–122.

70 D. Giuri, M. Barbalinardo, G. Sotgiu, R. Zamboni, M. Nocchetti, A. Donnadio, F. Corticelli, F. Valle, C. G. M. Gennari, F. Selmin, T. Posati and A. Aluigi, *Nanoscale*, 2019, **11**, 6422–6430.

71 S. Torres-Giner, in *Multifunctional and Nanoreinforced Polymers for Food Packaging*, Elsevier, 2011, pp. 108–125.

72 M. A. Cerqueira, S. Torres-Giner and J. M. Lagaron, in *Nanomaterials for Food Packaging: Materials, Processing Technologies, and Safety Issues*, Elsevier, 2018, pp. 147–171.

73 H. Yu, Y. Song, Y. Tang, Y. Li and S. Liu, *Ceramics International*, 2018, **44**, 12149–12156.

74 F. Sultanov, C. Daulbayev, B. Bakbolat, O. Daulbayev, M. Bigaj, Z. Mansurov, K. Kuterbekov and K. Bekmyrza, *Chemical Physics Letters*, 2019, **737**, 136821.

75 Q. Zhou, M. Bao, H. Yuan, S. Zhao, W. Dong and Y. Zhang, *Polymer*, 2013, **54**, 6867–6876.

76 C. Peng, P. Liu, J. Hu, T. Hua, Y. Shen, B. Zhao and G. Tang, *Colloids and Surfaces A: Physicochemical and Engineering Aspects*, 2014, **457**, 1–7.

77 M. Zhi, A. Manivannan, F. Meng and N. Wu, *Journal of Power Sources*, 2012, **208**, 345–353.

78 R. Khajavi and M. Abbasipour, *Scientia Iranica*, 2012, **19**, 2029–2034.

79 B.-S. Lee, H.-S. Yang and W.-R. Yu, *Nanotechnology*, 2014, **25**, 465602.

80 J. Kong, S. Y. Wong, Y. Zhang, H. R. Tan, X. Li and X. Lu, *Journal of Materials Chemistry*, 2011, **21**, 15928–15934.

81 J. Kong, H. R. Tan, S. Y. Tan, F. Li, S. Y. Wong, X. Li and X. Lu, *Chemical Communications*, 2010, **46**, 8773.

82 S. Park, B. Kim and W. Lee, *Journal of Power Sources*, 2013, 239, 122–127.

83 J. Wang, Q. Zhang, X. Li, B. Zhang, L. Mai and K. Zhang, *Nano Energy*, 2015, **12**, 437–446.

84 Y. Yu, L. Gu, C. Wang, A. Dhanabalan, P. A. van Aken and J. Maier, *Angewandte Chemie International Edition*, 2009, **48**, 6485–6489.

85 Z. X. Deng, J. W. Tao, L. J. Zhao, W. Zhang, Y. B. Wang, H. J. Mu, H. J. Wu, X. X. Xu and W. Zheng, *Process Biochemistry*, 2020, **96**, 73–79.

86 J. T. McCann, M. Marquez and Y. Xia, *Journal of the American Chemical Society*, 2006, **128**, 1436–1437.

87 H. Liu, J. Bai, Q. Wang, C. Li, S. Wang, W. Sun and Y. Huang, *Nano*, 2014, **09**, 1450041.

88 I. Savva, A. S. Kalogirou, A. Chatzinicolaou, P. Papaphilippou, A. Pantelidou, E. Vasile, E. Vasile, P. A. Koutentis and T. Krasia-Christoforou, *RSC Advances*, 2014, **4**, 44911–44921.

89 X. Xiong, W. Luo, X. Hu, C. Chen, L. Qie, D. Hou and Y. Huang, *Scientific Reports*, 2015, **5**, 9254.

90 W. Li, L. Shi, K. Zhou, X. Zhang, I. Ullah, H. Ou, W. Zhang and T. Wu, *Journal of Materials Processing Technology*, 2019, **266**, 551–557.

91 T. V. Hughes and C. R. Chambers, *Manufacture of 0 N Filaments*, United States, United States, 1889.

92 L. Radushkevich and V. L. Chim, *Zurn. Fisic. Chim.*, 1952, **26**, 88–95.

93 H. W. Kroto, J. R. Heath, S. C. O'Brien, R. F. Curl and R. E. Smalley, *Nature*, 1985, **318**, 162–163.

94 S. Iijima, *Nature*, 1991, **354**, 56–58.

95 S. Iijima and T. Ichihashi, *Nature*, 1993, **363**, 603–605.

96 D. S. Bethune, R. D. Johnson, J. R. Salem, M. S. De Vries and C. S. Yannoni, *Nature*, 1993, **366**, 123–128.

97 R. T. K. Baker, M. A. Barber, P. S. Harris, F. S. Feates and R. J. Waite, *Journal of Catalysis*, 1972, **26**, 51–62.

98 R. T. K. Baker, R. B. Thomas and R. J. Waite, *Journal of Catalysis*, 1973, **30**, 86–95.

99 A. V. Melechko, V. I. Merkulov, T. E. McKnight, M. A. Guillorn, K. L. Klein, D. H. Lowndes and M. L. Simpson, *Journal of Applied Physics*, 2005, **97**, 41301.

100 B. Adeniran and R. Mokaya, *Journal of Materials Chemistry A*, 2015, **3**, 5148–5161.

101 W. L. Li, K. Lu and J. Y. Walz, *International Materials Reviews*, 2012, **57**, 37–60.

102 S. Samitsu, R. Zhang, X. Peng, M. R. Krishnan, Y. Fujii and I. Ichinose, *Nature Communications*, 2013, **4**, 2653.

103 X. Liu, A. Ahmed, Z. Wang and H. Zhang, *Chemical Communications*, 2015, **51**, 16864–16867.

104 X. Liu, Y. Zhang, X. Pang, E. Yue, Y. Zhang, D. Yang, J. Tang, J. Li, Y. Che and J. Zhao,

Journal of Physical Chemistry C, 2015, **119**, 6446–6452.

105 M. Faccini, G. Borja, M. Boerrigter, D. Morillo Martín, S. Martìnez Crespiera, S. Vázquez-Campos, L. Aubouy and D. Amantia, *Journal of Nanomaterials*, 2015, **2015**, 1–9.

106 V. Aravindan, J. Sundaramurthy, P. Suresh Kumar, Y.-S. Lee, S. Ramakrishna and S. Madhavi, *Chemical Communications*, 2015, **51**, 2225–2234.

107 P. Serp, M. Corrias and P. Kalck, *Applied Catalysis A: General*, 2003, 253, 337–358.

108 I. U. Din, M. S. Shaharun, A. Naeem, M. A. Alotaibi, A. I. Alharthi, M. A. Bakht and Q. Nasir, *Ceramics International*, 2020, **46**, 18446–18452.

109 S. Peng, L. Li, J. Kong Yoong Lee, L. Tian, M. Srinivasan, S. Adams and S. Ramakrishna, *Nano Energy*, 2016, 22, 361–395.

110 K. L. Klein, A. V. Melechko, T. E. McKnight, S. T. Retterer, P. D. Rack, J. D. Fowlkes, D. C. Joy and M. L. Simpson, *Journal of Applied Physics*, 2008, **103**, 1126.

111 C. M. Yoon, D. Long, S. M. Jang, W. Qiao, L. Ling, J. Miyawaki, C. K. Rhee, I. Mochida and S. H. Yoon, *Carbon*, 2011, **49**, 96–105.

112 Z. Hualei and C. Yunfa, *Rare Metals*, 2010, **29**, 333–338.

113 H. Ago, *Journal of Physical Chemistry B*, 1999, **103**, 8116–8121.

114 X. Zhou, Y. Wang, C. Gong, B. Liu and G. Wei, *Chemical Engineering Journal*, 2020, 402, 126189.

115 K. V. Rao, K. Jayaramulu, T. K. Maji and S. J. George, *Angewandte Chemie - International Edition*, 2010, **49**, 4218–4222.

116 A. Dobashi, J. Maruyama, Y. Shen, M. Nandi and H. Uyama, *Carbohydrate Polymers*,

2018, **200**, 381–390.

117 T. N. Phan, M. K. Gong, R. Thangavel, Y. S. Lee and C. H. Ko, *Journal of Alloys and Compounds*, 2019, **780**, 90–97.

118 M. S. Javed, C. Zhang, L. Chen, Y. Xi and C. Hu, *Journal of Materials Chemistry A*, 2016, **4**, 8851–8859.

119 S. Li, A. Gao, F. Yi, D. Shu, H. Cheng, X. Zhou, C. He, D. Zeng and F. Zhang, *Electrochimica Acta*, 2019, **297**, 1094–1103.

120 B. Tang, Y. He, J. Liu, J. Zhang, J. Li, J. Zhou, Y. Ye, J. Wang and X. Wang, *Dyes and Pigments*, 2019, **170**, 107643.

121 Y. Zhang, X. Chen, C. Wang, G. M. Roozbahani, H. C. Chang and X. Guan, *Biosensors and Bioelectronics*, 2020, **165**, 112289.

122 N. Zhang, Y. Wang, S. Leng, S. Xu, L. Zhang, Q. Wang, Q. Zhang and H. Y. Hu, *Talanta*, 2019, **205**, 120133.

123 M. S. Sreevidya and R. Pavithran, *Materials Today: Proceedings*, , DOI:10.1016/j.matpr.2020.05.231.

124 P. Philip, E. Tomlal Jose, J. K. Chacko, K. C. Philip and P. C. Thomas, *Polymer Testing*, 2019, **74**, 257–265.

125 C. Kim, Y. Il Jeong, B. T. N. Ngoc, K. S. Yang, M. Kojima, Y. A. Kim, M. Endo and J.-W. Lee, *Small*, 2007, **3**, 91–95.

126 Y. Yao, P. Liu, Q. Zhang, S. Zeng, S. Chen, G. Zou, J. Zou, X. Zeng and X. Li, *Materials Letters*, 2018, **231**, 159–162.

127 M. Culebras, H. Geaney, A. Beaucamp, P. Upadhyaya, E. Dalton, K. M. Ryan and M. N.

Collins, *ChemSusChem*, 2019, **12**, 4516–4521.

128 J. Cárdenas-Martínez, B. L. España-Sánchez, R. Esparza and J. A. Ávila-Niño, *Synthetic Metals*, 2020, **267**, 116436.

129 B. Bessaire, M. Mathieu, V. Salles, T. Yeghoyan, C. Celle, J. P. Simonato and A. Brioude, *ACS Applied Materials and Interfaces*, 2017, **9**, 950–957.

130 J. H. Jeong and B. H. Kim, *Journal of the Taiwan Institute of Chemical Engineers*, 2018, **84**, 179–187.

131 J. A. Puszkiel, J. J. Andrade-Gamboa and F. C. Gennari, in *Emerging Materials for Energy Conversion and Storage*, Elsevier, 2018, pp. 393–428.

132 M. Steilen and L. Jörissen, in *Electrochemical Energy Storage for Renewable Sources and Grid Balancing*, Elsevier Inc., 2015, pp. 143–158.

133 P. Breeze, in *Power System Energy Storage Technologies*, Elsevier, 2018, pp. 69–77.

134 J. Afonso, I. Catarino, R. Patrício, A. Rocaboy, M. Linder and G. Bonfait, *Cryogenics*, 2011, **51**, 621–629.

135 K. M. Khalil, A. Ahmad, S. Mahmoud and R. K. Al-Dadah, *Journal of Cleaner Production*, 2017, **164**, 606–617.

136 R. Dutta, P. Ghosh and K. Chowdhury, *Cryogenics*, 2017, **88**, 132–142.

137 I. Sarbu and C. Sebarchievici, *Sustainability*, 2018, **10**, 191.

138 I. Sarbu, C. Sebarchievici, I. Sarbu and C. Sebarchievici, *Chapter 4 – Thermal Energy Storage*, Academic Press, 2017.

139 J. Hu, H. Li and X. Huang, *Solid State Ionics*, 2005, **176**, 1151–1159.

140 M. Winter, J. O. Besenhard, M. E. Spahr and P. Novák, *Advanced Materials*, 1998, **10**, 725–763.

141 W. J. Zhang, *Journal of Power Sources*, 2011, 196, 13–24.

142 G. A. Nazri and G. Pistoia, *Lithium Batteries: Science and Technology*, Springer Scicence & Business Media, 2004.

143 X. Zuo, J. Zhu, P. Müller-Buschbaum and Y. J. Cheng, *Nano Energy*, 2017, 31, 113–143.

144 P. S. Pravin, S. Misra, S. Bhartiya and R. D. Gudi, *Journal of Process Control*, 2020, **87**, 147–165.

145 P. Jienkulsawad, D. Saebea, Y. Patcharavorachot and A. Arpornwichanop, *International Journal of Hydrogen Energy*, 2020, **45**, 835–848.

146 V. T. Giap, Y. S. Kim, Y. D. Lee and K. Y. Ahn, *Journal of Energy Storage*, 2020, **29**, 101434.

147 D. Saha, Y. Li, Z. Bi, J. Chen, J. K. Keum, D. K. Hensley, H. A. Grappe, H. M. Meyer, S. Dai, M. P. Paranthaman and A. K. Naskar, *Langmuir*, 2014, **30**, 900–910.

148 R. Farma, M. Deraman, I. Talib, R. Omar, J. Manjunatha, M. Ishak, N. Basri and B. Dolah, *International Journal of Electrochemical Science*, 2013, **8**, 257–273.

149 S. Zhou, X. Li, Z. Wang, H. Guo and W. Peng, *Transactions of Nonferrous Metals Society of China*, 2007, **17**, 1328–1333.

150 A. Borenstein, O. Hanna, R. Attias, S. Luski, T. Brousse and D. Aurbach, *Journal of Materials Chemistry A*, 2017, 5, 12653–12672.

151 N. Mishra, S. Shinde, R. Vishwakarma, S. Kadam, M. M. Sharon and M. M. Sharon, in

AIP Conference Proceedings, 2013, vol. 1538, pp. 228–236.

152 R. Amade, E. Jover, B. Caglar, T. Mutlu and E. Bertran, *Journal of Power Sources*, 2011, **196**, 5779–5783.

153 J. E. Zuliani, J. N. Caguiat, D. W. Kirk and C. Q. Jia, *Journal of Power Sources*, 2015, **290**, 136–143.

154 H. Tomiyasu, H. Shikata, K. Takao, N. Asanuma, S. Taruta and Y. Y. Park, *Scientific Reports*, 2017, **7**, 1–12.

155 A. Daraghmeh, S. Hussain, I. Saadeddin, L. Servera, E. Xuriguera, A. Cornet and A. Cirera, *Nanoscale Research Letters*, 2017, **12**, 639.

156 X. Liu, M. Naylor Marlow, S. J. Cooper, B. Song, X. Chen, N. P. Brandon and B. Wu, *Journal of Power Sources*, 2018, **384**, 264–269.

157 X. Lu, C. Wang, F. Favier and N. Pinna, *Advanced Energy Materials*, 2017, **7**, 1601301.

158 S. Hussain, R. Amade, E. Jover and E. Bertran, *Journal of Materials Science*, 2013, **48**, 7620–7628.

159 P. Mukherjee and V. V. Rao, *Physica C: Superconductivity and its Applications*, 2019, 563, 67–73.

160 H. S. Salama and I. Vokony, *Journal of Cleaner Production*, 2020, **260**, 121099.

161 A. Kumar, J. V. Muruga Lal Jeyan and A. Agarwal, in *Materials Today: Proceedings*, Elsevier Ltd, 2020, vol. 21, pp. 1755–1762.

162 P. Dan, E. Mengeritski, Y. Geronov, D. Aurbach and I. Weisman, *Journal of Power Sources*, 1995, **54**, 143–145.

163 V. Etacheri, R. Marom, R. Elazari, G. Salitra and D. Aurbach, *Energy & Environmental*

Science, 2011, **4**, 3243–3262.

164 J. P. Gabano, M. Broussely and M. Grimm, in *Batteries for Implantable Biomedical Devices*, Springer US, Boston, MA, 1986, pp. 181–213.

165 H. Wu, K. Wang, Y. Meng, K. Lu and Z. Wei, *Journal of Materials Chemistry A*, 2013, **1**, 6366–6372.

166 J. S. Cho, Y. J. Hong and Y. C. Kang, *ACS Nano*, 2015, **9**, 4026–4035.

167 S. Ren, X. Zhao, R. Chen and M. Fichtner, *Journal of Power Sources*, 2014, **260**, 205–210.

168 J. L. Domingo, *Reviews of Environmental Contamination and Toxicology*, 1989, 108, 105–132.

169 S. M. H. T. Nyberg, M. Cefola and D. Sabine, *Archives of Biochemistry and Biophysics*, 1959, **85**, 82–88.

170 M. Horn, J. MacLeod, M. Liu, J. Webb and N. Motta, *Economic Analysis and Policy*, 2019, **61**, 93–103.

171 M. Vangari, T. Pryor and L. Jiang, *Journal of Energy Engineering*, 2013, **139**, 72–79.

172 A. M. A. M. Namisnyk and J. G. Zhu, University of Technology, Sydney, 2003.

173 Y. Lu, K. Fu, S. Zhang, Y. Li, C. Chen, J. Zhu, M. Yanilmaz, M. Dirican and X. Zhang, *Journal of Power Sources*, 2015, **273**, 502–510.

174 H. Helmholtz, *Annalen der Physik*, 1853, **165**, 211–233.

175 B. E. Conway, J. O. M. Bockris and I. A. Ammar, *Transactions of the Faraday Society*, 1951, **47**, 756–766.

176 D. Qu, *Journal of Power Sources*, 2002, **109**, 403–411.

177 J. W. Yan, Z. Q. Tian and B. W. Mao, *Current Opinion in Electrochemistry*, 2017, 4, 105–111.

178 W. Hsieh, T. L. A. Horng, H. C. Huang and H. Teng, *Journal of Materials Chemistry A*, 2015, **3**, 16535–16543.

179 H. Yang and D. Zhao, *Journal of Materials Chemistry*, 2005, **15**, 1217–1231.

180 C. W. Huang, C. H. Hsu, P. L. Kuo, C. Te Hsieh and H. Teng, *Carbon*, 2011, **49**, 895–903.

181 C. Portet, G. Yushin and Y. Gogotsi, *Carbon*, 2007, **45**, 2511–2518.

182 C. Largeot, C. Portet, J. Chmiola, P. L. Taberna, Y. Gogotsi and P. Simon, *Journal of the American Chemical Society*, 2008, **130**, 2730–2731.

183 M. Zhi, C. Xiang, J. Li, M. Li and N. Wu, *Nanoscale*, 2013, **5**, 72–88.

184 Y. Wang and Y. Xia, *Advanced Materials*, 2013, **25**, 5336–5342.

185 J. Wei, J. Zhou, S. Su, J. Jiang, J. Feng and Q. Wang, *ChemSusChem*, 2018, **11**, 3410–3415.

186 Y. Jiang and J. Liu, *ENERGY & ENVIRONMENTAL MATERIALS*, 2019, **2**, 30–37.

187 B. E. E. Conway, V. Birss and J. Wojtowicz, *Journal of Power Sources*, 1997, **66**, 1–14.

188 I. Langmuir, *Journal of the American Chemical Society*, 1918, 40, 1361–1403.

189 M. S. Javed, J. Chen, L. Chen, Y. Xi, C. Zhang, B. Wan and C. Hu, *Journal of Materials Chemistry A*, 2015, **4**, 667–674.

190 *Topics in Fluorescence Spectroscopy*, Springer US, 2005.

191 *Advanced Concepts in Fluorescence Sensing*, Springer US, 2005.

192 L. Manjakkal, D. Szwagierczak and R. Dahiya, *Progress in Materials Science*, 2020, 109, 100635.

193 S. Zhuiykov, *Sensors and Actuators, B: Chemical*, 2012, 161, 1–20.

194 L. Manjakkal, C. G. Núñez, W. Dang and R. Dahiya, *Nano Energy*, 2018, **51**, 604–612.

195 W. Dang, L. Manjakkal, W. T. Navaraj, L. Lorenzelli, V. Vinciguerra and R. Dahiya, *Biosensors and Bioelectronics*, 2018, **107**, 192–202.

196 T. Guinovart, G. Valdés-Ramírez, J. R. Windmiller, F. J. Andrade and J. Wang, *Electroanalysis*, 2014, **26**, 1345–1353.

197 A. J. Bandodkar, V. W. S. Hung, W. Jia, G. Valdés-Ramírez, J. R. Windmiller, A. G. Martinez, J. Ramírez, G. Chan, K. Kerman and J. Wang, *Analyst*, 2013, **138**, 123–128.

198 J. Kim, T. N. Cho, G. Valdés-Ramírez and J. Wang, *Talanta*, 2016, **150**, 622–628.

199 K. Paek, H. Yang, J. Lee, J. Park and B. J. Kim, *ACS Nano*, 2014, **8**, 2848–2856.

200 H. Cao, V. Landge, U. Tata, Y. S. Seo, S. Rao, S. J. Tang, H. F. Tibbals, S. Spechler and J. C. Chiao, *IEEE Transactions on Biomedical Engineering*, 2012, **59**, 3131–3139.

201 N. Uria, N. Abramova, A. Bratov, F. X. Muñoz-Pascual and E. Baldrich, *Talanta*, 2016, **147**, 364–369.

202 V. M. Stippl, A. Delgado and T. M. Becker, *Innovative Food Science and Emerging Technologies*, 2004, **5**, 285–292.

203 E. Kress-Rogers, *Trends in Food Science and Technology*, 1991, 2, 320–324.

204 A. M. Gibson, N. Bratchell and T. A. Roberts, *International Journal of Food*

Microbiology, 1988, **6**, 155–178.

205 R. Martínez-Máñez, J. Soto, E. García-Breijo, L. Gil, J. Ibáñez and E. Gadea, *Sensors and Actuators, A: Physical*, 2005, **120**, 589–595.

206 V. K. Gupta, C. K. Jain, I. Ali, M. Sharma and V. K. Saini, *Water Research*, 2003, **37**, 4038–4044.

207 J. K. Atkinson, A. W. J. Cranny, W. V. Glasspool and J. A. Mihell, *Sensors and Actuators, B: Chemical*, 1999, **54**, 215–231.

208 M. Shamsipur, A. Barati and Z. Nematifar, *Journal of Photochemistry and Photobiology C: Photochemistry Reviews*, 2019, 39, 76–141.

209 S. Cheng, Q. Liu, X. Zhou, Y. Gu, W. Yuan, W. Feng and F. Li, *ACS applied materials & interfaces*, 2020, **12**, 25557–25564.

210 L. Wang, L. Wang, Y. Zhang, J. Pan, S. Li, X. Sun, B. Zhang and H. Peng, *Advanced Functional Materials*, 2018, **28**, 1804456.

211 Y. Jiao, X. Gong, H. Han, Y. Gao, W. Lu, Y. Liu, M. Xian, S. Shuang and C. Dong, *Analytica Chimica Acta*, 2018, **1042**, 125–132.

212 C. Wang, Q. Fu, X. Wang, D. Kong, Q. Sheng, Y. Wang, Q. Chen and J. Xue, *Analytical Chemistry*, 2015, **87**, 8227–8233.

213 Y. Zhang, X. Chen, G. M. Roozbahani and X. Guan, *Analyst*, 2019, **144**, 1825–1830.

214 Y. L. Qi, L. Guo, L. L. Chen, H. Li, Y. S. Yang, A. Q. Jiang and H. L. Zhu, *Coordination Chemistry Reviews*, 2020, 421, 213460.

215 D. S. Pisoni, L. Todeschini, A. C. A. Borges, C. L. Petzhold, F. S. Rodembusch and L. F. Campo, *Journal of Organic Chemistry*, 2014, **79**, 5511–5520.

216 D. K. Gupta, S. Chatterjee, S. Datta, V. Veer and C. Walther, *Chemosphere*, 2014, 108, 134–144.

217 J. J. Mortvedt, *Fertilizer research*, 1995, **43**, 55–61.

218 N. Defarge, J. Spiroux de Vendômois and G. E. Séralini, *Toxicology Reports*, 2018, **5**, 156–163.

219 N. S. Shaban, K. A. Abdou and N. E.-H. Y. Hassan, *Beni-Suef University Journal of Basic and Applied Sciences*, 2016, **5**, 102–106.

220 A. Barhoum and M. Luisa García-Betancourt, in *Emerging Applications of Nanoparticles and Architectural Nanostructures: Current Prospects and Future Trends*, Elsevier Inc., 2018, pp. 279–304.

221 P. Senthil Kumar, K. Grace Pavithra and M. Naushad, in *Nanomaterials for Solar Cell Applications*, Elsevier, 2019, pp. 97–124.

222 H. Itagaki, in *Experimental Methods in Polymer Science: Modern Methods in Polymer Research and Technology*, Elsevier Inc., 2012, pp. 155–260.

223 S. Hänselmann and D. P. Herten, in *Encyclopedia of Spectroscopy and Spectrometry*, Elsevier, 2016, pp. 84–88.

224 D. Skoog, F. Holler and S. Crouch, *Principles of instrumental analysis*, 2017.

225 R. Krishna, T. J. Unsworth and R. Edge, in *Reference Module in Materials Science and Materials Engineering*, Elsevier, 2016.

226 N. John and S. George, in *Spectroscopic Methods for Nanomaterials Characterization*, Elsevier, 2017, vol. 2, pp. 95–127.

227 I. Childres, L. A. Jauregui, W. Park, H. Cao and Y. P. Chen, *RAMAN SPECTROSCOPY OF*

GRAPHENE AND RELATED MATERIALS, .

228 D. Lin-Vien, N. B. Colthup, W. G. Fateley and J. G. (Professor) Grasselli, *The Handbook of infrared and raman characteristic frequencies of organic molecules*, Academic Press, 1991.

229 A. Cuesta, P. Dhamelincourt, J. Laureyns, A. Martínez-Alonso and J. M. D. Tascón, *Carbon*, 1994, **32**, 1523–1532.

230 A. Dutta, in *Spectroscopic Methods for Nanomaterials Characterization*, Elsevier, 2017, vol. 2, pp. 73–93.

231 L. Mino, L. Mandrile, L. Iannarelli, C. Portesi, G. Martra and A. M. Rossi, in *Characterization of Nanoparticles: Measurement Processes for Nanoparticles*, Elsevier, 2019, pp. 457–480.

232 R. K. Mishra, J. Cherusseri, A. Bishnoi and S. Thomas, in *Spectroscopic Methods for Nanomaterials Characterization*, Elsevier, 2017, vol. 2, pp. 369–415.

233 J. A. Sanders, in *Functional Brain Imaging*, Elsevier, 1995, pp. 419–467.

234 G. A. Pearson, *Shimming an NMR Magnet*, Iowa, 1991.

235 F. L. Holmes, *Isis*, 1963, **54**, 50–81.

236 S. Loganathan, R. B. Valapa, R. K. Mishra, G. Pugazhenthi and S. Thomas, in *Thermal and Rheological Measurement Techniques for Nanomaterials Characterization*, Elsevier, 2017, vol. 3, pp. 67–108.

237 J. Abraham, A. P. Mohammed, M. P. A. Kumar, S. C. George and S. Thomas, in *Characterization of Nanomaterials: Advances and Key Technologies*, Elsevier, 2018, pp. 213–236.

238 S. Brunauer, P. H. Emmett and E. Teller, *Journal of the American Chemical Society*, 1938, **60**, 309–319.

239 K. S. W. Sing, *Advances in Colloid and Interface Science*, 1998, **76**–**77**, 3–11.

240 J. I. Goldstein, D. E. Newbury, J. R. Michael, N. W. M. Ritchie, J. H. J. Scott and D. C. Joy, *Scanning Electron Microscopy and X-Ray Microanalysis*, Springer New York, New York, NY, 2018.

241 L. Reimer, *Measurement Science and Technology*, 2000, **11**, 1826.

Chapter 2 Methodology

2.1 Preparation of Materials

Perylene-1,3,9,10-tetracarboxylic anhydride (97 %), 5-aminoisophthalic acid (94 %), imidazole (≥99.5 %), sodium hydroxide (≥97 % pellets), hydrochloric acid (37 %), glucono-δ-lactone (≥ 99 %), polyacrylonitrile (M_W = 150 000 g.mol^{-1}), polyethylene glycol (M_W = 400 000 g.mol^{-1}), phosphoric acid (≥85 wt.%), iron (III) nitrate nonahydrate (≥98%), copper (II) nitrate trihydrate (99%), glucono-δ-lactone (GdL) (≥ 99%), titanium (III) chloride (12 wt.%), copper (II) chloride dihydrate (reagent grade), iron (II) chloride tetrahydrate (98%), iron (III) chloride hexahydrate (97%), zinc (II) nitrate hexahydrate (98%), and cobalt (II) acetate tetrahydrate (≥98%), potassium hydroxide (≥85%), sodium sulfate (≥99%), sulfuric acid (95%), phosphoric acid (≥85%), triethylamine (TEA) (≥99%), N,N-dimethylformamide (DMF) (99.8%), N-methyl pyrrolidone (NMP) (99.5%), and polyvinylidene fluoride (PVDF) (MW ~180 0000 g.mol^{-1}) were purchased from Sigma-Aldrich and used without further purification. Cobalt (II) gluoconate (98%) was purchased from AK Scientific and used as received. Ethanol (≥ 99.9 %) was obtained from Brenntag and used as received.

2.1.1 Synthesis of perylene-3,4,9,10-tetracarboxylic diimide-N,N-isophthalic acid (PDI):

Perylene-1,3,9,10-tetracarboxylic dianhydride (PTCDA) (2.0 g, 0.00278 moles), 5-aminoisophthalic acid (1.26 g, 0.00695 moles), and imidazole (16 g , 0.235 moles) were added to a 50 mL round-bottomed flask attached to a condenser which was then purged with Nitrogen gas for 20 minutes before heating to 127 °C for 6 hours. 20mL deionized water was added to the hot mixture and allowed to cool to room temperature naturally. The mixture was filtered under vacuum and the product-containing filtrate collected. To the

aqueous mixture, hydrochloric acid (2.5 M, 100 mL) in ethanol was added and the resulting mixture filtered under vacuum and washed further with ethanol. ^{1}H NMR in d^{6}-DMSO was performed to ensure the correct product was obtained as well as to confirm purity. In the case of an impure product caused by the presence of residual reaction solvent, imidazole, a further recrystallisation was conducted by adding aqueous sodium hydroxide (2.5 M) until PDI was completely dissolved, then adding aqueous hydrochloric acid (2.5 M). PDI was precipitated out due to its insolubility in acidic conditions and removed via filtration and washed with ethanol before drying under vacuum at 60 °C.

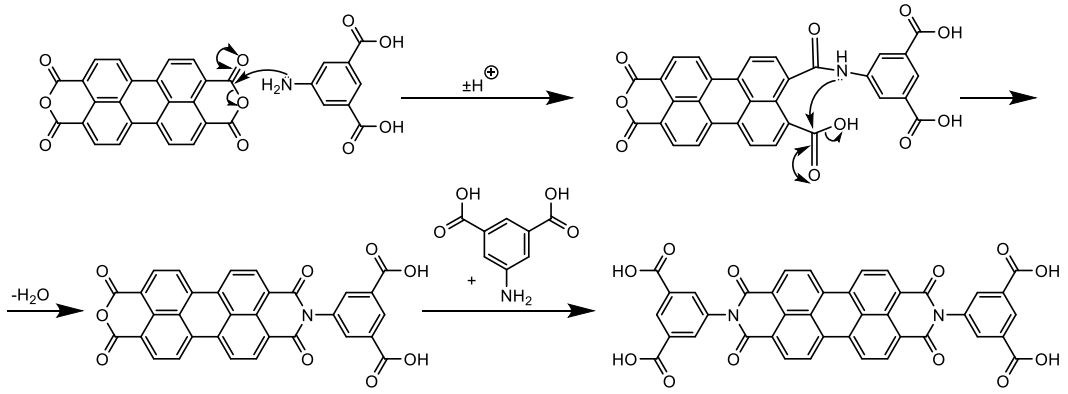

Figure 2.1 Mechanism of PDI synthesis

2.1.2 Self-assembly

2.1.2.1 pH-Triggered Self-Assembly

In concentrations stated in **Table 3.3**, perylene-3,4,9,10-tetracarboxylic diimide-N,N-isophthalic acid (PDI) powder was weighed out into a sample vial for addition of pre-dissolved alkali in water. PDI solutions were stirred and left to stand until no precipitate could be observed after 30 minutes. A concentration of acidic solution was made up separately, corresponding to 1.2 equivalents of base present in the PDI solution. The mixture was left to stand for 2 hours while undergoing self-assembly before dry fibres were isolated.

2.1.2.2 Solvent-Phase Interfacial Self-Assembly

In amounts stated in **Table 3.3**, PDI powder was weighed into a clean glass vial to which, pre-dissolved alkali in water was added. PDI solutions were stirred until no precipitate was present after 30 minutes of standing. Poor solvent addition was performed using an equivalent volume of water-miscible solvent to the initial PDI solution. Solvent was gently pipetted onto the surrounding glass walls to prevent disturbance of the initial solution and to ensure diffusion would be the primary mixing factor. This mixture was left to stand for 2 hours before dry fibres could be isolated.

2.1.2.3 Isolating Dry Fibres

Self-assembled fibres were isolated from their aqueous solutions initially using lyophilisation in which the samples were frozen rapidly using liquid Nitrogen before being transferred to a Virtis AdVantage freeze drier for 48 hours at -90°C. Subsequent fibres were isolated by gravimetric filtration and washed with water and ethanol before oven drying at 60°C overnight.

2.1.3 Electrospinning

Electrospinning parameters were determined for each individual solution and were achieved initially by setting the syringe pump to a flow rate such that when the bead of solution is wiped away from the needle tip, another bead takes its place almost instantly. Once the flow rate is established, applied voltage is gradually increased until a Taylor cone eruption can be observed. Voltage was supplied from a 40 kV / 15 W M40 high voltage generator from Linari engineering. Flight distance was set at 15 cm from the needle tip to the collector which was wrapped in Aluminium foil and attached to a ground.

2.1.4 Carbonisation conditions

Samples were carbonised using a Carbolite tube furnace in a ceramic work tube supplied with a continuous flow of Nitrogen gas supplied from a cylinder at atmospheric pressure. Materials placed in an alumina crucible, supplied by Almath crucibles, (15 mL, 102 x 20 x 14 mm) were degassed initially at room temperature for 30 minutes before the temperature was ramped at a rate of 2°C/min until the temperature reached 200°C. Temperature was held for 2 hours then ramped up again, this time at a rate of 3°C/min until the subsequent carbonisation temperature of 800°C was reached and held for a further 2 hours. At the end of the heating cycle, the tube furnace was allowed to cool naturally to room temperature. Samples were removed and weighed for yield.

2.2 Sensing

2.2.1 Measuring sensitivity of aqueous PDI solutions to the presence of M^{n+} ions.

PDI (10 mM) was dissolved in aqueous sodium hydroxide solution (0.02 M, 10 mL) then further diluted to 10 µM. PDI solution (2 mL) in a cuvette was measured via UV-Vis absorbance between 350 – 800 nm. Successive addition of metal solution using chloride salts during preparation. Concentrations were back-calculated and absorbances measured relative to initial PDI absorbance.

2.3 Electrochemical Testing

2.3.1 Cyclic Voltammetry

A slurry of active material (90%) and polyvinylidene fluoride (PVDF) pellets (10%) were combined to a concentration of 1 $mg.cm^{-3}$ in N-methyl pyrrolidone (NMP). An accurate volume of 11 µL was pipetted onto the surface of a 1 cm^2 carbon disc and the NMP allowed to evaporate in an oven overnight. The coated carbon disc was assembled into an electrode

using copper wire and a PTFE tape coating, leaving only the coated face of the electrode exposed to the electrolyte.

A three-electrode system was used with a working electrode, a platinum wire counter electrode, and a Ag/AgCl reference electrode attached to a CHI 660D electrochemical analyser for measurement recordings.

$$C_{sp} = \frac{\int IdV}{\Delta V.v.m} \quad (1)$$

Data analysis was performed by calculating an average area under the curves for positive and negative sweeps using Equation (1). C_{sp} is specific capacitance, $\int I\, dV$ is an integration representing the area under the potential/current curve, ΔV is the potential window, v is the sweep rate, m is the mass of active material.

2.3.2 Li-ion Battery Testing

A slurry of active material (80 wt. %), PVDF (10 wt. %), and carbon black (10 wt. %) in NMP was made up. The active material slurry was deposited onto a copper current collector uniformly using a razor blade and dried at 100°C for 4 hours in air. The dry coated foil was pressed under a load of ~1000 kg before discs were punched out from the foil and weighed. 2032 button cells were assembled as seen in **Figure 2.2**, in an argon glove box using lithium foil as a counter electrode and $LiPF_6$ (1 M) as the electrolyte.[30,31]

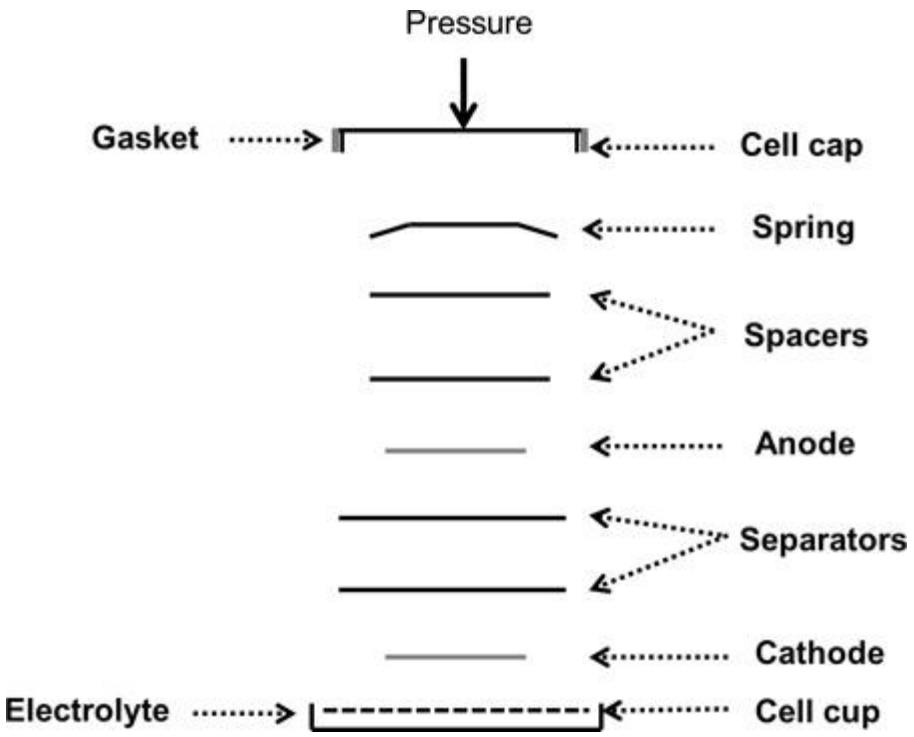

Figure 2.2 Assembly of a coin cell.[1]

Charge-discharge curves were measured at current density 50 mA.g^{-1} with a PGSTAT302, Autolab. The coin cell was charged between 0.0 – 3.0 V for 6 cycles.

2.4 Characterisation

2.4.1 Fluorescence Spectroscopy

Fluorescence measurements were recorded at 90° from the incident light using a Shimadzu RF-5301PC. Sample solutions were placed in a clean 4 mL quartz cuvette and measurements taken at 1 nm intervals. Excitation was achieved with light of wavelength 350 nm and measurements were recorded between 350 – 800 nm.

2.4.2 Ultraviolet – Visible Spectrophotometry, UV-Vis

UV-Vis measurements were recorded on a Shimadzu UV-vis 3600 in plastic 4 mL cuvettes from aqueous solutions, with a water baseline solution. Complete scans were recorded

between 300 – 800 nm. Where sensing measurements were used stimuli solutions were pipetted directly into the cuvette and the complete solution was mixed using trituration.

2.4.3 Raman spectroscopy

Raman spectroscopy was conducted on a Renishaw inVia Reflex Qontor Confocal Raman Microscope with a 532 nm laser at 5% power, 2400 $l.mm^{-1}$ grating, Renishaw Centrus 5134M5 detector. Samples were placed aluminium slide and brought into focus using the attached microscope. Measurements were recorded for 10 seconds as an initial sample scan, before scanning for a duration of 1 second at a new location for each scan.

2.4.4 Fourier Transform Infrared Spectroscopy, FTIR

Samples were tested using a Perkin Elmer Spectrum 2000 infrared spectrometer with microscope attachment with Autoimage. For Fourier transform, spectroscopy samples were prepared prior to testing by mixing with KBr and manually grinding into a powder using a pestle and mortar. The powder was pressed into a transparent disc with a Specac manual hydraulic press. FTIR transmission spectroscopy was measured between 4000 – 600 cm^{-1} at 1 cm^{-1} intervals for 16 scans to reduce signal to noise ratio.

2.4.5 Nuclear Magnetic Resonance Spectroscopy, NMR

Samples were prepared by dissolving in deuterated dimethyl sulfoxide ($[D_6]$DMSO) in a sample vial before transferring via syringe and syringe filter to a standard 5 mm glass tube. ^{1}H NMR spectra were recorded using a JEOL JNM-ECZR 500 MHz. 64 scans were performed for each sample to resolve signals enough to be measured.

2.4.6 Elemental Analysis, CHNX

Between 2-3 mg of sample was weighed accurately into an aluminium capsule and folded to seal in the sample sufficiently preventing loss of mass during movement. Samples were

placed into the autosampler of a Thermo Scientific Flash 1112 series elemental analyser for combustion analysis at 950 °C.

2.4.7 Thermogravimetric Analysis, TGA

TGA was conducted using TA Instruments' Q500 analyser to isolate temperature segments at which mass loss could be attributed to specific functional groups. Between 3 – 5 mg was weighed accurately into an alumina crucible. The filled crucible was placed onto the sample loader and zeroed before the heating program was run. The heating program used a temperature ramp rate of 10°C.min^{-1} to a maximum temperature of 800°C. The gas flow used was either nitrogen or air.

2.4.8 Brunauer-Emmett-Teller Analysis, BET

The BET equation (2) was used to calculate specific surface area of samples.

$$\frac{1}{V[\left(p^*/p\right)-1]} = \frac{(c-1).(p^*/p)}{c.V_{mono}} + \frac{1}{c.V_{mono}} \quad (2)$$

In which, V is the volume of gas adsorbed (cm^{-3}), p is absolute pressure (N.m^{-2}), $p*$ is absolute pressure (N.m^{-2}), V_{mono} is the volume of gas adsorbed (cm^{-3}) as a monolayer to the surface of the material, and c is the BET constant.

The resulting BET equation, Eq (2), was then used to calculate specific surface area using a plot of relative pressure, $\frac{1}{\mathrm{V}[(p^*/p)-1]}$, against, $\frac{p}{p^*}$, from which the linear range was identified and used to calculate the volume of gas required to form a monolayer, V_{mono}, on the surface using the slope, $\frac{(c-1)}{c.V_{mono}}$, and y-intercept, $\frac{1}{\mathrm{c}.V_{mono}}$. Using the volume of a monolayer of adsorbant, the area occupied by gas molecules was calculated by assuming the gas behaves

ideally. Thus, using the ideal gas equation (3) and equation (4), the surface area of the material was calculated.

$$p.V_{mono} = n.R.T \tag{3}$$

Since the gas used is assumed to be obeying ideal conditions, it is possible to use the ideal gas law (equation 3) to calculate the number of moles of N_2 adsorbed onto the surface. Where *n* is the number of moles, *R* is the ideal gas constant, 8.314 $J.mol^{-1}.K^{-1}$, and *T* is temperature in Kelvin.

$$S_A = (n.N_A.A) \tag{4}$$

Using the result calculated using equation 3, the surface area, S_A (m^2) may be calculated using Avogadro's number, N_A, 6.022×10^{23} mol^{-1}, the cross-sectional area of a single molecule of N_2, *A*, 1.62×10^{-19} m^2. This surface area may be divided by the mass of the sample used to provide the specific surface area for the material.

Measurements were performed using an ASAP 2020 Automatic High Resolution Micropore Physisorption Analyser by placing material in sample tubes for a degas sequence at 150°C for 10 hours at which time the samples were dried under vacuum.

$$Relative\ \%\ error = \frac{(\Delta I + \Delta m)}{(I + \Delta I + m + \Delta m)} \tag{5}$$

Errors were calculated using error values generated during calculation of the linear intercept and slope of isotherms, and combined using equation (5) which provided the relative percentage error and could be applied to the measurement values individually. In which, *I* and *m* refer to the linear isotherm intercept and gradient respectively.

2.4.9 Field Emission Scanning Electron Microscopy, FESEM

Morphology of materials generated were observed under a JEOL JSM6700F FESEM. Before imaging, samples were coated in a thin layer of gold by sputtering for 30 seconds. Samples were secured to a sample holder using carbon tape as a physical fixture. The sample holder was placed in the chamber and the air evacuated before pushing the sample holder into the path of the 5 kV electron beam. The working distance was set at 8.0 mm and the image brought into focus from there.

2.5 References

1 A. Kayyar, J. Huang, M. Samiee and J. Luo, Construction and Testing of Coin Cells of Lithium Ion Batteries, *J. Vis. Exp.*, 2012, **e4104**, 1–5.

Chapter 3 Self-Assembly and Electrospinning of Perylene Diimide Derived Carbon Nanofibres

3.1 Introduction

High surface area to volume ratio, surface functionality, and superior mechanical properties are some of the desirable characteristic achievable by materials which can be reduced to the nanoscale. Carbon nanofibres (CNFs) fall into such materials and while their synthetic methods are varied, greater environmental conscientiousness is desired in their production. Supramolecules are molecular assemblies held together by intermolecular forces rather than covalent bonding.[1–4] They are capable of forming highly ordered and complex systems without complex synthetic routes that accompany covalent bonds.[5–8]

Chemical modification to Perylenetetracarboxylic dianhydride (PTCDA) using side-group functionalisation at the imide N,N' positions is the simpler of two methods (imide substitution and bay additions) to change properties of the parent molecule.[9–12] Modifications at bay positions often affect electronic properties to a greater degree than substitution at the two imide positions since the imide positions are the nodes of the HOMO and LUMO orbitals of the molecule.[9–12]

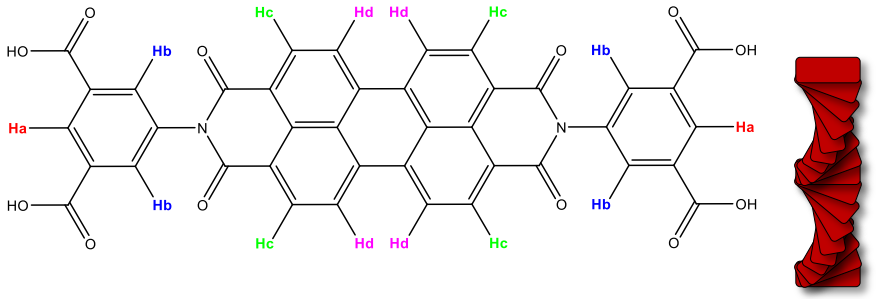

Figure 3.1 Perylene diimide derivative (PDI) molecular structure with NMR active protons recorded (left) and it's theoretical helical stacking arrangement (right) using isophthalic acid N-substitutions.[3,13]

Unlike applications in the pigment industry where insoluble PDIs are a desirable characteristic supramolecular self-assembly requires facile solubility in common solvents.[12,14,15] Bulky substituents added to imide positions inhibit π-π stacking to a greater or lesser amount depending on the substitute, allowing a degree of tunability.[11,16,17] Due to the central π-system, with suitable solvent and triggering systems, PDIs are capable of self-assembly into one-dimensional fibres.[18–20]

Electrospinning provides a facile method of fibre production on the nano-scale. The method eases incorporating active materials into precursor solutions to produce hybrid fibres with tunable properties.[21–26] Electrospinning as a production method typically results in non-woven fibrous mats which have been applied in medical[27,28] and food packaging[29,30] applications.

In this chapter the self- assembly through both pH-triggering and bulk solvent interfaces are explored for the PDI molecule depicted in **Figure 3.1**, building on previous group member's work.[31–33] In addition, electrospinning processes are utilised to explore novel evaporation-induced self-assembly routes and characterisation of the resulting materials, including the efficacy of methods for production of carbon nanofibres.

3.3 Experimental

3.3.1 Chemicals and Materials

Perylene-3,4,9,10-tetracarboxylic anhydride (97%), 5-aminoisophthalic acid (94%), imidazole (≥99.5%), sodium hydroxide (≥97% pellets), hydrochloric acid (37%), phosphoric acid (≥85 wt.%), iron (III) nitrate nonahydrate (≥98%), copper (II) nitrate trihydrate (99%), glucono-δ-lactone (GdL) (≥ 99%), polyacrylonitrile (PAN) (M_W = 150 000 $g.mol^{-1}$), polyethylene glycol (PEG) (M_W = 400 000 $g.mol^{-1}$) were purchased from Sigma-Aldrich and used without further purification. Ethanol (≥ 99.9%) was obtained from Brenntag and used as received.

3.3.2 Synthesis of perylene-3,4,9,10-tetracarboxylic diimide-N,N-isophthalic acid (PDI)

Perylene-3,4,9,10-tetracarboxylic acid dianhydride (PTCDA) (0.2 g), 5-aminoisophthalic acid (0.23 g) and, imidazole (1.6 g) at 127°C for 6 hours under Argon atmosphere. Water was added to the hot mixture and stirred while cooling to room temperature. Mixture was filtered, and the product precipitated from the filtrate using hydrochloric acid (2.4 M) in ethanol. Product isolated by filtering and washed with ethanol until the filtrate was neutral, then dried at 60°C.

3.3.3 Self-Assembly Conditions

Table 3.1 Samples of self-assembled PDI fibres (**SP**) and their conditions of formation. Fibre diameters were measured as an average directly from SEM images using Image J software.

Sample	Conditions	Diameter (nm)		Carbonisation % Yield
		Bef.	Aft.	
SP.3.1	[PDI (10mM), NaOH (0.06M), water (3 mL)] + *[H_3PO_4 (0.03 M), GdL (0.035 M), water (3 mL)]*	N/A	N/A	N/A
SP.3.2	[PDI (6mM) NaOH (0.036M), water (1.5 mL)] + *[GdL (0. 44 M) water (1.5 mL)]*	23	N/A	32.70%
SP.3.3	[PDI (60 mM), Imidazole (0.06 M), water (5 mL)] + *[GdL (0.17 M), water (5 mL)]*	75	N/A	31.35%
SP.3.4	[PDI (60 mM), Imidazole (0.72 M), water (3.3 mL)] + *[GdL (0.72 M), water (3.3 mL)]*	43	N/A	N/A
SP.3.5	[PDI (60 mM), Imidazole (0.72 M), water (3.3 mL)] + *[GdL (0.72 M), water (3.3 mL)]*	41	N/A	N/A
SP.3.6	[PDI (60 mM), Imidazole (0.24 M), water (4 mL)] + *[Gdl (0.28 M), water (4 mL)]*	61	52	57.63%
SP.3.7	[PDI (60 mM), Imidazole (0.24 M), water (1 mL)] + *[$Fe(NO)_3$ (0.06 M),GdL (0.56 M), water (3 mL)]*	38	47	48.68%
SP.3.8	[PDI (60 mM), Imidazole (0.24 M), water (3 mL)] + e*thanol (3 mL)*	117	N/A	N/A
SP.3.9	[PDI (60 mM), Imidazole (0.24 M), water (3 mL)] + *[$Fe(NO)_3$ (0.056 M), ethanol (3 mL)]*	69	N/A	N/A
SP.3.10	[PDI (60 mM), Imidazole (0.24 M), water (3 mL)] + *[$Cu(NO_3)_2.3H_2O$ (0.056 M), ethanol (3 mL)]*	88	43	39.10%

3.3.3.1 pH-Triggered Self-Assembly

In concentrations stated in **Table 3.1**, perylene-3,4,9,10-tetracarboxylic diimide-N,N-isophthalic acid (PDI) powder was weighed out into a sample vial for addition of pre-dissolved alkali in water. PDI solutions were stirred and left to stand until no precipitate

could be observed after 30 minutes. A concentration of acidic solution was made up separately, corresponding to 1.2 equivalents of base present in the PDI solution. The mixture was left to stand for 2 hours while undergoing self-assembly before dry fibres were isolated.

3.3.3.2 Solvent-Phase Interfacial Self-Assembly

In amounts stated in **Table 3.1**, PDI powder was weighed into a clean glass vial to which, pre-dissolved alkali in water was added. PDI solutions were stirred until no precipitate was present after 30 minutes of standing. Poor solvent addition was performed using an equivalent volume of water-miscible solvent to the initial PDI solution. Solvent was gently pipetted onto the surrounding glass walls to prevent disturbance of the initial solution and to ensure diffusion would be the primary mixing factor. This mixture was left to stand for 2 hours before dry fibres could be isolated.

3.3.3.3 Isolating Dry Fibres

Self-assembled fibres were isolated from their aqueous solutions initially using lyophilisation in which the samples were frozen rapidly using liquid Nitrogen before being transferred to a Virtis AdVantage freeze drier for 48 hours at -90°C. Subsequent fibres were isolated by gravimetric filtration and washed with water and ethanol before oven drying at 60°C overnight.

3.3.4 Electrospinning Conditions

Samples were made up using amounts listed in **Table 3.3** and loaded into a 5 mL plastic syringe fitted with a flat-tipped .22 gauge stainless steel needle with 0.41 mm inner diameter. A syringe pump was calibrated using the mass of water measured at time intervals with constant flow rate. The speed of the pump was calculated by using the cross-

sectional area of the 5 mL syringe used and could be used to calculate flow rate for different syringe sizes.

3.3.5 Carbonisation Conditions

Dry fibres were weighed into an alumina crucible and placed, uncovered, into the centre of a tube furnace. Samples were degassed for 30 minutes prior to heating using a gentle flow of N_2 and a mineral oil airlock. The tube furnace was then heated at a rate of 2°C.min^{-1} to a temperature of 200°C and held at that temperature for 2 hours, then heated further to 800°C at a rate of 3°C.min^{-1} and held for another 2 hours before being allowed to cool naturally and weighed for yield.

3.3.6 Materials Characterisation

Synthesised materials were characterised primarily using ^{1}H NMR spectra recorded using a JEOL JNM-ECZR 500 MHz. PDI powder was dispersed in deuterated dimethyl sulfoxide ([D_6]DMSO) in a sample vial before being transferred via syringe and syringe filter to a standard 5 mm tube. CHNX analysis was performed using an elemental analyser, Flash 1112 series with samples enveloped in aluminium capsules beforehand. FTIR spectra were recorded using a Perkin Elmer Spectrum 2000 with Autoimage by grinding samples with potassium bromide and pressing into a disc using a Specac manual hydraulic press. UV-Visible spectra were recorded in plastic cuvettes using a Shimadzu UV-vis 3600 spectrometer. SEM images were recorded on a JEOL FESEM JSM6700F and used to image fibres and their diameters were measured using Image J software. BET surface area analysis and degassing was performed using a Micrometrics ASAP 2020 surface area and porosity analyser with Nitrogen gas.

3.4 Results and Discussion

3.4.1 Characterisation of perylene-3,4,9,10-tetracarboxylic diimide-N,N-isophthalic acid (PDI)

PDI was synthesised as has been presented previously using imidazole as a solvent and 5-aminoisophthalic acid as the primary amine for N,N' substitution.[11,12,17,34] The mechanism for this reaction is suggested in **Scheme 3.1** as a nucleophilic substitution at a δ+ carbon either side of the anhydride. As the molecule is symmetrical, both carbons are equivalent.

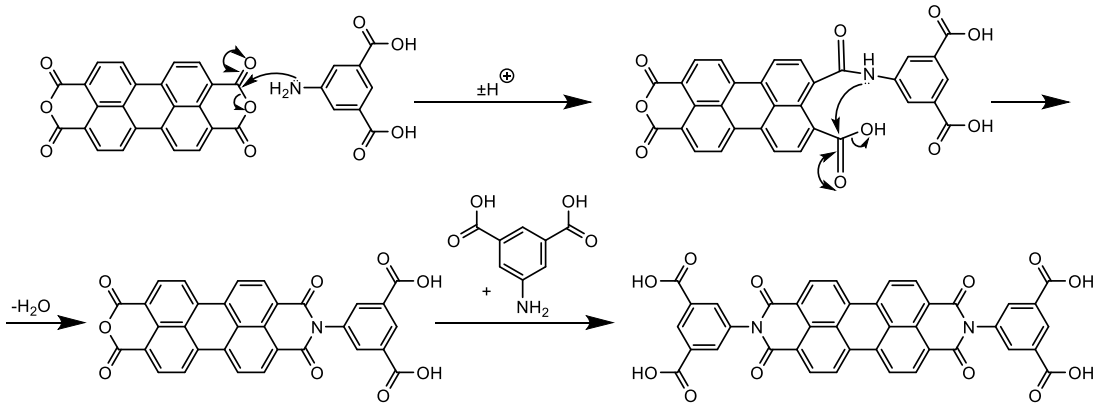

Scheme 3.1 Mechanism of N-substitution at PTCDA anhydrous groups using 5-aminoisophthalic acid and imidazole as a solvent.

Due to its planar nature, the perylene molecule in **Figure 3.1** is symmetrical in x, y, and z planes and thus, there are only four different aromatic Hydrogen environments. The Hs present within the carboxylic acid groups are all equivalent and only visible in ^{1}H NMR when using an aprotic solvent.

The synthesis used was presented previously and post-synthetic purification consisted solely of washing and filtering with ethanol. Using this procedure, it was found that a significant proportion of material collected contained imidazole impurities (**Appendix A.1**), due to trapping by PDI as a result of rapid precipitation using large quantities of ethanol. As such, an extra step was added into the purification. By filtering the product after adding

hydrochloric acid into the reaction mixture, PDI of higher purity could be obtained before the subsequent washing step with ethanol.

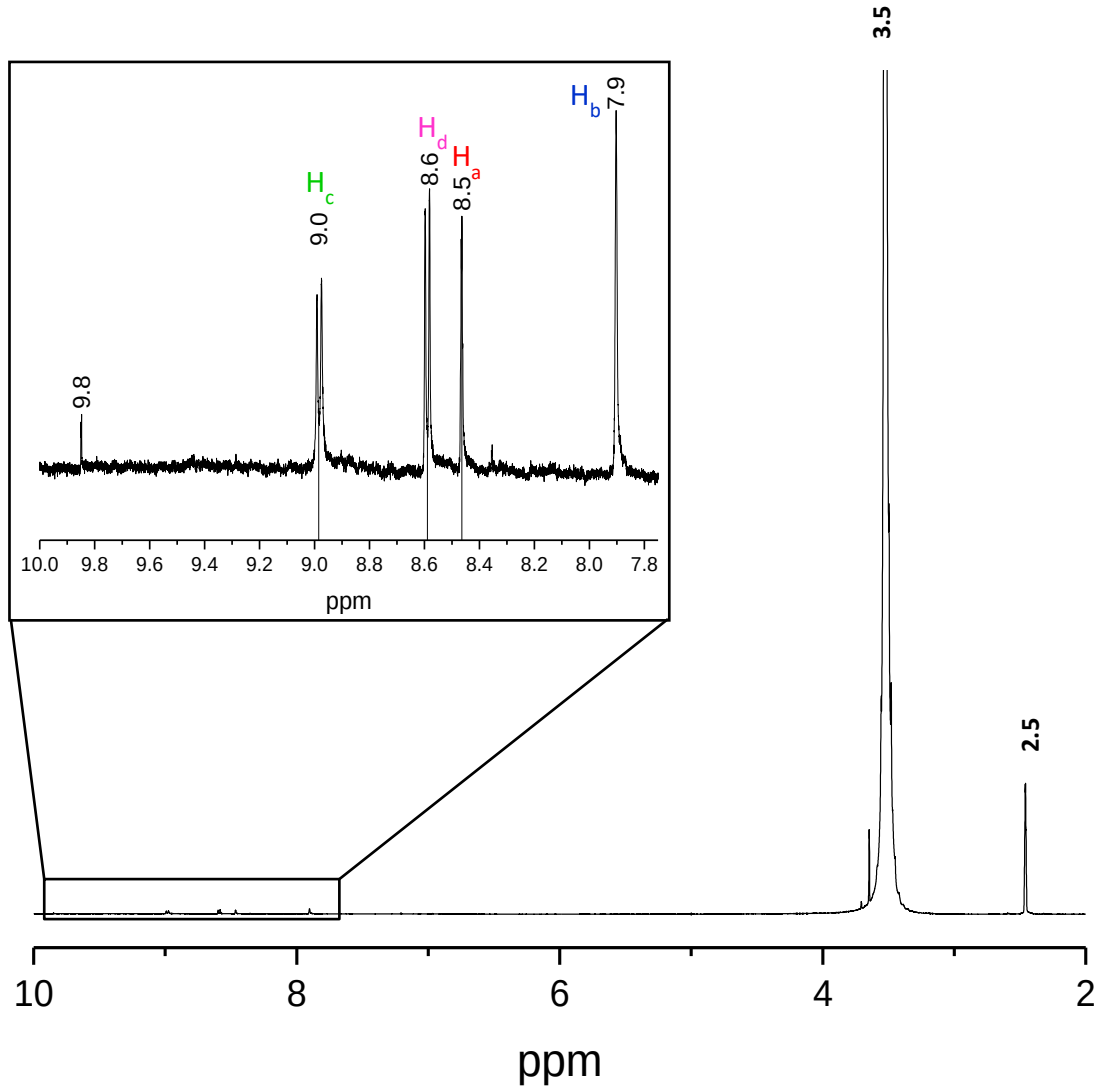

Figure 3.2 ^{1}H NMR of PDI in d^{6}-DMSO with a zoomed in section to highlight characteristic PDI peaks

Purity was measured primarily using ^{1}H NMR in d^{6}-dimethyl sulfoxide (DMSO) as shown in **Figure 3.2**. Due to limited solubility of PDI in DMSO, characteristic proton signals on aromatic carbon rings were observed very weakly within 7.9 – 9.8 ppm while peaks at 3.5 ppm and 2.5 ppm were attributed to water and non-deuterated DMSO respectively. Since

the PDI was dried in an oven before sample preparation, water was present in the NMR solvent which is due to the very hygroscopic nature of DMSO.

Signals at 9.0 ppm and 8.6 ppm were attributed to protons on the core perylene molecule and differentiated from each other by their chemical shift, with the higher frequency signal, 9.0 ppm, attached to equivalent protons marked H_c in **Figure 3.1** due to decreased nuclear shielding on the proton next to the amide group and an integration value equivalent to 4 protons. The second doublet at 8.6 ppm was assigned to proton H_d due to ^3J coupling and an integration value of 4 protons. H_a was assigned to the signal at 8.5 ppm due to an integration value half of the other signals in the same region indicating only 2 equivalent protons and no coupling indicating a proximity within three bonds of another spin active nuclei. The final signal associated with the target perylene molecule at 7.9 ppm was attributed to H_b due to its singlet nature and integration value calculated at 4 equivalent protons. A very weakly observed, broader signal at 9.8 ppm was assigned to the proton found on the carboxylic acid groups, however due to the large presence of water its integration value was not applicable to the PDI molecule.

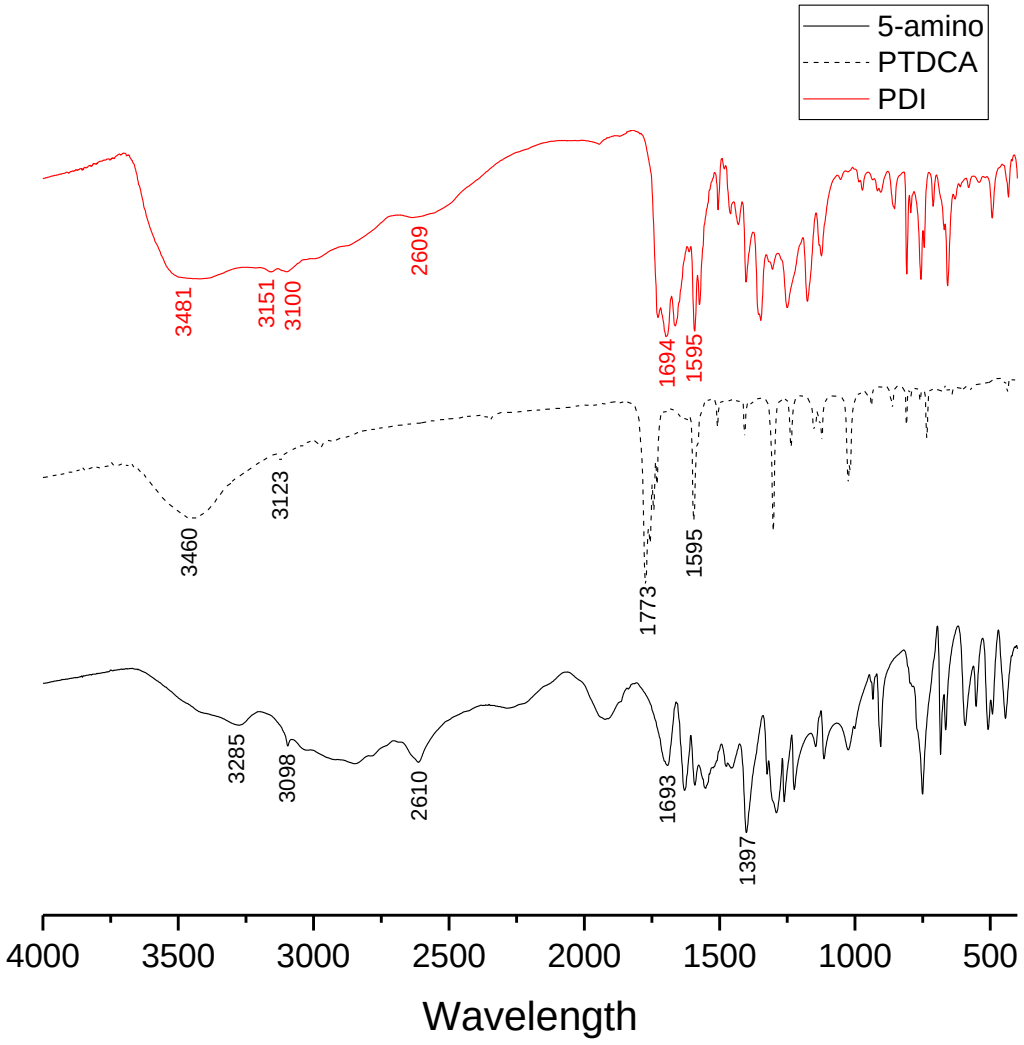

Figure 3.3 FTIR spectra of starting materials, PTCDA, 5-aminoisophthalic acid, and their product PDI. Intensities have been normalised and offset for comparison.

FTIR was used to determine the presence of functional groups attached to the perylene core by cross-referencing spectral data with starting reaction materials. As shown in **Figure 3.3**, broad peaks between 3500 – 3100 cm^{-1} are indicative of O-H bond stretches found in both PDI and 5-aminoisophthalic acid, though the presence of a strong peak around 3470 cm^{-1} within the PTCDA and PDI spectra indicates that the samples are wet. While the reaction was performed under inert gas conditions, it does not appear that the presence of water within the starting materials was detrimental to the end product.

Signals presenting around 3100 cm^{-1} in all three spectra were attributed to C-H bond stretching in an unsaturated molecule, and were confirmed by the presence of peaks between 1700 - 1500 cm^{-1} which have been associated with C-C bonds found in aromatic molecules. Peak absorbances at 2610 and 2609 cm^{-1} were related to the presence of carboxylic acid O-H bond stretches found in both 5-aminoisophthalic acid and PDI respectively. While the strong peak at 1773 cm^{-1} within the spectra for PTCDA was assigned to the C=O bond stretch found in anhydride functional groups and is appropriately not present in the spectra for either PDI or 5-aminoisophthalic acid.

Table 3.2 CHN elemental analysis results for PDI synthesis reaction from starting materials.

Sample	**% Carbon**		**% Nitrogen**		**% Hydrogen**	
	Calc.	Analysis	Calc.	Analysis	Calc.	Analysis
PTCDA	73.41	**66.28 ± 0.871**	0.00	**0.00 ± 0.00**	2.04	**1.92 ± 0.005**
5-aminoisophthalic acid	52.99	**51.57 ± 0.913**	8.28	**11.74 ± 0.512**	3.86	**4.27 ± 0.0003**
Imidazole	52.88	**53.79 ± 0.163**	44.07	**49.04 ± 1.13**	5.88	**5.99 ± 0.005**
PDI	66.67	**61.96 ± 1.23**	4.17	**5.00 ± 0.026**	2.50	**2.92 ± 0.030**

CHN elemental analysis was used to confirm the substitution had taken place. PTCDA has an elemental formula of $C_{24}H_8O_6$ giving the C, N, and H percentages calculated in **Table 3.2** from a total molecular mass of 392.32 $g.mol^{-1}$. 5-aminoisophthalic acid has an elemental formula, $C_8H_7NO_4$, with molecular mass 181.15 $g.mol^{-1}$. Imidazole, with an elemental formula $C_3H_4N_2$ has molecular mass 68.08 $g.mol^{-1}$. PTCDA, 5-aminoisophthalic acid, and imidazole mass values were provided by Sigma-Aldrich upon purchase. Mass of synthesised PDI was calculated to be 720 $g.mol^{-1}$ with an elemental formula, $C_{40}H_{18}N_2O_{12}$.

Table 3.2 shows CHN elemental analysis results conducted on starting materials and reaction products used, as mentioned, without any further purification. Values attained for PDI from the reaction match with the calculated values reasonably well with a maximum

deviation of 7.09% from the calculated carbon value. This was attributed to incomplete combustion within the chamber since the average total combustion was 69.89%. Errors in analytical values were calculated using half the difference between largest and smallest values from two separate measurements.

3.4.2 Self-Assembly

Due to its planar nature, perylene readily forms aggregates and is difficult to dissolve in conventional laboratory solvents, e.g. water, ethanol, toluene, acetone, etc. As mentioned previously (Chapter 1, section 1.1) N-substitution is commonly used to change the solubility of perylene derivatives. In the case of our PDI molecule, 5-aminoisophthalic acid contains two carboxylic acid groups, and a symmetrical substitution allowed aqueous alkaline solutions to be employed to aid dissolution.

Since we added carboxylic acid groups on bulkier aromatic functional groups, we were able to achieve self-assembly through two methods; a pH change, and solvent-diffusion in which a poor solvent is introduced to the pre-dissolved PDI and left to diffuse through.

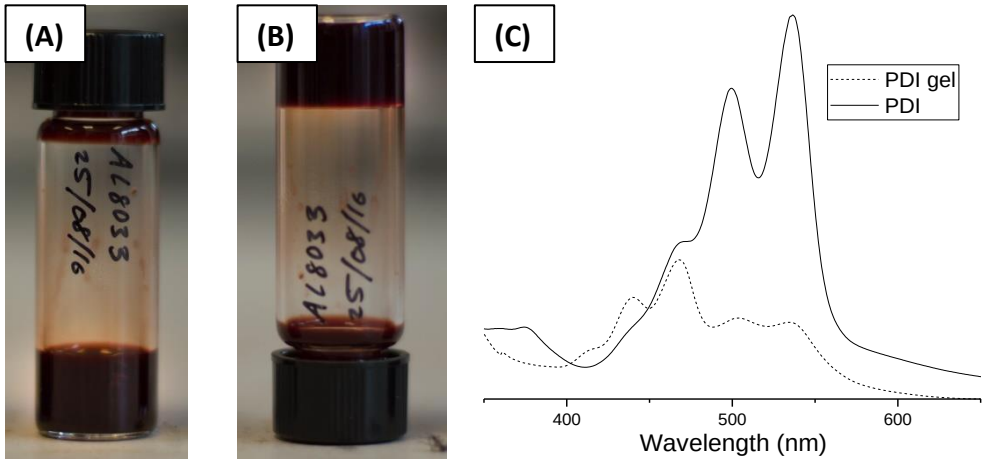

Figure 3.4 Photographic images **(A)** and **(B)** of sample **SP.3.2** after self assembly demonstrating gel formation by sample inversion. **(C)** shows recorded UV-Visible spectra of sample before and after self-assembly.

UV-Visible spectra of PDI in solution and in suspension after self-assembly were recorded using sodium hydroxide as the alkali present to aid solubility owing to the potential for imidazole to also absorb within the UV-visible light spectrum.[35] Initially, prominent peaks were measured at 536 and 499 nm with additional absorbances present at 469 and 440 nm. With a change in pH, from pH 11 – pH 6, initiated by addition of a solution of glucono-δ-lactone (GdL) in water, the position of fluorescent peaks moved.

The presence of carboxylic acid-containing R-groups that were N-substituted onto the initial PTCDA molecule, affected the solubility such that alkali could be used to dissolve PDI in aqueous solutions. Initially, NaOH was selected as a suitable alkali owing to its high solubility in water as well as its low dissociation constant, potentially allowing lower concentrations to be used. Through increasing additions of NaOH solution to a PDI mixture, it was discovered that 6 molar equivalents of NaOH must be added to PDI to ensure dissolution. Due to very strong colouring of PDI, it was necessary to add more NaOH with mixing then leave the mixture to stand for at least 30 minutes to determine if there was any solid material still present.

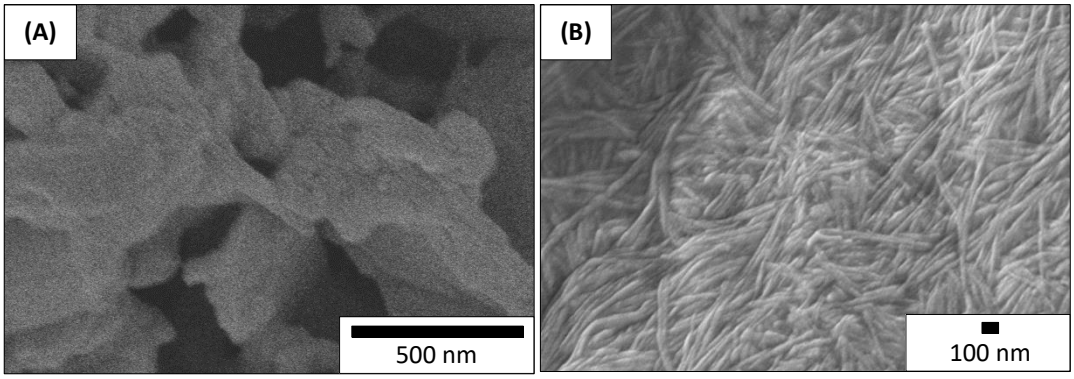

Figure 3.5 SEM images of PDI self-assembled by pH-triggering using NaOH with **(A)** H_3PO_4 (**SP.3.1**) and **(B)** GdL (**SP.3.2**). Images taken after lyophilisation.

The interactions between acids and bases are greatly influenced by how strong or weak an acid or base is and its counterpart. A strong acid with a strong base will cause a very large and rapid change in pH around the equivalence point.[36] **Figure 3.5(A)** shows PDI after using

NaOH as a solubilising agent, and H_3PO_4 as a pH trigger. No fibres could be observed within the sample which was attributed to a too rapid pH change, inhibiting PDI molecules from advantageously arranging themselves into the desirable fibrous structures before precipitation occurred.

The interaction between strong bases and weak acids caused a longer time-period to pass at higher pH before a less rapid decrease in pH occurs at the equivalence point.[36] **Figure 3.5(B)** shows fibres formed using GdL as a weak acid. Slower interactions than those between NaOH and H_3PO_4 appeared to allow a slower pH transition to acidic conditions, causing PDI molecules to have enough time to arrange themselves into fibres (**Table 3.1**).

Imidazole was presented as an alternative alkali material for consideration since it has the ability to act as both a base and a weak acid, it was hypothesised that imidazole, coupled with GdL, could provide a slow enough pH change when exposed to acid thereby allowing PDI more time to self-assemble, favouring the formation of fibres. Initially, a greater concentration of imidazole was used to ensure dissolution of PDI in water, owing to it being a weaker acid, 9 molar equivalents of imidazole were used for each 1 molar equivalent of PDI. **Figure 3.6(A)** shows fibres formed using this weak acid – weak base interaction using equivalent amounts of imidazole and GdL to induce self-assembly.

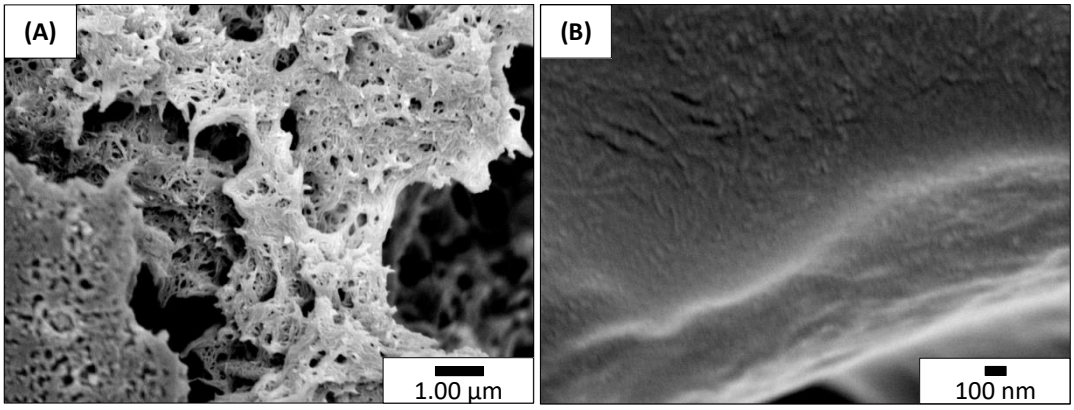

Figure 3.6 Sample **SP.3.5** PDI fibres shown **(A)** before carbonisation and **(B)** after carbonisation directly after freeze drying

Drying fibres using lyophilisation provided advantages in fibre retention and yield given that using a filtration method will invariably result in lost material in the filter and loss of any continuous super structure present in the monolith. However, as can be seen in **Figure 3.6(A)**, while fibres were initially present in the sample **Figure 3.6(B)** showed that after carbonisation, no fibrous material could be found. This was a result of a continued presence of the alkaline solubilising agent, imidazole, which has a melting point between 89-91°C, while GdL decomposes at 151-155°C.[37,38] The presence of molten imidazole within the crucible caused dissolution of the PDI fibres and their structural collapse. As such, it was determined that washing the fibres to isolate them using ethanol was the preferred method of extraction.

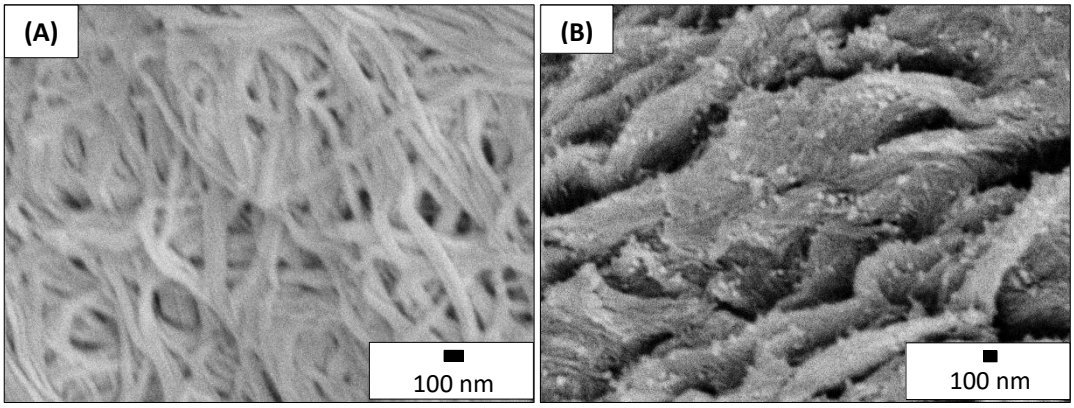

Figure 3.7 SEM images of **SP.3.6 (A)** before carbonisation and **(B)** after carbonisation**.**

It was discovered that a lower concentration of imidazole could be used to dissolve PDI within the same volume of water. 4 molar equivalents of imidazole to 1 molar equivalent of PDI was sufficient to ensure there was no precipitate in the solution. Using these ratios for the starting solutions also enabled a slight excess of GdL to be used to switch the pH. The ratio of acid to base used was 1.2 : 1 molar equivalents as stated in **Table 3.1**.

PDI fibres which were isolated from their suspension in aqueous solution through filtration and washing with ethanol to remove imidazole without destroying structure could be carbonized and **Figure 3.7** shows retention of fibres within the material. On average, fibres

were 14.39% smaller in diameter after carbonization which could be loosely related to the loss of carbonyl groups from the initial PDI molecule since it is believed that PDI-stacking may be in the formation of helices which can be influenced by the addition of chiral N-substitutions.[3,13] Similarly, carbonization yielded 57.63% of the total material used, mass losses were also attributed to the decomposition at imide side-groups.

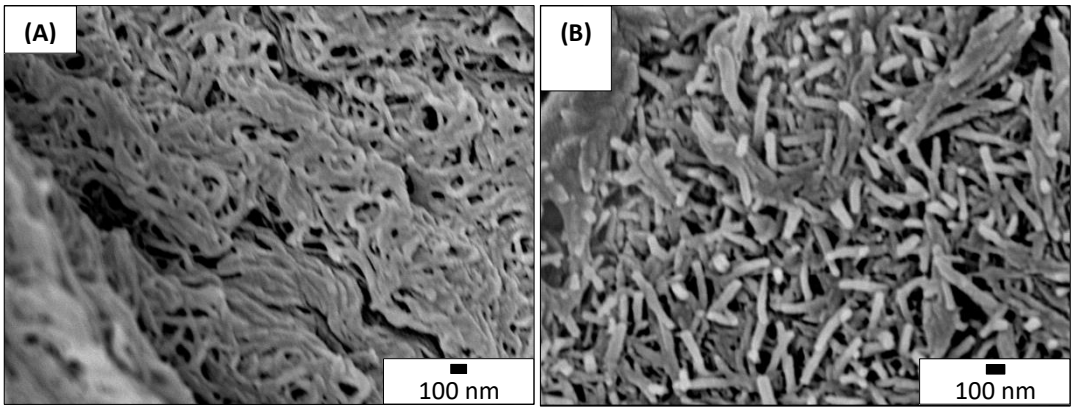

Figure 3.8 SEM images of **SP.3.7 (A)** before carbonisation and **(B)** after carbonisation.

A combination of iron (III) nitrate in water with GdL added to PDI solution with imidazole resulted in entangled fibre formation, while post self-assembly washing with ethanol ensured removal of any remaining imidazole in the mixture. Thus, fibres were retained after carbonisation and could be observed under SEM. Widths of the measured fibres increased after carbonisation which was speculated to be due to fibre stacks fusing during heating combined with an overall mass loss which could be related to the N-substituted groups on the original PDI molecule. It was not possible to perform energy-dispersive x-ray spectroscopy on the samples within the SEM to determine if any iron material remained after washing and carbonisation.

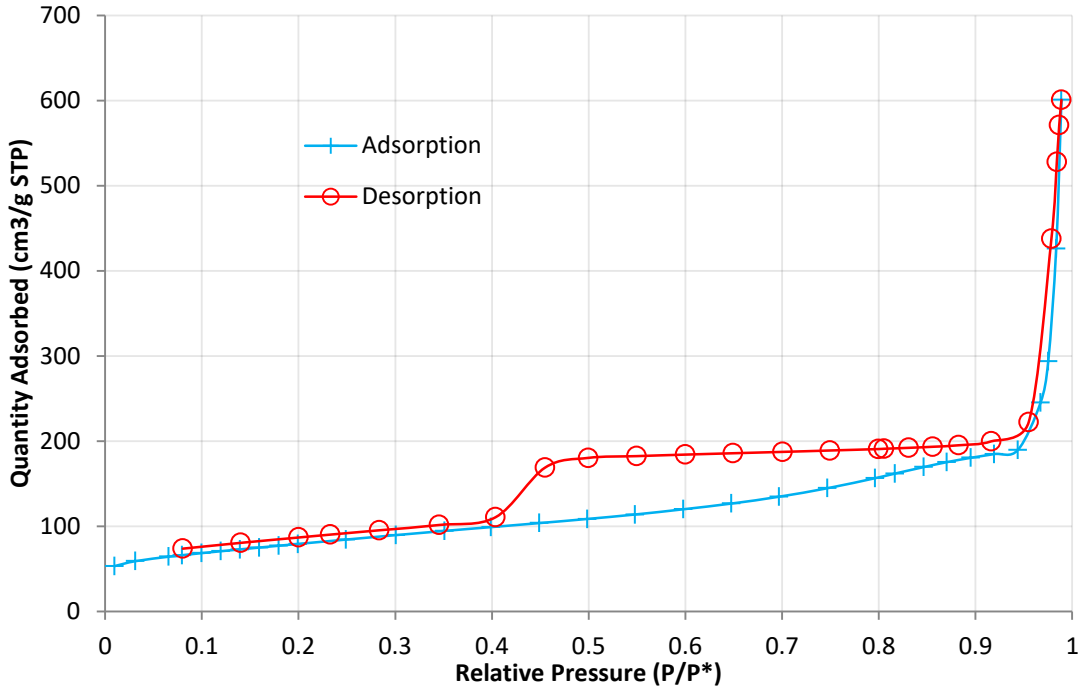

Figure 3.9 N_2 BET isotherm of **SP.3.7**.

BET analysis of sample **SP.3.7** after carbonisation revealed a surface area of 242 $m^2.g^{-1}$ without any post-synthetic modification. The isotherm generated by sample **SP.3.7** shows a type II isotherm which initially indicates a non-porous material, though there is a distinct type H2 hysteresis loop which has been associated with more complex pore structures. The steep desorption branch was a result of pore blocking, pores with wider and narrow sections, or interconnected channels. BJH adsorption pore radii generated a range of pores between 1-6 nm which, with the self-assembly process, it was thought that fibres could be formed in an entangled state which could appear as interconnected channels to an analytical technique.

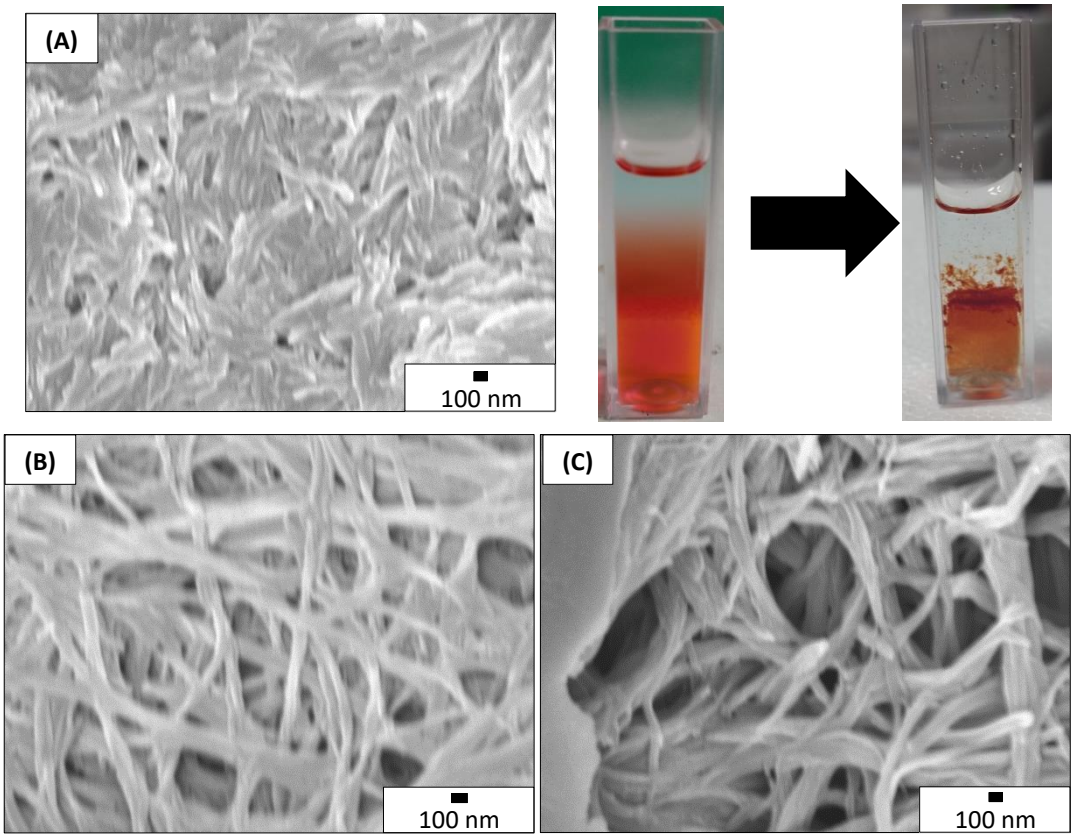

Figure 3.10 SEM images of fibres formed with interfacial self-assembly of PDI using **(A) SP.3.8** ethanol **(B) SP.3.9** $Fe(NO_3)_3$/ethanol **(C) SP.3.10** $Cu(NO_3)_2$/ethanol with photos of **SP.3.10** with copper solution before and after interfacial assembly.

Figure 3.10 shows SEM images of fibres formed using interfacial self-assembly between the original PDI solution, using imidazole as a solubilising agent, and ethanol solutions. As stated in **Table 3.1**, there is variation in fibre diameters between fibres formed using purely pH-triggered self-assembly and those formed at the interface between aqueous PDI solution and the poor solvent ethanol either neat or containing acidic metal ion species.

It was speculated that since imidazole is also soluble in ethanol, that the presence of ethanol alone was not enough to overcome its solubilising ability. However, with the additional presence of Lewis acidic metal ions within the ethanol solution, pH-triggering and interfacial self-assembly methods combined to form entangled fibres.

3.4.3 Electrospinning

Attempts to spin neat, aqueous PDI solutions resulted in randomized jetting since intermolecular forces between PDI molecules was not strong enough to balance the external potential applied to the solution. As a result, the solution was ejected in a manner similar to that of electrospraying, and since there was no balance of surface tension vs applied potential, the solvent, water, did not evaporate. Liquid material arrived at the collector without any change in supramolecular structure.

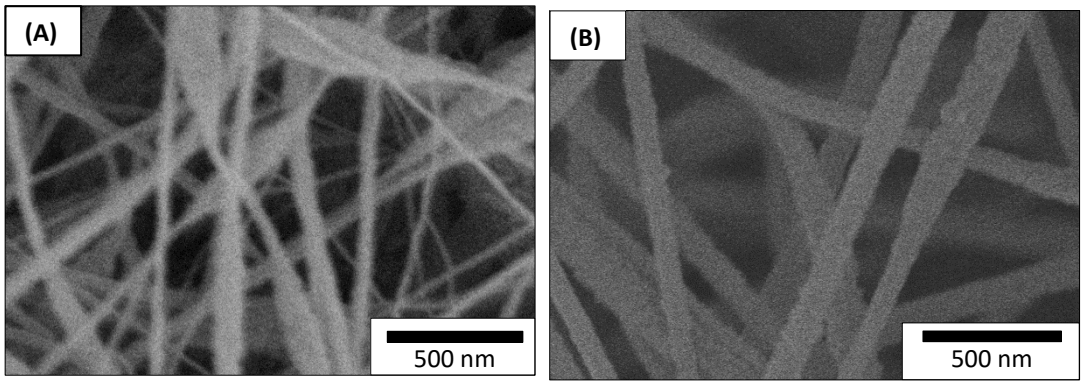

Figure 3.11 SEM images of electrospun polymer samples (**A**) **PAN 1**, (**B**) **PAN 3**

Due to its prominence as a good electrospinning carrier polymer, **Figure 3.11 (A)** shows fibres achieved initially using PAN with a molecular weight 150 000 g mol^{-1} dissolved in DMSO. The fibres in **Figure 3.11(A)** had some beaded sections and were not uniformly spun, while **Figure 3.11 (B)** shows PAN in DMF with small quantities of PDI present in the initial spinning solution, the addition of PDI appeared to have lessened the surface tension of PAN in DMF enough such that more uniform fibres were formed. However solubility restrictions for PDI necessitated use of alkaline additives to aid dissolution of PDI within the solution and only very small concentrations were able to be dissolved. Poly (vinyl alcohol) (PVA) was considered as another carrier polymer, however this was undesirable since PVA itself can be carbonised after electrospinning into carbon nanofibres. PEG with molecular weight

400 000 g mol^{-1}, can be electrospun from alkaline aqueous solutions and as such was employed as a carrier polymer for PDI.

A desirable characteristic of PEG is that when carbonised in an inert atmosphere, it will be completely decomposed[39] (**Appendix A.2**). Aqueous solutions of PEG were made up in concentrations as stated in **Table 3.3** without additional PDI present, and spun to produce fibres which were then heated to 800°C in a nitrogen atmosphere. Using this thermogravimmetric analysis, carbonisation conditions were mimicked.

Table 3.3 Electrospun PDI (**EP**) sample starting solutions, fibre diameters, and their carbonisation yields.

Sample	Concentration			Conditions	Diameter/nm		% Yield
	Polymer	PDI	Solvent		Bef.	Aft.	
PAN 1	PAN (4 wt.%)	N/A	DMF	22 kV 1 mL.h^{-1}	76	59	27.27%
PAN 2	PAN (10 wt.%)	N/A	DMF	22 kV 1 mL.h^{-1}	558	452	43.07%
PAN 3	PAN (4 wt.%)	10 mM	DMF/ TEA (0.12 M)	22 kV 1 mL.h^{-1}	112	398	22.65%
PVA	PVA (10 wt.%)	N/A	Water	25 kV 0.8 mL.h^{-1}	231	N/A	N/A
PEG	PEG (7.5 wt.%)	N/A	Water	13.0 kV 0.50 mL.h^{-1}	136	N/A	0.00%
PEG 2	PEG (7.5 wt.%)	N/A	Water/ imidazole (0.24 M)	10.0 kV 0.24 mL.h^{-1}	88	N/A	0.00%
EP.3.1	PEG (4 wt.%)	60 mM	Water/ imidazole (0.24 M)	9.3 kV 0.38 mL.h^{-1}	71	40	24.08%
EP.3.2	PEG (3 wt.%)	60 mM	Water/ imidazole (0.24 M)	8.0 kV 0.15 mL.h^{-1}	120	74	23.39%
EP.3.3	PEG (5 wt.%)	60 mM	Water/ imidazole (0.24 M)	10.5 kV 0.24 mL.h^{-1}	189	75	16.78%
EP.3.4	PEG (5 wt.%)	90 mM	Water/ imidazole (0.36 M)	10.0 kV 0.25 mL.h^{-1}	192	54	23.05%
EP.3.5	PEG (3 wt.%)	70 mM	Water/ imidazole (0.28 M)	10.0 kV 0.1 mL.h^{-1}	511	54	16.63%
EP.3.6	PEG (2 wt.%)	46.7 mM	Water/ imidazole (0.16 M)	9.5 kV 1.0 mL.h^{-1}	N/A	17	28.96%
EP.3.7	PEG (1.6 wt.%)	46.7 mM	Water/ imidazole (0.16 M)	15 kV 1.0 mL/h^{-1}	N/A	21	30.69%

Fibres were then produced from PEG/PDI solutions as described in **Table 3.3**. Samples **EP.3.1**-**EP.3.5** consisted of attempting to optimise solution properties to achieve fibres with

minimal beading or other evidence of an unstable electrospinning jet while simultaneously trying to use fewer additional materials during solution processing. This was to reduce overall environmental impact. As PEG was chosen specifically for its lack of residue after carbonisation, fibre diameters were measured before and after carbonisation.

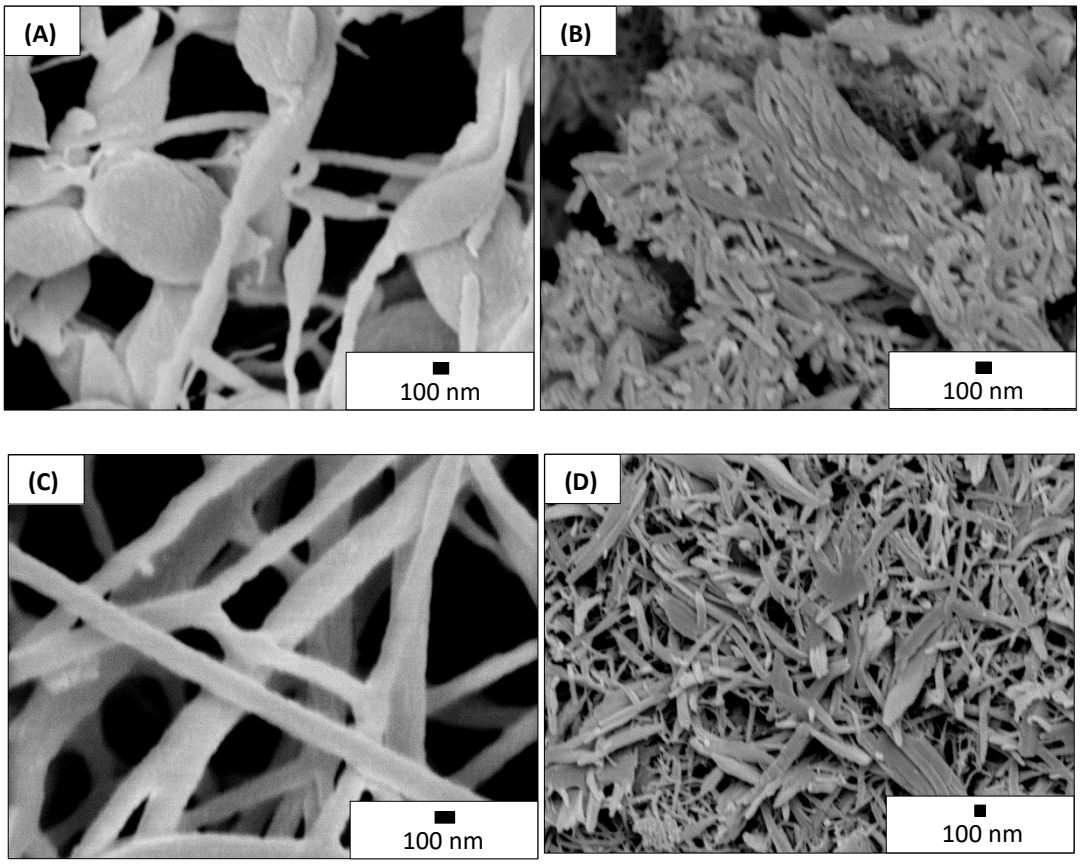

Figure 3.12 SEM images of samples **EP.3.2** and **EP.3.3** after electrospinning, **(A)** and **(C)**, and after carbonisation, **(B)** and **(D)** respectively.

In **Figure 3.12(A)**, electrospun material formed using sample **EP.3.2** resulted in a non-uniform structure which contained a majority of beading effects rather than fibres. This was due to a deficit in the proportion of PEG within the starting solution, preventing the jet from balancing the potential and surface tension forces acting upon the solution. Rather than emerging from the syringe as a continuous stream, there was a spraying effect. After carbonisation, **Figure 3.12(B)** appeared to show fibrous materials despite their lack of presence prior to carbonisation. This implied that PDI must, at some point during flight,

self-assemble into fibres. It was speculated that the electrospinning process provides an environment akin to evaporation-triggered self-assembly since the PEG provides enough surface tension for the PDI solution to withstand the whipping instability which occurs during flight and assists in solvent evaporation. Once the solvent has evaporated, the remaining PDI can self-assemble into fibrous structures which are contained within a PEG matrix and can be revealed once PEG has been removed through carbonisation.

By increasing the concentration of PEG in sample **EP.3.3**, **Figure 3.12(C)** shows that more uniform fibres arrive at the collector. The fibres under SEM appeared to show a branched morphology which indicates a still unstable jet resulting in lower local charge per unit surface area causing a smaller jet to be ejected from the surface or for the primary jet to split into two smaller jets. Such branching usually occurs at 90° to the axis of the primary jet, which is consistent with our findings.[40]

After carbonisation, there was minimal uniform fibre retention visible from **Figure 3.12(D)**. The remaining material is of comparable width as the fibres of sample **EP.3.2** which remained after carbonisation, though with much lower uniformity. This suggests that a similar self-assembly phenomenon occurs in-flight. However, since the fibres produced by electrospinning arrive at the collector as a non-entangled mat, it is possible that carbonisation results in a mixture of PDI fibre morphologies. After carbonisation, PDI fibres are either as formed within the PEG mixture after electrospinning, or, as a result of proximity to other fibres prior to carbonisation, fused fibres as was suggested previously occurred with the self-assembled fibres, **SP.3.7**.

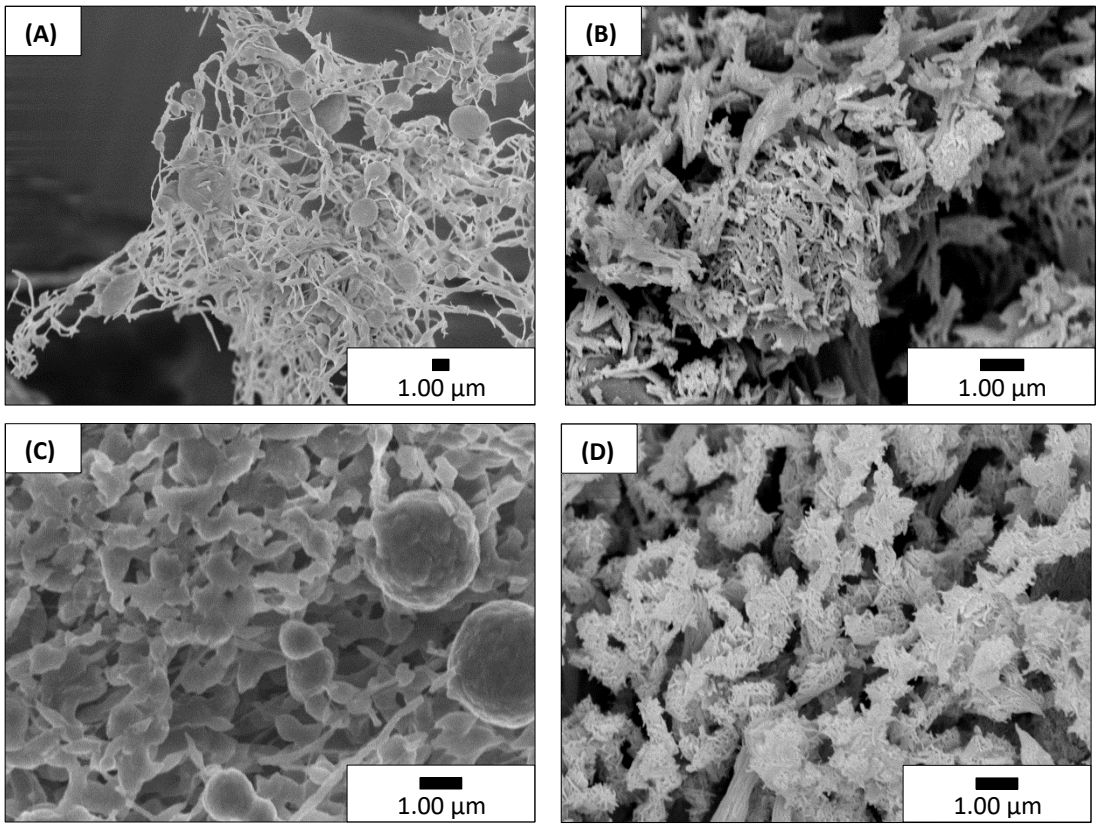

Figure 3.13 SEM images of electrospun samples **EP.3.4** and **EP.3.5**. Images **(A)** and **(C)** are of **EP.3.4** and **EP.3.5** respectively. Images **(B)** and **(D)** are of respective samples after carbonisation.

In trying to increase the ratio of PDI or active material in the initial electrospinning solution, the stability of the fluid jet was disturbed since the surface tension provided by the PEG molecules was lessened proportionally. **Figure 3.13(A)** shows a sample with many beaded sections with connecting fibres. As with sample **EP.3.2**, after carbonisation, **EP.3.4** displayed fibres. Unlike with self-assembled fibres, there was no washing necessary after electrospinning despite the continued presence of imidazole in the initial spinning solution. As stated in **Table 3.3**, there was no significant residue after carbonising an electrospun PEG/imidazole material which suggests that both materials were removed during carbonisation in a manner which did not affect the PDI structure.

Sample **EP.3.5** increased the PDI content in order to decrease surface tension and reduce beading, however the opposite morphology resulted. Mostly beaded material reached the collector with limited, if any, connecting fibres between beads. After carbonisation however, the material retained its initial spherical morphology, though the beads were comprised of bundles of fibres. These fibres were of comparable diameter to the previous sample, **EP.3.4**, 54 nm. These fibres, in turn, were of comparable diameter and surface area to those formed through self-assembly methods, **EP.3.4** = 285 $m^2.g^{-1}$ and **EP.3.5** = 183 $m^2.g^{-1}$.

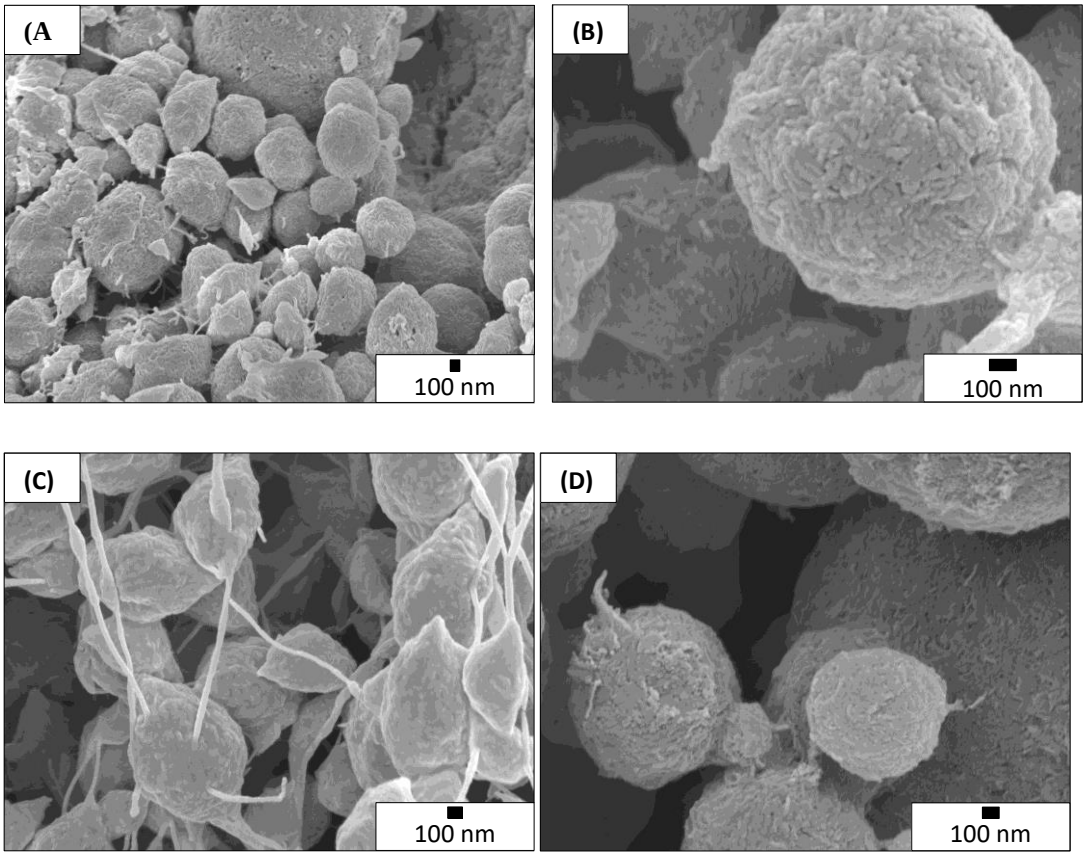

Figure 3.14 Electrosprayed spheres of PEG/PDI mixtures. **(A)** is sample **EP.3.6 (C)** is sample **EP.3.7**. **(B)** and **(D)** show respective samples after carbonisation

Finally, as PDI fibres were unaffected by the initial morphology of the electrospun PEG/PDI mixture, it was thought that producing uniformly distributed spheres in a process more akin to electrospraying could be beneficial. The solution mixture parameters were altered to

change the balance between applied potential and surface tension. As expected, these parameters resulted in a larger proportion of spheres than connecting fibres and after carbonisation, spheres composed of bundles of fibres could be observed. **EP.3.6** CNFs in **Figure 3.14(B)** showed a value of 412 $m^2.g^{-1}$ after surface area analysis with pore radii of 7.24 nm which, as was found with self-assembled fibres, could be due to entanglement which occurred due to self-assembly within a package of PEG spheres.

Figure 3.14(C) shows sample **EP.3.7** collected after electrospraying. With a lower concentration of PEG present in the initial spinning solution but a higher spinning potential, the beads formed were less spherical in shape with more connecting fibres which suggested that the potential overcame more of the surface tension provided by the PEG in flight, allowing elongation. Though after carbonisation the connecting fibres are no longer visible and similar fibre-containing spheres could be observed. BET analysis of sample **EP.3.7** after carbonisation revealed a slightly lower surface area than that of sample **EP.3.6** though with similar values calculated for pore radii and volume it is reasonable to suggest that the materials formed are not too dissimilar from each other. This implies that the solution parameters are relatively robust and can be altered without significant detrimental effect to the final product.

3.6 Conclusions

Previous research within the group provided an imide-substituted PDI molecule capable of self-assembly though the method provided proved difficult to replicate. Self-assembly triggered through pH-change was optimised to utilise a weak-base/weak-acid interaction. The slower pH transition facilitated formation of more ordered fibres, coupled with a washing procedure, which were successfully carbonised yielding nanofibres. Solvent-interfacial self-assembly was also explored utilising additional metal ions, though due to equipment restraints, residual presence of metal ions after self-assembly was not able to be ascertained. Detecting whether PDI self-assembly can integrate metals within the fibres would be worth exploring in order to incorporate functionlisation.

By incorporating PDI into an electrospinning process, it was thought that non-woven fibrous mats could be produced and provide another route to PDI fibre production. As PDI could not itself sustain jet stability, PEG was incorporated as a carrier polymer which could be removed after carbonisation. It was discovered that PDI could self-assemble in-flight since the beading effect, caused by imbalance between surface tension and potential, after carbonisation contained PDI fibres. Fibres retained their morphology without an extra washing step despite the presence of imidazole as a solubiliser in the initial spinning solution.

Overall, PDI fibres were produced through two different methods. Self-assembled gels provide potential to construct discrete monoliths with good yields and surface areas after carbonisation. pH-triggering of gelation could be tuned to incorporate metal ions or other active species, and further research into PDI's ability to retain such active species is desirable. Electrospun materials provides a continuous production method and potentially a method of coating surfaces in bundles of PDI fibres with accessible internal surfaces.

Electrospinning also provided a facile route to PDI fibres which is not inhibited by time-consuming washing steps to remove extra compounds used in initial production.

3.7 References

1 K. Sun, C. Xiao, C. Liu, W. Fu, Z. Wang and Z. Li, *Langmuir*, 2014, **30**, 11040–11045.

2 K. Wang, W. Zhang, R. Phelan, M. A. Morris and J. D. Holmes, *Journal of the American Chemical Society*, 2007, **129**, 13388–13389.

3 Q. Song, F. Li, Z. Wang and X. Zhang, *Chemical Science*, 2015, **6**, 3342–3346.

4 M. R. Wasielewski, *The Journal of Organic Chemistry*, 2006, **71**, 5051–5066.

5 P. Serp, M. Corrias and P. Kalck, *Applied Catalysis A: General*, 2003, 253, 337–358.

6 C. M. Lieber, *MRS Bulletin*, 2011, 36, 1052–1063.

7 S. Sainio, H. Jiang, M. A. Caro, J. Koehne, O. Lopez-Acevedo, J. Koskinen, M. Meyyappan and T. Laurila, *Carbon*, 2016, **98**, 343–351.

8 S. Peng, L. Li, J. Kong Yoong Lee, L. Tian, M. Srinivasan, S. Adams and S. Ramakrishna, *Nano Energy*, 2016, 22, 361–395.

9 H. Langhals, S. Demmig and H. Huber, *Spectrochimica Acta Part A: Molecular Spectroscopy*, 1988, **44**, 1189–1193.

10 H. Langhals, *HETEROCYCLES*, 1995, **40**, 477.

11 S. Chen, P. Slattum, C. Wang and L. Zang, *Chemical Reviews*, 2015, **115**, 11967–11998.

12 F. Würthner, *Chemical Communications*, 2004, **14**, 1564–1579.

13 K. Sun, C. Xiao, C. Liu, W. Fu, Z. Wang and Z. Li, *Langmuir*, 2014, **30**, 11040–11045.

14 W. Herbst, K. Hunger, G. Wilker, H. Ohleier and R. Winter, *Industrial Organic Pigments*, Wiley, 3rd Ed., 2004.

15 M. Greene, in *High Performance Pigments*, Wiley-VCH Verlag GmbH & Co. KGaA, Weinheim, Germany, 2009, pp. 261–274.

16 N. I. Georgiev, A. R. Sakr and V. B. Bojinov, *Dyes and Pigments*, 2011, **91**, 332–339.

17 C. Huang, S. Barlow and S. R. Marder, *The Journal of Organic Chemistry*, 2011, **76**, 2386–2407.

18 F. Criscitiello, A. Scigliano, R. Bianco, M. R. Beccia, T. Biver and A. Pucci, *Colloids and Surfaces A: Physicochemical and Engineering Aspects*, 2017, **516**, 32–38.

19 G. Boobalan, P. K. M. M. Imran and S. Nagarajan, *Spectrochimica Acta - Part A: Molecular and Biomolecular Spectroscopy*, 2013, **113**, 340–345.

20 G. Boobalan, P. M. Imran, S. G. Ramkumar and S. Nagarajan, *Journal of Luminescence*, 2014, **146**, 387–393.

21 R. Khajavi and M. Abbasipour, *Scientia Iranica*, 2012, **19**, 2029–2034.

22 B.-S. Lee, H.-S. Yang and W.-R. Yu, *Nanotechnology*, 2014, **25**, 465602.

23 R. Mishra, J. Militky and M. Venkataraman, in *Nanotechnology in Textiles*, Elsevier, 2019, pp. 35–161.

24 D. H. Reneker and A. L. Yarin, *Polymer*, 2008, **49**, 2387–2425.

25 T. Subbiah, G. S. Bhat, R. W. Tock, S. Parameswaran and S. S. Ramkumar, *Journal of Applied Polymer Science*, 2005, **96**, 557–569.

26 G. Taylor, *Proceedings of the Royal Society A: Mathematical, Physical and Engineering Sciences*, 1969, **313**, 453–475.

27 A. Das, J. Adhikari and P. Saha, in *Nanocarbon and its Composites: Preparation, Properties and Applications*, Elsevier, 2018, pp. 91–122.

28 D. Giuri, M. Barbalinardo, G. Sotgiu, R. Zamboni, M. Nocchetti, A. Donnadio, F. Corticelli, F. Valle, C. G. M. Gennari, F. Selmin, T. Posati and A. Aluigi, *Nanoscale*, 2019, **11**, 6422–6430.

29 M. A. Cerqueira, S. Torres-Giner and J. M. Lagaron, in *Nanomaterials for Food Packaging: Materials, Processing Technologies, and Safety Issues*, Elsevier, 2018, pp. 147–171.

30 S. Torres-Giner, in *Multifunctional and Nanoreinforced Polymers for Food Packaging*, Elsevier, 2011, pp. 108–125.

31 X. Liu, A. Ahmed, Z. Wang and H. Zhang, *Chemical Communications*, 2015, **51**, 16864–16867.

32 X. Liu, A. Roberts, A. Ahmed, Z. Wang, X. Li and H. Zhang, *Journal of Materials Chemistry A*, 2015, **3**, 15513–15522.

33 E. R. Draper, B. J. Greeves, M. Barrow, R. Schweins, M. A. Zwijnenburg and D. J. Adams, *Chem*, 2017, **2**, 716–731.

34 E. Rostami-Tapeh-Esmail, M. Golshan, M. Salami-Kalajahi and H. Roghani-Mamaqani, *Dyes and Pigments*, 2020, **180**, 108488.

35 'Photoelectric Spectrometry Group England Staff', in *UV Atlas of Organic Compounds / UV Atlas organischer Verbindungen*, Springer US, Boston, MA, 1967, pp. 5–605.

36 R. de Levie, *Journal of Chemical Education*, 1993, **70**, 209.

37 Imidazole | C3H4N2 - PubChem, https://pubchem.ncbi.nlm.nih.gov/compound/Imidazole, (accessed 14 April 2020).

38 Gluconolactone | C6H10O6 - PubChem, https://pubchem.ncbi.nlm.nih.gov/compound/Gluconolactone#section=Melting-Point, (accessed 14 April 2020).

39 R. P. Lattimer, *Journal of Analytical and Applied Pyrolysis*, 2000, **56**, 61–78.

40 S. Koombhongse, W. Liu and D. H. Reneker, *Journal of Polymer Science Part B: Polymer Physics*, 2001, **39**, 2598–2606.

Chapter 4 Perylene Diimide for Sensing Metal Ions by UV-Vis Spectroscopy.

4.1 Introduction

An increasing population leads to a corresponding increase in demand for clean water supplies as such, being able to monitor and detect the presence and the concentration of metal ions is of paramount importance to avoid contamination or otherwise bioaccumulation of foreign materials through the food chain.[1–4] While detection using atomic absorption spectroscopy and inductively coupled plasma atomic emission spectrometry may be used to detect low concentrations, these methods require trained personnel, expensive equipment, and time-consuming procedures.

Fluorescent detection based analysis, on the other hand, is very popular since measurements can be very sensitive, providing real-time monitoring and quick responses, while also being easy to perform at a fraction of the price. Similarly, UV-Visible spectroscopy is a facile low-cost technique which requires minimal preparation of samples beforehand. Perylene diimide derivatives have been previously reported as fluorescent probes for detection of individual organic molecules,[5–8] biological compounds[9,10], pH[11,12], as well as biolabelling[13].

Planar aromatic dyes, such as perylene derivatives, have been known to be sensitive to the presence of metal ions. The fluorescence emission of PDI decreases in the presence of metal ions by provision of transfer of energy to an excited state which decays through an alternative non-radiative route.[14,15]

In this chapter, minimal metal ion detection limits of 2.5 nM for copper and iron salt compounds using an aqueous solution of the PDI molecule, as synthesised, in Chapter 3 are presented. PDI absorbance provides information on the concentration of metal ions present in solution as well as identification of the metal ion present.

4.2 Experimental

4.2.1 Chemicals and Materials

PDI synthesised according to the procedure detailed in Chapter 3, titanium (III) chloride (12 wt.%), copper (II) chloride dihydrate (reagent grade), copper (II) nitrate trihydrate (99%), iron (II) chloride tetrahydrate (98%), iron (III) chloride hexahydrate (97%), iron (III) nitrate nonahydrate (≥98%), zinc (II) nitrate hexahydrate (98%), and cobalt (II) acetate tetrahydrate (≥98%), were purchased from Sigma-Aldrich and used without further purification. Cobalt (II) gluoconate (98%) was purchased from AK Scientific and used as received. Ethanol (≥ 99.9 %) was obtained from Brenntag and used as received.

4.2.2 Materials Characterisation

Fluorescence measurements were recorded in 4 mL quartz cuvettes at 90° to the 350 nm incident light using a Shimadzu RF5301-PC. UV-Visible spectra were recorded on samples in 4 mL plastic cuvettes using a Shimadzu UV-Vis 3600.

4.2.3 Measuring sensitivity of aqueous PDI solutions to the presence of M^{n+} ions.

PDI (10 mM, 0.072 g) was dissolved in aqueous sodium hydroxide solution (0.05 M, 10 mL) then further diluted to 10 µM. For fluorescent measurements, PDI solution (2 mL) was placed into a quartz cuvette and analysed using a light source with wavelength 350 nm. For UV-Visible spectroscopy, PDI solution (2 mL) in a plastic cuvette was measured between

350 – 800 nm. Successive additions of metal salt solution were carried out using a pipette and the solution mixed using trituration. Concentrations of metals within solution were calculated using the new total volume and absorbance was measured. Comparisons between spectra were drawn from data normalised with respect to the initial absorbance value at wavelength 536 nm.

4.3 Results and Discussion

4.3.1 Standardising Sensing Solution

A response to acidic stimuli was produced in **Figure 4.1** without the presence of transition metal ions to quench the absorbance at 536 nm. A solution of PDI (6 mM) dissolved in 1.5 mL NaOH (0.036 M) was self-assembled into fibres using an aqueous solution of glucono-δ-lactone, GdL (0.043 M) in a 1:1 volume ratio. The presence of the weakly acidic GdL, in concentration greater than the solubilising agent NaOH, caused the slow adjustment of pH from ~12 to <6 within the mixture providing the trigger for the PDI to self-assemble.

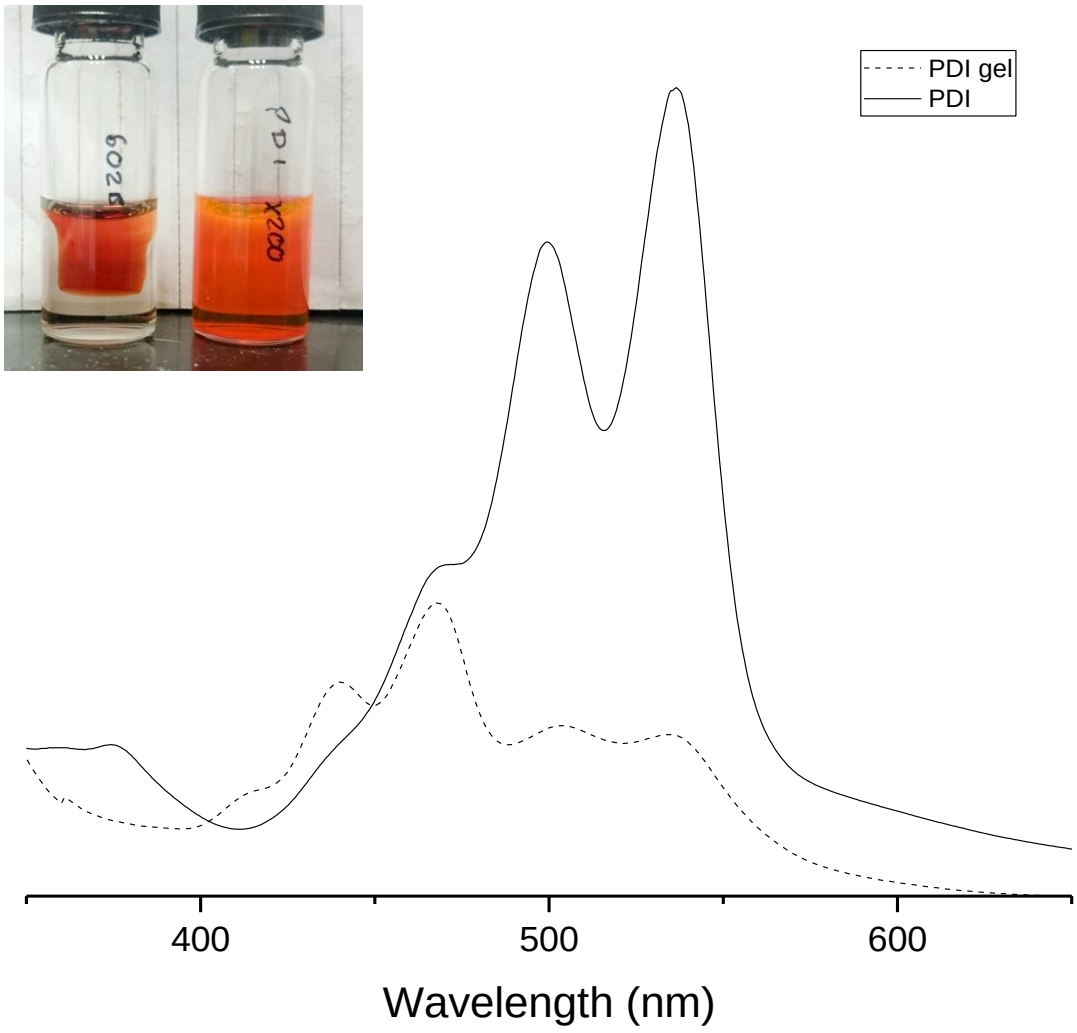

Figure 4.1 UV-Visible spectra of PDI in NaOH solution (solid) and PDI after self-assembly (dashed). Inset shows PDI (6 mM), NaOH (6 mM) aqueous solution before (right) and after (left) self-assembly.

After gelation, peaks at 534 and 499 nm absorbed less while, peaks at 469 and 440 nm increased their relative absorbance. It was speculated that the change was evidence of H-aggregates forming due to the significant decrease in the position of absorbance (blue-shift) while the shape of the spectra remains constant and the ratio between peaks is comparable.[16–18] The ratio between the initial spectra peaks at 534 and 499 nm was calculated at 0.8333, while the ratio between peaks after gelation was 0.8009. Non-aggregated PDI present in the solution indicated by peaks still present at 534 and 499 nm.[19]

Changes in the main absorbing peaks were attributed to a change in the energy gap between molecular orbital energies. As the molecules of PDI self-assemble it is speculated that the extended supramolecular structure is more stable and therefore the HOMO-LUMO gap is increased. This change in energy was attributed to the π-π interactions between molecules which occur during self-assembly. The stacking utilises interactions between delocalised π-electrons upon individual molecules which significantly lower the molecular orbital energy of the HOMO when in phase, while increasing the molecular orbital energy of the out of phase LUMO.[20]

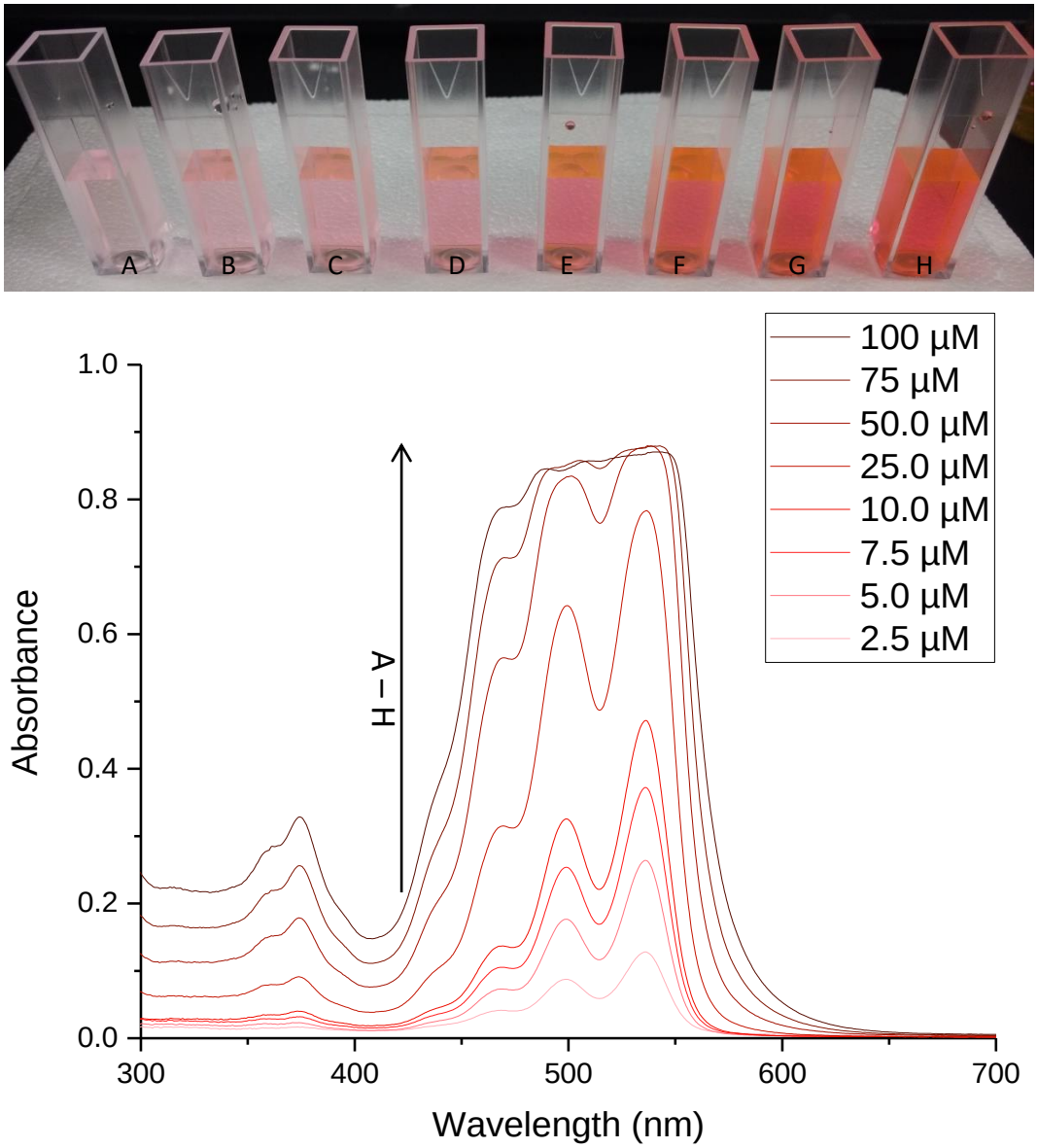

Figure 4.2 PDI solutions from A – H increasing in concentration (2.5, 5.0, 7.5, 10.0, 25.0, 50.0, 75.0, 100.0 µM) in 5 molar equivalent concentration of sodium hydroxide and corresponding UV-Visible spectra.

As mentioned previously in section **3.4.2** synthesised PDI was very sparingly soluble in neutral water due to strong π-π interactions, thus aqueous sodium hydroxide (NaOH) solution was used to adjust water to an alkaline pH (pH = 12) and deprotonate carboxylic acid groups. Clear pink-orange solutions, which can be observed in **Figure 4.2** were the result of highly dilute 10 µM PDI solutions with sodium hydroxide in water. For PDI

solutions to be utilised as sensors, a standard solution with suitable concentrations was determined using UV-Vis. This standard concentration must be low enough to allow enough transmission while being easily detectable, but high enough that the signals can be clearly measured without individual peaks becoming drowned out by overall signal.

Strong colouration of PDI molecules necessitated use of very dilute solutions to balance desirable and detectable absorption against saturation of the signal. Solutions of PDI were made up in increasing concentrations; 2.5, 5.0, 7.5, 10.0, 25.0, 50.0, 75.0, 100.0 μM, using 5 molar equivalents of sodium hydroxide for solubility in water. Spectra of samples were recorded and the concentration of 10 μM was chosen to be used as the standard since there is enough intensity in the signal to clearly identify changes and the peaks remain discrete.

4.3.2 Fluorescence

Using the solutions made up to concentrations stated in **4.3.1** quartz cuvettes were prepared with thorough washing in water, ethanol, and acetone and oven drying before use. PDI solution, 2 mL, placed in the cuvette was measured first as a reference before additions of the metal ion solutions. Mixture was achieved using trituration before the next measurement was recorded.

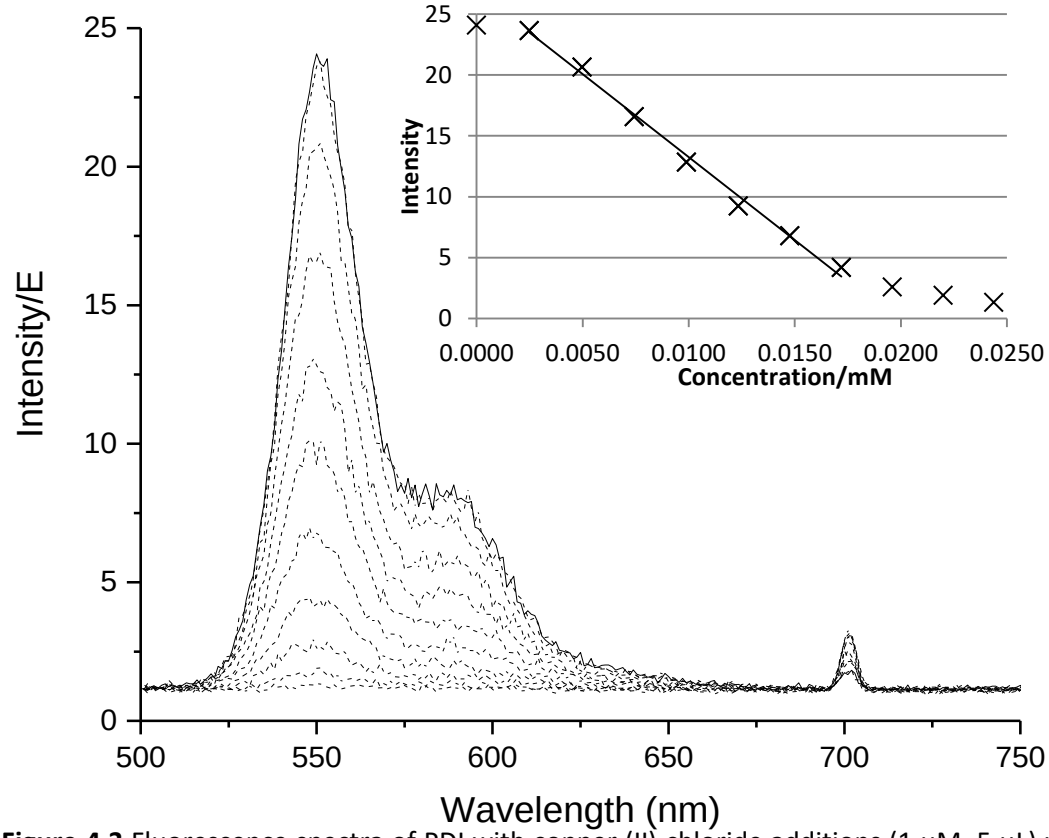

Figure 4.3 Fluorescence spectra of PDI with copper (II) chloride additions (1 µM, 5 µL) with a graph of λ_{550} emission intensity vs concentration (inset).

Initial measurements showed the highest intensity peak between 549-551 nm and a shoulder peak between 577-592 nm. Longer emission wavelengths compared to absorbance wavelengths are consistent with the Stokes shifts of fluorophores and vibrational relaxation.

Using measurements taken at λ_{max}, 550 nm, changes in the emission spectra upon addition of copper (II) chloride were monitored. **Figure 4.3** depicts the rapid decrease in emission intensity with successive additions of copper chloride solution. A linear trend between emission units (E) and additions of 5 to 35 µL of solution was isolated with a relationship of Intensity = -1361.12 E.μM^{-1} [Cu^{2+}] + 26.86 E, with a spread of 0.60%. After addition of 50 µL of copper solution, fluorescence emission was no longer detectable.

Fluorescence emission spectra are usually detected with intensity measured in the hundreds (arbitrary units),[21–23] whereas this PDI solution presented intensity an order of magnitude less. Due to this low intensity, the peak maxima were difficult to isolate consistently due to variation, or noise, within the signal and thus a larger error. As such, it was decided that UV-Vis would be the most beneficial technique moving forwards.

4.3.3 UV-Vis

UV-Visible spectroscopy was primarily used for observations since signal-to-noise ratios were lower than those found in fluorescent spectra. 2 mL PDI solution was placed in plastic cuvettes and scanned between 350 – 800 nm, using UV-Vis to quantify changes in the spectra with additions of metal salts in very low concentrations. Initial PDI spectra showed peaks at 536, 499, and 469 nm and were normalised relative to the highest, 536 nm absorbance peak.

Previous reports of perylene diimide derivatives have shown that the presence of metal ions within the solution quench the fluorescent behaviour by providing alternative, non-radiative electronic interactions.[24,25] This mechanism was exploited for our sensing purposes, and allowed detection of materials in the range of tens of nanomolar within the 2 mL experimental conditions.

4.3.3.1 Copper

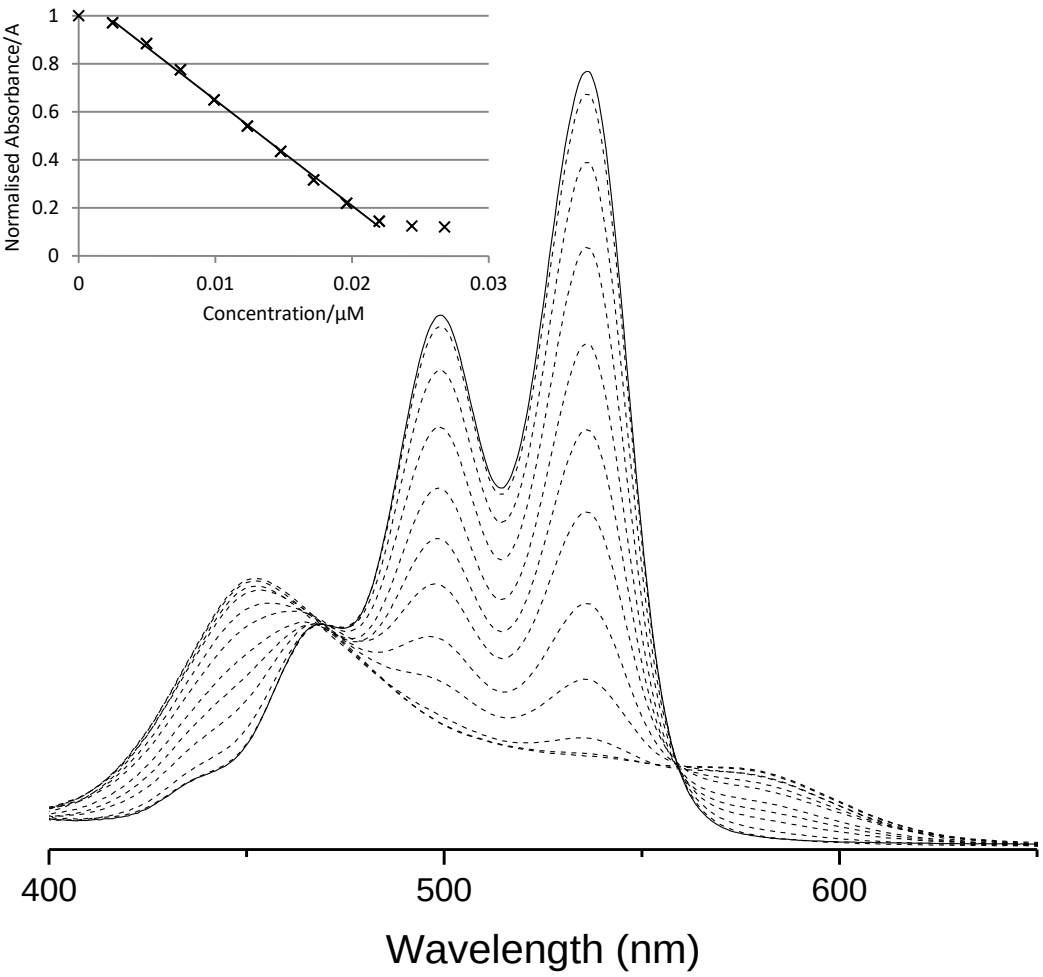

Figure 4.4 UV-Vis spectra of PDI solution with additions of copper (II) chloride (1 µM, 5 µL) with the plot of normalised absorbance λ_{536} vs concentration (inset).

As with the previous fluorescence experiment, the metal ion solution used was copper chloride in water. With 5 µL increment additions of 1 µM solution, the relationship between normalised absorbance and concentration was -44.0 A.μM^{-1}. The initial addition of copper chloride solution gave a small response, implying the lowest limit of metal ion concentration is 2.5 nM. With the intention to detect specific concentrations, there was an identifiable linear relationship between concentration and absorbance response between 2.5 nM and 22 nM. After addition of $CuCl_2$ in total concentration 22 nM, peaks at 536, and 499 nm had become indistinguishable from each other.

With each successive addition of $CuCl_2$ solution, an additional peak becomes more prominent until it could be clearly identified at 452 nm. This peak was not linearly related to the concentration added.

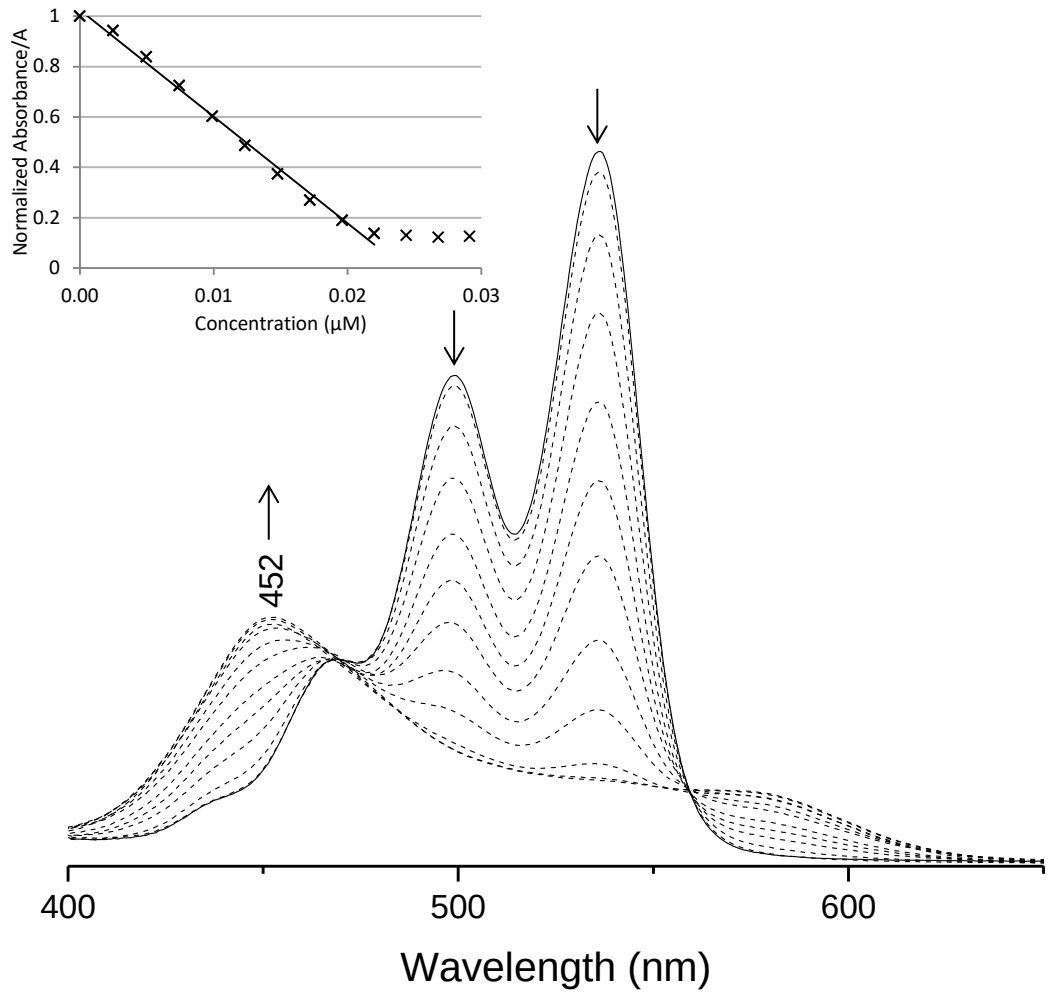

Figure 4.5 UV-Vis spectra of PDI solution with successive additions of copper (II) nitrate (1 µM, 5 µL) with plot of λ_{536} absorbance vs concentration (inset).

To test whether the anion in the salt caused any discrepancy in the results, $Cu(NO_3)_2$ was also used as the metal ion solution. **Figure 4.5** shows a comparable linear relationship could be drawn between the PDI response for $CuCl_2$ and $Cu(NO_3)_2$ with a gradient of -45.2 $A.\mu M^{-1}$. The initial delay in response was less than that observed in **Figure 4.4**. This suggests that there is a small change in response between the two associated anions which could be attributed to ion dissociation. An average plot between both copper compounds (**Appendix**

Figure A.4) provided a gradient of -45.2 A.µM^{-1} with a spread from the linear trend line of 4.45%. This spread from the linear trend limits precision in the concentration analysis to ± 2.5 nM for copper compounds.

4.3.3.2 Iron

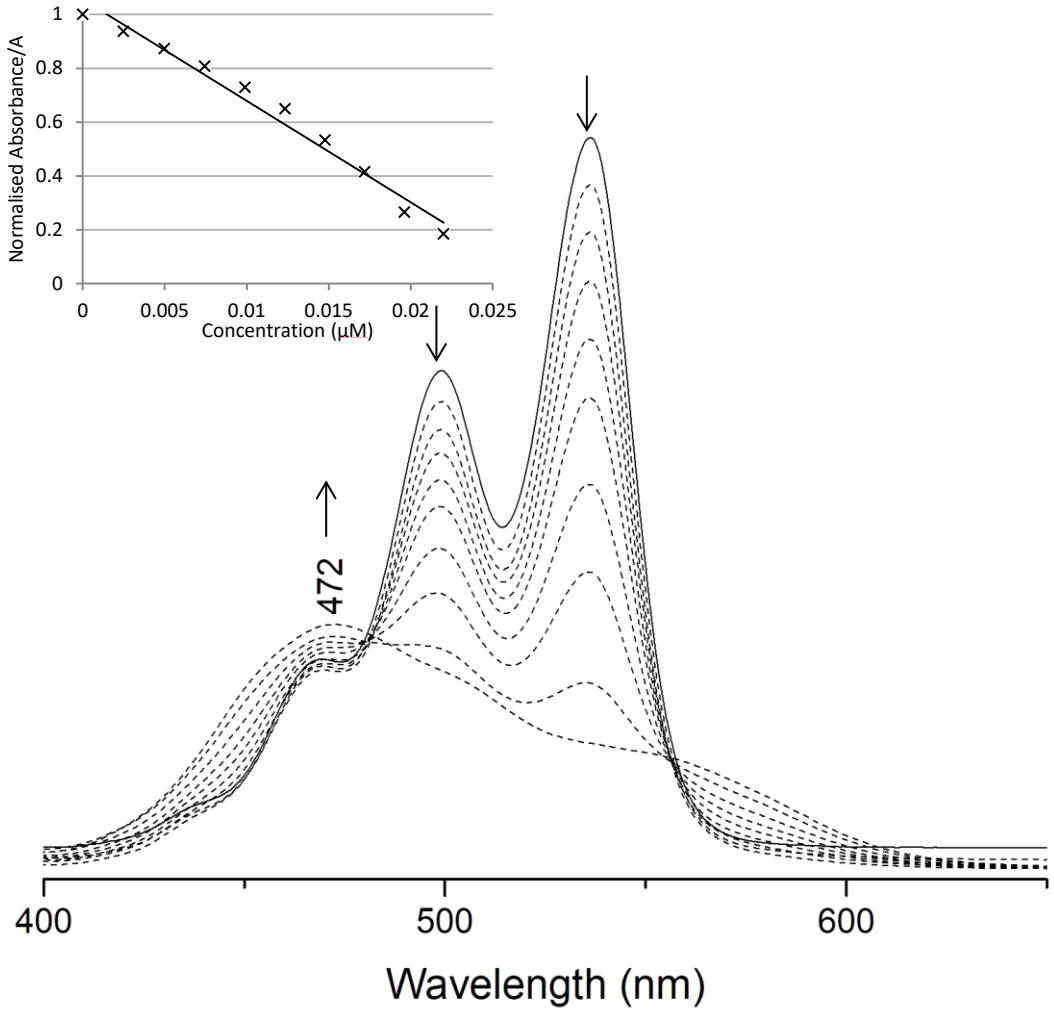

Figure 4.6 UV-Vis spectra of PDI solutions with successive additions of aqueous iron (III) nitrate solution (1 µM, 5 µL) and a comparison of λ_{536} absorbance vs concentration (inset).

Iron (III) nitrate was added in 5 µL increments of 1 µM solution to a solution of PDI and spectra were recorded over the range of additions. **Figure 4.6** shows an absorbance decrease at the 536 nm peak was linear (gradient = -37.7 A.µM^{-1}) within the range of 2.5 to 19.6 nM with a spread from the linear trend of 2.26 %. This was attributed to errors within

the pipette while additions were being made, and also mixing of the solution was achieved through trituration using a 1mL pipette. Iron (II) nitrate was also used to explore any observational changes with metal ions in different oxidation states, though with 10 µL additions of 1 µM solutions, good agreement (within 2% spread) was observed between the two solutions (**Appendix Figure A.5**). After initial PDI peaks were diminished, similar to copper spectra, a third peak gained absorbance at 472 nm. This peak was in a different position to the copper spectra and thus it was speculated that this response may be specific to each metal ion.

4.3.3.3 Titanium

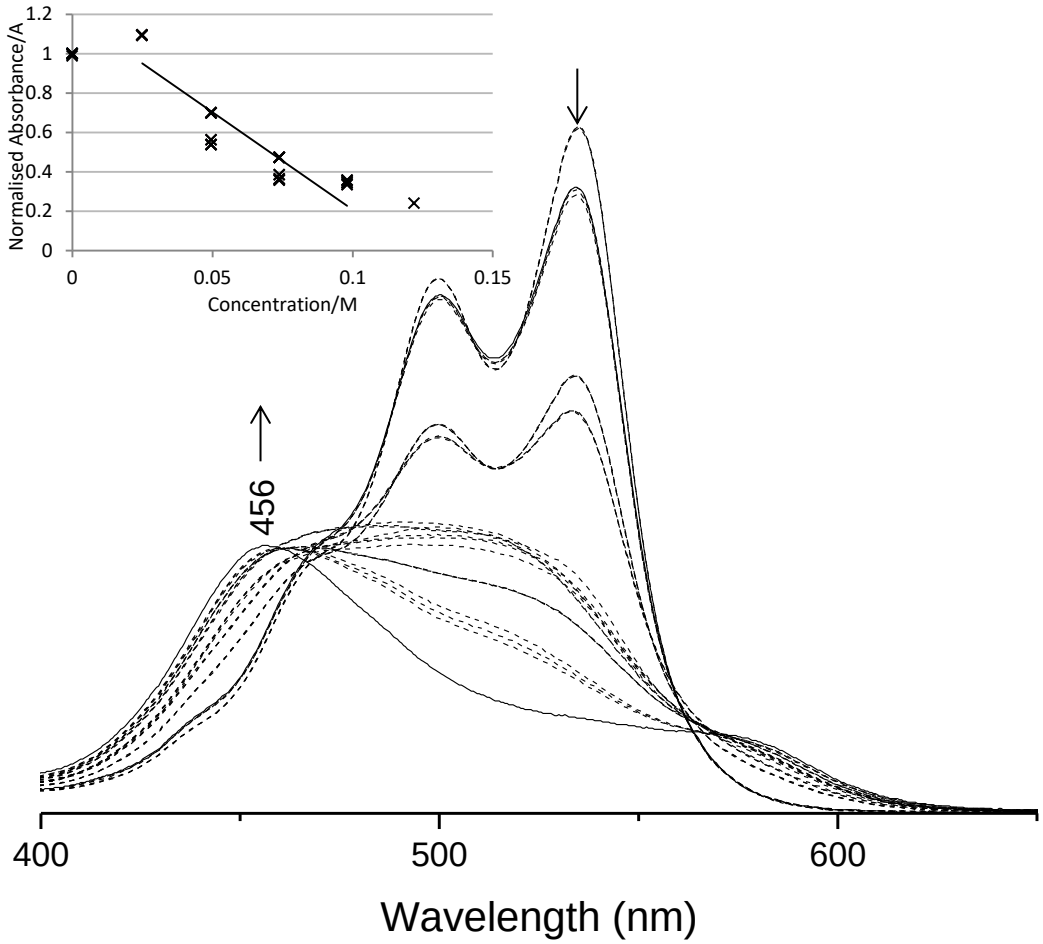

Figure 4.7 UV-Vis spectra of PDI solution with additions of titanium (III) chloride (5 µM, 10 µL) with graph of normalised λ_{536} absorbance vs concentration (inset).

Titanium (III) chloride solution was diluted to a concentration of 5 μM for addition in 10 μL aliquots to pre-prepared PDI solution. An initial increase in absorbance was attributed to electron donation from the metal which briefly enhanced absorbance. A gradient measuring relationship between λ_{536} absorbance and concentration was calculated to be -9.89 A.μM, less when compared to previously calculated relationships with metal concentration. The inset in **Figure 4.7** shows a large spread of absorbances recorded for the same concentration suggesting a weaker quenching response from the Ti^{3+} ion despite an additional acid presence.

The UV-vis spectra showed similar quenching behaviour of PDI found in previous metal ion test, however with a significantly decreased response per addition of solution. Compared to addition of acid to PDI solution, which showed the appearance and increase of peaks at 469 and 440 nm (**Figure 4.1**)

Figure 4.1, addition of a metal ion-containing solution resulted in a single peak at 456 nm. It was not possible to distinguish which stimuli was the cause of the absorbance decrease though the rate at which the response occurred suggests that the $TiCl_3$ solution was less reactive with PDI. This response could be a result of slower dissociation of the salt or less ground-state complexation with the Ti^{3+} ion. The single peak after additions of solution was in a different position again from those peaks observed with iron and copper solutions.

4.3.3.4 Zinc

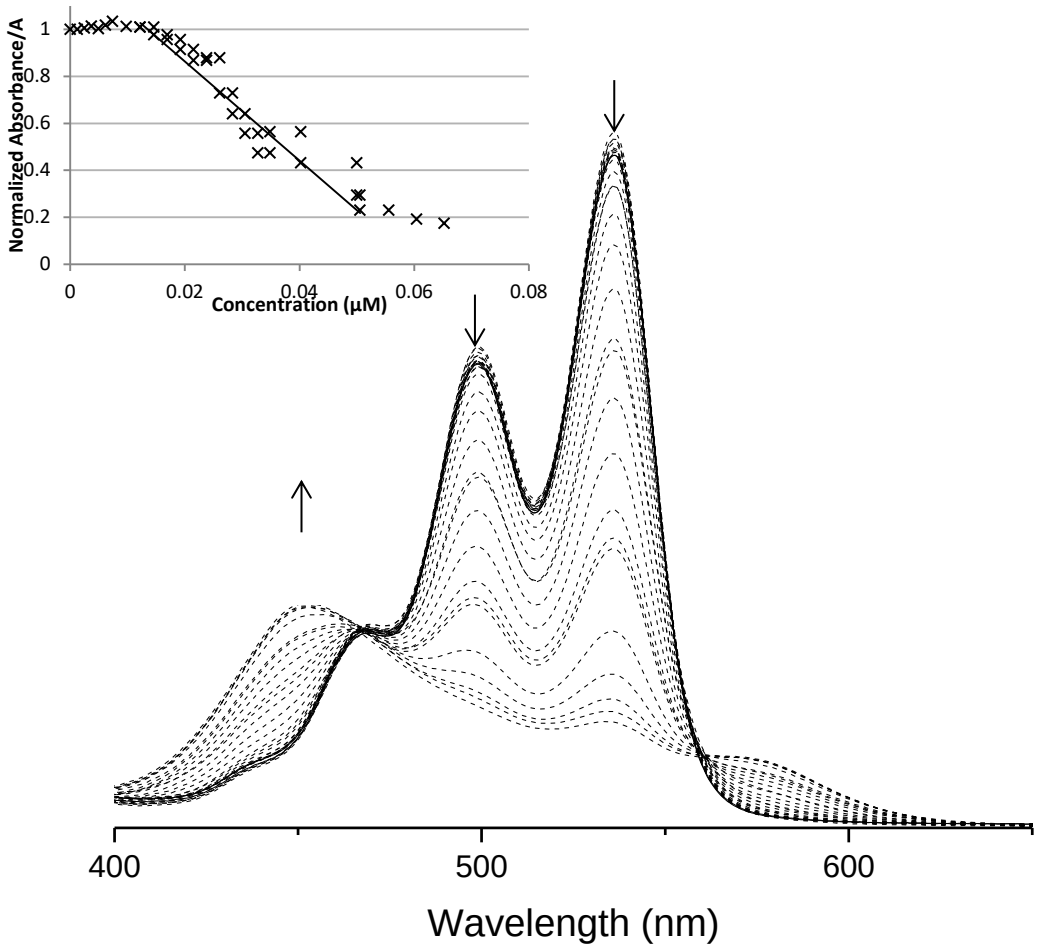

Figure 4.8 UV-Vis spectra of additions of zinc (II) nitrate (0.5 µM, 5 µL) to PDI solution with graph of λ_{536} absorbance plotted against concentration (inset).

Aqueous zinc nitrate solution was made up to 0.5 µM concentration and was added in 5 µL increments to a cuvette containing PDI solution until a final peak was distinguished at 453 nm. As with $TiCl_3$, an initial increase in absorbance was observed over the course of several additions of solution before PDI exhibited the expected λ_{536} absorbance reduction. The plotted absorbance decrease, **Figure 4.8**, after 14.5 nM, was calculated as a gradient of -13.4 $A.\mu M^{-1}$. However the spread from the plotted linear trend line was calculated at 4.62% which is a greater variation than previous metal solutions have yielded. By using the points for which there is the greatest variation between measurements, the smallest

precision with which zinc ion solution can be detected is ± 10 nM between the active 14.5 – 50.5 nM range.

4.3.3.5 Cobalt

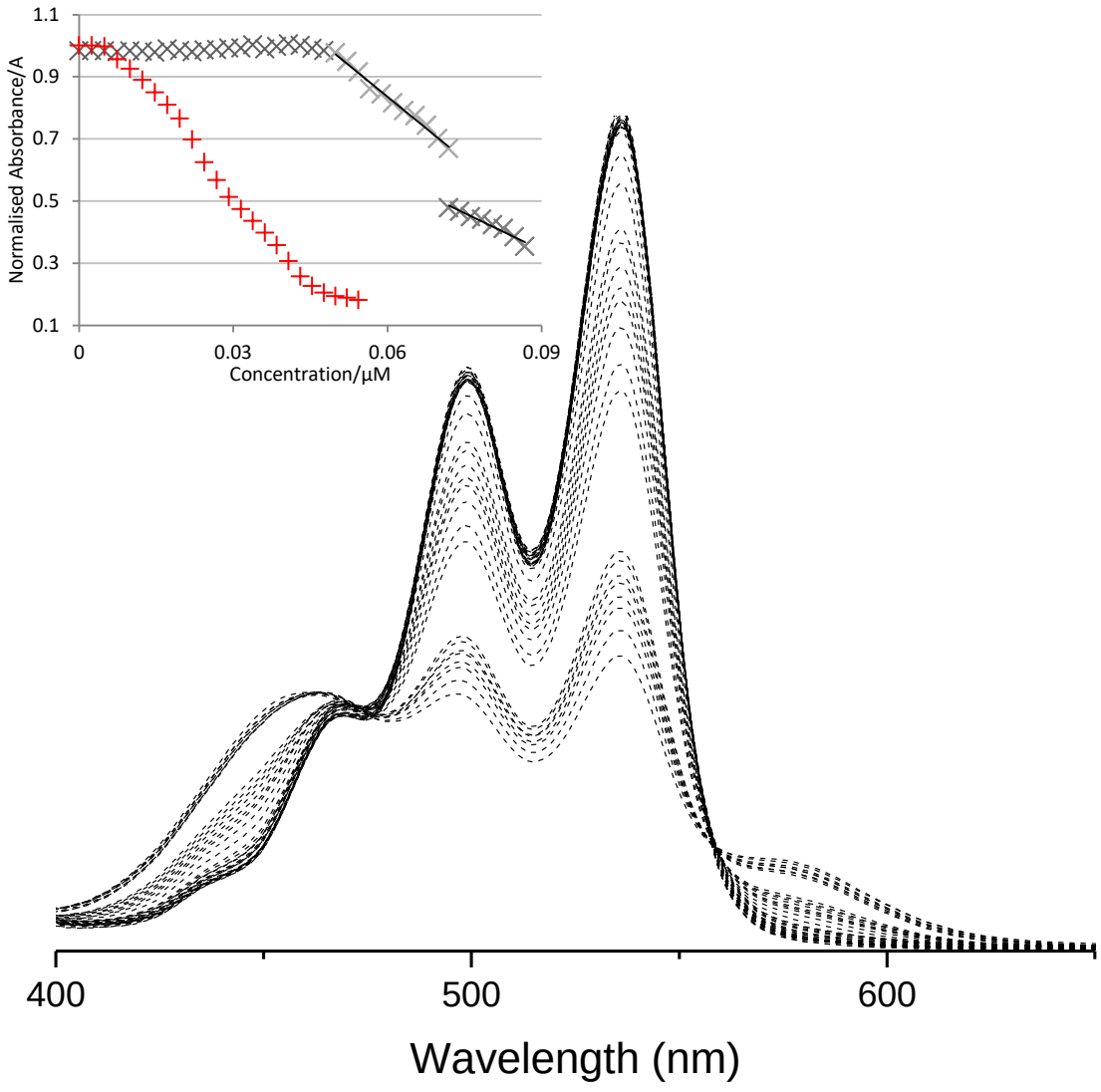

Figure 4.9 UV-Vis spectra of PDI solution with additions of aqueous cobalt (II) gluconate (1 µM, 5 µL) with a graph of λ_{536} absorbance vs concentration for $Co(OAc)_2$ (red) and Co(gluconate) (black) (inset).

Cobalt (II) gluconate was made up to 1 µM aqueous solution for 5 µL additions to the PDI solution to observe the effect, if any, of changing the ligand associated with the metal. The initial lowest detection limit for cobalt (ii) gluconate in solution was placed at 49.88 nM,

which was 10 times higher than that of cobalt (ii) acetate (**Figure 4.9** (inset)). This distinction was attributed to the change in ligand associated with the cobalt ion. Since in aqueous solution gluconic acid forms an equilibrium with glucono-δ-lactone which can chelate metal ions and form very stable complexes, especially in alkaline solution.[26] It was speculated that this reaction caused a stronger interaction between itself and cobalt, thereby leading to fewer interactions between cobalt ions and PDI molecules in solution.

A two hour gap between measurements occurred at concentration 72 nM and resulted in a further decrease in absorbance at 536 nm without any additional Co(glu) solution. Before this gap in measurements, the gradient formed by normalised absorbance λ_{536} vs Co(glu) concentration readings taken at 534 nm was -13.52 $A/\mu M^{-1}$, which was less than that of the gradient using cobalt acetate (-20.3 A.μM). However after the waiting period, the gradient further decreased to -7.93 $A.\mu M^{-1}$, indicating that the additional time resulted in a similar response to adding further metal solution to the point at which the PDI response begins to taper off. This response suggests a metal complex dissociation limiting factor. With an initial spread of 0.91 % from the trend line, and intervals between additions being < 5 minutes, this effect was studied further. The final peak visible in the spectra after all metal solution additions was observed at 461 nm.

4.3.3.6 Counter-ion effect

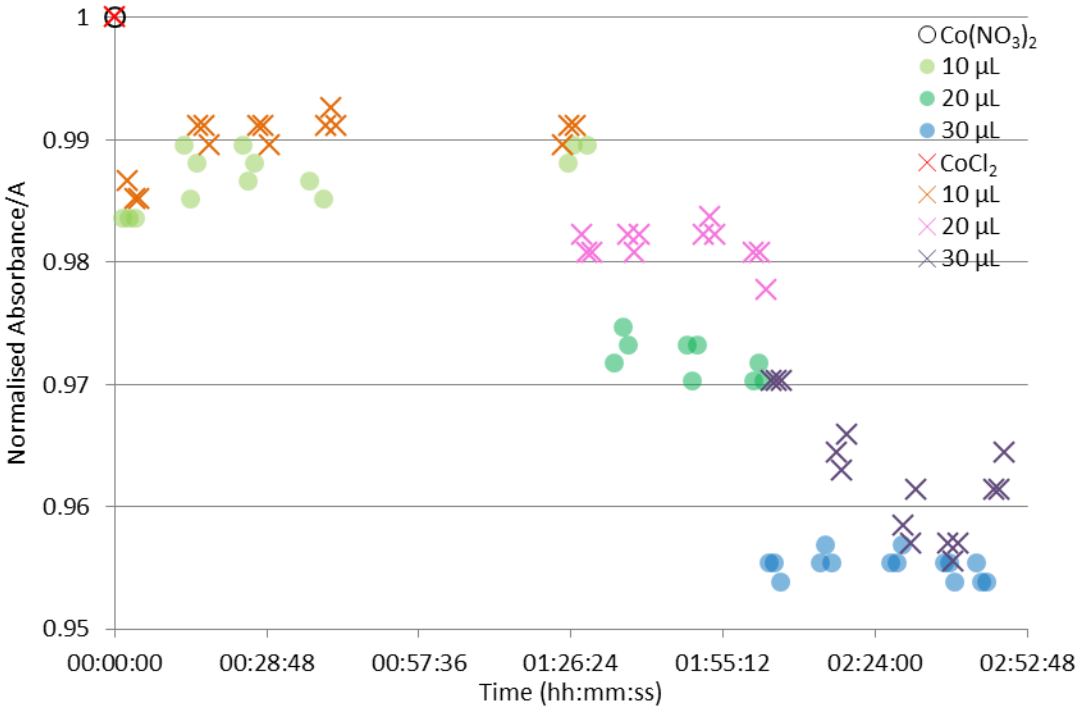

Figure 4.10 Graph of λ_{536} absorbance with increasing additions of metal solutions over time, $Co(NO_3)_2$ and $CoCl_2$ to PDI.

A further investigation into the effect of the associated counter-ion to the metal was conducted to observe changes in λ_{536} normalised absorbance. After each addition of metal solution, spectra were recorded at ten minute intervals and then again after an hour before another metal solution addition. **Figure 4.10** shows that with increased concentration there is a decrease in λ_{536} absorbance, though between nitrate ions and chloride ions, the recorded absorbances begin to deviate with time and concentration. Cobalt nitrate appeared to show smaller deviations after the initial change in absorbance with solution addition, though cobalt chloride is much less consistent. PDI spectra with additions of iron salt solutions (Appendix Figure A.6) displayed a discrepancy between how the PDI absorbance responded to its presence. $Fe(NO_3)_2$ additions gave consistent decreases in absorbance followed by a slight increase in absorbance minutes after the addition, while additions of $FeCl_2$ showed a smaller response that showed an overall decrease in

absorbance after the addition. Furthermore, incremental additions of $TiCl_3$ with spectra measured over time (Appendix Figure A.7) showed an initial increase in absorbance, from a normalised value, before decreasing over time and with further additions of solution.

4.3.3.7 Metal identification

Table 4.1 Table of final PDI peak wavelengths and the concentrations at which the absorbance is observable.

Metal	Final peak wavelength (nm)	Observable absorbance concentration
Copper	452	22.0 nM
Iron	472	22.0 nM
Zinc	453	50.6 nM
Titanium	456	122.0 nM
Cobalt	461	47.6 nM

The positions of the peaks described in **Table 4.1** arise at different concentrations for the metals stated. This was related to the initial concentration at which PDI shows a response to the presence of metal ions as well as the rate at which the absorbance changed with concentration. With the exception of titanium, there appeared to be a correlation with ionic radii, though titanium has been recorded as having a smaller radii than its peak position would suggest.[27] The presence of this peak is a promising suggestion that this PDI solution can selectively identify metal ions in solution at concentrations as low as 22.0 nM.

4.4 Conclusions

In this chapter an aqueous PDI solution concentration was optimised before its use as a sensing solution. Fluorescence and UV-Vis spectroscopy were employed to ensure efficient absorption of light while preventing signals becoming indistinguishable from each other at higher concentrations.

Fluorescent spectra for PDI solutions were recorded and an initial solution of copper (II) chloride was made up in water as a stimulus to quench the fluorescence. A predicted decrease in fluorescence emission was measured with increasing copper concentration. Limited emission intensity prevented accurate measurements from being made since the maximum intensity peak position could not be determined with great enough precision.

UV-Vis was used as a preferable spectrometry technique for sensing with PDI and was used to test PDI response to metal solutions. For each metal salt used, the initial change in absorbance was recorded, the rate of absorbance change at 536 nm was measured against concentration, and the position of the peak formed with significant metal ion addition was recorded. Counter ions appeared to have an effect on the initial response and the rate at which PDI responded to the concentration of metal.

Initial testing over the range of the PDI response did not how a difference between nitrate and chloride anions, though testing over time revealed deviations from the initial absorbance change. Final peak position for PDI solutions, with significant additions of metal ions, was specific to each metal ion tested suggesting PDI solution could distinguish between metal ions in solution with a minimal detection limit of 22.0 nM. This promising result requires further testing to confirm the response is consistent over more materials.

4.5 References

1 V. K. Gupta, C. K. Jain, I. Ali, M. Sharma and V. K. Saini, *Water Research*, 2003, **37**, 4038–4044.

2 J. J. Mortvedt, *Fertilizer research*, 1995, **43**, 55–61.

3 N. S. Shaban, K. A. Abdou and N. E.-H. Y. Hassan, *Beni-Suef University Journal of Basic and Applied Sciences*, 2016, **5**, 102–106.

4 N. Defarge, J. Spiroux de Vendômois and G. E. Séralini, *Toxicology Reports*, 2018, **5**, 156–163.

5 P. S. Hariharan, J. Pitchaimani, V. Madhu and S. P. Anthony, *Journal of Fluorescence*, 2016, **26**, 395–401.

6 N. N. Lathiotakis, I. S. K. Kerkines, G. Theodorakopoulos and I. D. Petsalakis, *Chemical Physics Letters*, 2018, **691**, 388–393.

7 D. Sriramulu and S. Valiyaveettil, *Dyes and Pigments*, 2016, **134**, 306–314.

8 J. Wang, E. He, X. Liu, L. Yu, H. Wang, R. Zhang and H. Zhang, *Sensors and Actuators, B: Chemical*, 2017, **239**, 898–905.

9 L. Shang and S. Dong, *Biosensors and Bioelectronics*, 2009, **24**, 1569–1573.

10 H. Cheng, Y. Zhao, H. Xu, Y. Hu, L. Zhang, G. Song and Z. Yao, *Dyes and Pigments*, 2020, **180**, 108456.

11 D. Pfeifer, I. Klimant and S. M. Borisov, *Chemistry - A European Journal*, 2018, **24**, 10711–10720.

12 X. Zhang, S. Rehm, M. M. Safont-Sempere and F. Würthner, *Nature Chemistry*, 2009,

1, 623–629.

13 S. K. Yang, X. Shi, S. Park, S. Doganay, T. Ha and S. C. Zimmerman, *Journal of the American Chemical Society*, 2011, **133**, 9964–9967.

14 S. Chen, P. Slattum, C. Wang and L. Zang, *Chemical Reviews*, 2015, **115**, 11967–11998.

15 T. L. Mako, J. M. Racicot and M. Levine, *Chemical Reviews*, 2019, **119**, 322–477.

16 T. Martyński, R. Hertmanowski, R. Stolarski and D. Bauman, *Thin Solid Films*, 2008, **516**, 8834–8838.

17 A. Miyata, D. Heard, Y. Unuma and Y. Higashigaki, *Thin Solid Films*, 1992, **210**–**211**, 175–177.

18 E. R. Draper, B. J. Greeves, M. Barrow, R. Schweins, M. A. Zwijnenburg and D. J. Adams, *Chem*, 2017, **2**, 716–731.

19 X. Zhao, K. Zhao and P. Sun, *Chemical Physics Letters*, 2019, **730**, 582–586.

20 A. Dannenhoffer, H. Sai, D. Huang, B. Nagasing, B. Harutyunyan, D. J. Fairfield, T. Aytun, S. M. Chin, M. J. Bedzyk, M. Olvera De La Cruz and S. I. Stupp, *Chemical Science*, 2019, **10**, 5779–5786.

21 B. Wang and C. Yu, *Angewandte Chemie International Edition*, 2010, **49**, 1485–1488.

22 J. M. Seco, E. San Sebastián, J. Cepeda, B. Biel, A. Salinas-Castillo, B. Fernández, D. P. Morales, M. Bobinger, S. Gómez-Ruiz, F. C. Loghin, A. Rivadeneyra and A. Rodríguez-Diéguez, *Scientific Reports*, 2018, **8**, 14414.

23 J. Y. Kim, S. W. Woo, J. W. Namgoong and J. P. Kim, *Dyes and Pigments*, 2018, **148**, 196–205.

24 T. Salthammer, H. Dreeskamp, D. J. S. Birch and R. E. Imhof, *Journal of Photochemistry and Photobiology, A: Chemistry*, 1990, **55**, 53–62.

25 D. J. S. Birch, K. Suhling, A. S. Holmes, T. Salthammer and R. E. Imhof, *Pure and Applied Chemistry*, 1993, **65**, 1687–1692.

26 Gluconic acid | C6H12O7 - PubChem, https://pubchem.ncbi.nlm.nih.gov/compound/10690, (accessed 6 March 2019).

27 R. D. Shannon, *Acta Crystallographica Section A*, 1976, **32**, 751–767.

Chapter 5 Perylene Diimide Derivative Nanofibres as Electrode Materials

5.1 Introduction

As energy-requiring products increase in number and diversify in their needs, reliable and quick-charging storage must be developed to fill the demands. Li-ion batteries are capable of large amounts of energy storage thanks to their bulk redox reaction. Whereas, for applications such as electric cars, the low power density of Li-ion cannot keep up with requirements for acceleration, braking, and hill climbing. Supercapacitors generally possess much higher power density and are capable of harvesting energy in short time periods and also providing short bursts of energy.[1]

Both electrochemical double-layer capacitors (EDLCs) and pseudocapacitors store charge at the interface between an electrode and the electrolyte. EDLCs store charge through reversible ion adsorption while pseudocapacitance involves an electron charge transfer between the electrode and the electrolyte. [2,3] As such an electrode material capable of providing a large surface area is ideal for supercapacitor applications.

Carbon materials are widely used in electrochemical capacitors as electrodes due to their low cost, wide availability, diverse morphologies, and thermal and chemical stability.[4–9] Carbon nanofibres (CNFs) specifically can possess high surface areas, attractive porosity, and flexibility. CNFs may be produced by carbonising carbon rich polymers or sustainable biomass. The properties of carbon materials can be tuned by choosing suitable carbon precursors or post-modification.

Perylene-3,4,9,10-tetracarboxylic acid diimide derivatives or perylene diimide derivatives (PDIs) have previously been extensively studied as dyes and pigments and display excellent chemical, thermal, and photo stability.[10–14] Due to their strong hydrophobicity PDIs can self-assemble into nanostructures via π-π interactions and also interactions between side chains, the resulting assembled fibres may be carbonised to yield CNFs.[15,16] In addition to self-assembly, electrospinning can also be used to generate PDI nanofibres.[17,18] By exploring both self-assembly and electrospinning, it is possible to more easily influence the properties of the resulting nanofibres from an earlier stage using less harsh conditions.

After carbonisation, materials from Chapter 3 were analysed for their suitability as electrode materials. This was primarily conducted through use of analytical techniques, that is, Raman spectroscopy and gas sorption analysis for carbon structural information and surface area analysis respectively. Finally, materials were tested using cyclic voltammetry and galvanostatic method for their performance as a supercapacitor electrode material as well as potentially a lithium ion anode.

5.2 Experimental

5.2.1 Chemicals and Materials

PDI was synthesised as detailed in Chapter 3. Hydrochloric acid (37%), sodium hydroxide (≥97%), glucono-δ-lactone (GdL) (≥ 99 %), potassium hydroxide (≥85%), sodium sulfate (≥99%), sulfuric acid (95%), phosphoric acid (≥85%), triethylamine (TEA) (≥99%), N,N-dimethylformamide (DMF) (99.8%), polyacrylonitrile (PAN) (MW 150 000 $g.mol^{-1}$), polyethylene glycol (PEG) (Mw 400 000 $g.mol^{-1}$), N-methyl pyrrolidone (NMP) (99.5%), and polyvinylidene fluoride (PVDF) (MW ~180 0000 $g.mol^{-1}$) were purchased from Sigma-Aldrich and used without further purification. Ethanol (≥ 99.9 %) was obtained from Brenntag and used as received.

5.2.2 Self-Assembled Fibres

Self-assembled fibres were formed using the same procedure detailed in Chapter 3. The conditions for each self-assembly are stated in **Table 5.1**.

Table 5.1 PDI samples with their stated self-assembly conditions and observed fibre dimensions before and after cabonisation.

Sample	Conditions	Diameter (nm)		Carbonisation % Yield
		Bef.	Aft.	
CSP.5.1	[PDI (0.06 M), NaOH (0.18 M), water (5 mL)] + *[H_3PO_4 (0.18 M), water (5 mL)]*	48	121	33.83%
CSP.5.2	[PDI (60 mM), Imidazole (0.06 M), water (1 mL)] + *[GdL (0.66 M), Graphene oxide (0.5 mL, 6.2 g.L^{-1}), water (0.5 mL)]*	46	25	33.51%
CSP.5.3	[PDI (60 mM), Imidazole (0.24 M), water (4 mL)] + *[GdL (0.28 M), water (4 mL)]*	61	52	57.63%

5.2.3 Electrospun fibres

Electrospun fibres were also produced as detailed in Chapter 3. Their parameters and conditions for spinning are listed in **Table 5.2**.

Table 5.2 Table of electrospun fibre samples and their production conditions, fibre diameters before and after carbonisation, and percentage yield after carbonisation

Sample	Concentration			Conditions	Diameter (nm)		% Yield
	Polymer	PDI	Solvent		Bef.	Aft.	
CEP.5.1	PAN (6 wt.%)	10 m M	DMF + TEA (0.12 M)	22 kV 0.4 $mL.h^{-1}$	181	154	14.54%
CEP.5.2	PAN (8 wt.%)	10 m M	DMF + TEA (0.12 M)	22.0 kV 0.4 $mL.h^{-1}$	440	398	22.65%
CEP.5.3	PEG (5 wt%)	90 m M	Aqueous imidazole (0.36 M)	10.0 kV 0.25 $mL.h^{-1}$	192	54	23.05%
CEP.5.4	PEG (3 wt%)	70 m M	Aqueous imidazole (0.28 M)	10.0 kV 0.1 $mL.h^{-1}$	511	54	16.63%

5.2.4 Carbonisation conditions

Fibres produced by either self-assembly or electrospinning were collected and weighed into an alumina crucible (15 mL, 102 x 20 x 14 mm). Standard carbonisation conditions all took place within sealed tube furnace. Samples were degassed with Nitrogen for 30 minutes before heating to 200°C at 2°C/min and holding for 2 hours. Further heating up to 800°C at a rate of 3°C/min then held at temperature for 2 hours.

5.2.5 Characterisation

^{1}H NMR spectra were recorded using a JEOL JNM-ECZR 500 MHz. PDI powder was dispersed in [D_6]DMSO in a sample vial before being transferred via syringe and syringe filter to a standard 5 mm tube. Fibres were observed using field-emission scanning electron microscopy (FESEM) on a JEOL FESEM JSM6700F. Materials were affixed to the sample holder using carbon tape before coating with a thin layer of gold for 30 seconds. Raman

spectra were recorded by placing the sample onto an aluminium slide and fitting it into the attached microscope on a RAMAN Micro Raman system JYT64000. Scans were performed for an initial 10 seconds before moving position of the laser and scanning for 1 second at each new location. Brunauer Emmett Teller analysis was conducted on a Micrometrics ASAP 2020 surface area and porosity analyser upon ~0.1 g after degassing for 10 hours at 150°C. Electrochemical measurements were performed on a PGSTAT302, Autolab for Li-ion batteries, and CHI 660D electrochemical analyser for cyclic voltammetry measurements.

5.2.6 Electrochemical Testing

5.2.6.1 Supercapacitor Testing

A slurry of active material (90%) and PVDF pellets (10%) were combined to a concentration of 1 $mg.cm^{-3}$ in N-methyl pyrrolidone (NMP). An accurate volume of 11 µL was pipetted onto the surface of a 1 cm^2 carbon disc and the NMP allowed to evaporate in an oven overnight. The coated carbon disc was assembled into an electrode using copper wire and a PTFE tape coating, leaving only the coated face of the electrode exposed to the electrolyte.

Evaluating nanofibres as electrode materials was performed using cyclic voltammetry using a voltage window of -0.6 – 0.6 V and 1 M electrolyte solution. Alkaline, neutral, and acidic electrolytes were used, KOH, Na_2SO_4, and H_2SO_4 respectively . A three-electrode system was used with the sample as working electrode, a platinum wire counter electrode, and a Ag/AgCl reference electrode attached to a CHI 660D electrochemical analyser for measurement recordings.

5.2.6.2 Li-Ion Battery Testing

A slurry of active material (80 wt. %) and carbon black (10 wt. %) was added to the PVDF in NMP binder mentioned in *5.2.6.1* such that PVDF binder was present in 10 wt. % of the

total weight of the mixture. The active material slurry was deposited onto a copper current collector uniformly using a razor blade and dried at 100°C for 4 hours in air. The dry coated foil was pressed under a load of ~1000 kg before discs were punched out from the foil and weighed. 2032 button cells were assembled in an argon glove box using lithium foil as a counter electrode and 1 M $LiPF_6$ in ethylene carbonate/dimethyl carbonate (1:1 v/v ratio) as the electrolyte.[19,20] Charge-discharge curves were measured at current density 50 $mA.g^{-1}$ with a PGSTAT302, Autolab. The coin cell was charged between 0.0 – 3.0 V for 6 cycles.

5.3 Results and Discussion

Fibres produced and carbonized as described in **5.2.2**, **5.2.3**, and **5.2.4** were studied for their physiochemical properties and potential usage as electrode materials in supercapacitors. To facilitate understanding of their properties samples were analysed using N_2 sorption analysis for surface area measurements as well as Raman spectroscopy for graphitic content of material. The potential of these CNFs was then examined by cyclic voltammetry. Finally, testing of sample CE063 in a lithium-ion cell was also conducted.

5.3.1 Raman

As stated above, Raman spectroscopy was used to gain structural information about carbon materials by making use of Raman active vibrational modes since Raman spectroscopy is particularly sensitive to carbon microstructures. For all samples (**Table 5.3**), overlapping peaks were present in Raman spectra around 1350 and 1580 cm^{-1} wavenumbers corresponding to D- and G-bands respectively, after excitation with laser light at wavelength 532 nm.[21–25]

While ratios between D- and G-bands can be most accurately used to describe the population of sp^2 and sp^3 carbon, it is worth noting that its accuracy is reliant on the sample

containing only carbon. Also, the G mode of stretching relates to E_{2g} symmetry which can be found in the in-plane bond-stretching motion of pairs of carbon sp^2 atoms.[21–25] These bonds are not required to be found in six-membered rings and can occur due to olefinic molecules.

Table 5.3 Table of Raman results with labelled D- and G-band peak wavenumbers, fitted peak heights(I_D, I_G), and calculated area ratio (A_D/A_G).

Sample	D-band wavelength	G-band wavelength	I_D	I_G	A_D/A_G
CSP.5.1	1353.31	1596.27	302.10	296.30	2.59
CSP.5.2	1346.04	1581.93	214.79	189.80	2.60
CSP.5.3	1347.31	1588.98	257.11	244.93	3.27
CEP.5.3	1338.01	1586.81	892.46	867.55	2.15
CEP.5.4	1342.19	1572.81	155.19	137.53	3.18

With each sample tested, multiple points were exposed to the laser for measuring spectra to receive more reliable results without sampling areas damaged by the laser from previous measurements. Previous studies have used full-width half maximum[26] (FWHM) to state measurement, others have used just peak intensity[27–29]. Spectra were fitted with Lorentzian peaks, the values for which were used to calculate the ratio between peak area in **Table 5.3**. In the interest of accuracy, both A_D/A_G and peak height ratios will be discussed.

For samples **CSP.5.1** and **CSP.5.2**, fitted peak heights and A_D/A_G values agree with peak heights measured directly from the spectra that there is a greater proportion of disorder present. Between the measurement parameters generated by lorentzian peak fitting and those takes directly from the spectra there is good agreement even about the proportion of disorder compared to graphite with peak height ratios for CSP.5.1 = 1.02/1.02 and CSP.5.2 = 1.13/1.18 with fitted/spectra values respectively.

Highly ordered pyrolytic graphite (HOPG) has a spectral peak recorded at 1581 cm^{-1} corresponding to the E_{2g} stretching mode,[24,30] the only mode allowed in pure graphite. With

introduction of impurities into the ideally perfect structure, not only does a separate spectral band associated with disordered carbon appear, often the initial graphitic peak shifts. With the samples presented in **Table 5.3**, the shift in graphitic peak position is related to a non-perfect graphite structure as a result of nitrogen presence in the initial molecule as well as any fusing of fibres during carbonisation.

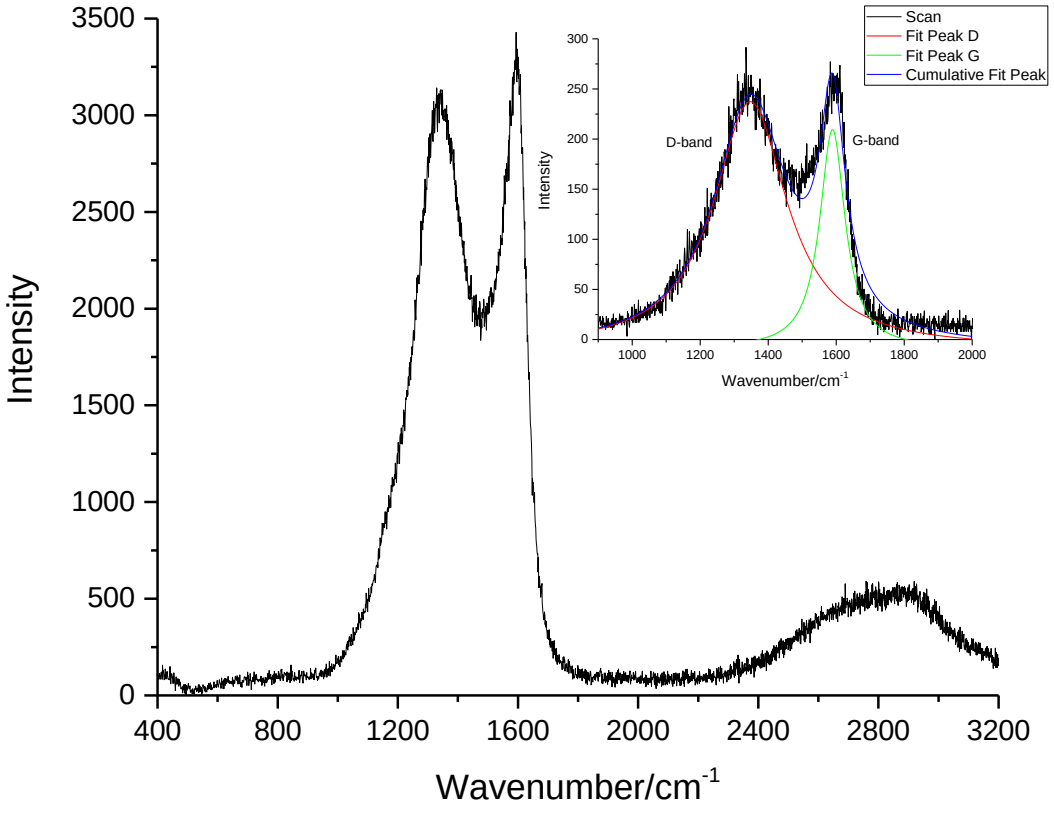

Figure 5.1 sample **CSP.5.3** Raman spectra collected between 400 – 3200 cm^{-1} with Lorentzian peak fitting between 900 – 2000 cm^{-1} (inset).

Though peak height values taken directly from the spectra in **Figure 5.1**

Figure 5.1infer that there is a greater amount of graphitic carbon. A_D/A_G measured by peak fitting agrees with the ratio between fitted peak heights, that there is a greater proportion of disordered carbon. The broad peak across the range 2600 – 3000 cm^{-1} was identified as overlapping second order Raman spectral bands. Poor definition of peaks from one another agrees a greater proportion of disordered carbon present as stated by the ratio (=3.27) provided by peak fitting, (**Table 5.3**).

This increased disorder could be due, in part to the self-assembly process and fibre isolation method used. In such that after the self-assembly occurs, within the solution it is possible there are still free PDI molecules with aggregate upon filtration and washing with water and ethanol. This aggregation is rapid and uncontrolled, leading to disordered morphologies.

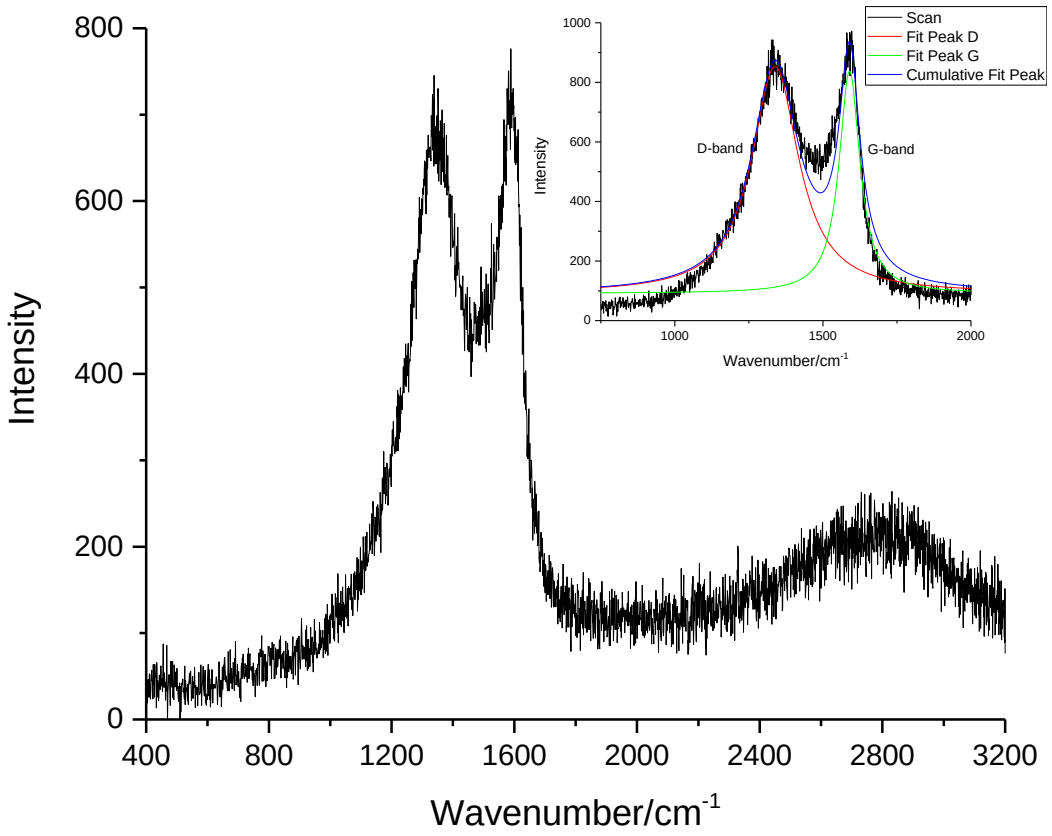

Figure 5.2 Sample **CEP.5.3** Raman spectra collected between 400 – 3200 cm^{-1} with Lorentzian peak fitting between 900 – 2000 cm^{-1} (inset).

Compared to **CSP.5.3**, sample **CEP.5.3** in **Figure 5.2** showed a lesser ratio of disorder, with an A_D/A_G value of 2.15. Though Peak heights measured directly from the spectra indicated more graphitic content, fitted peak heights agreed with the A_D/A_G value, that there is still a greater degree of disorder compared to graphitic content. Comparing the ratio of G-band to D-band for sample **CEP.5.3** to other samples recorded, the A_D/A_G value infers much lower disordered content. However the peak height ratios are comparable between **CEP.5.3** and **CSP.5.1**, as such the difference lies in peak width which could be a result of resonant raman processes.[30,31] This increase in comparative graphitic content could be due to the

electrospinning process used which could have caused a greater yield of fibres rather than a mixture of fibres and aggregated PDI.

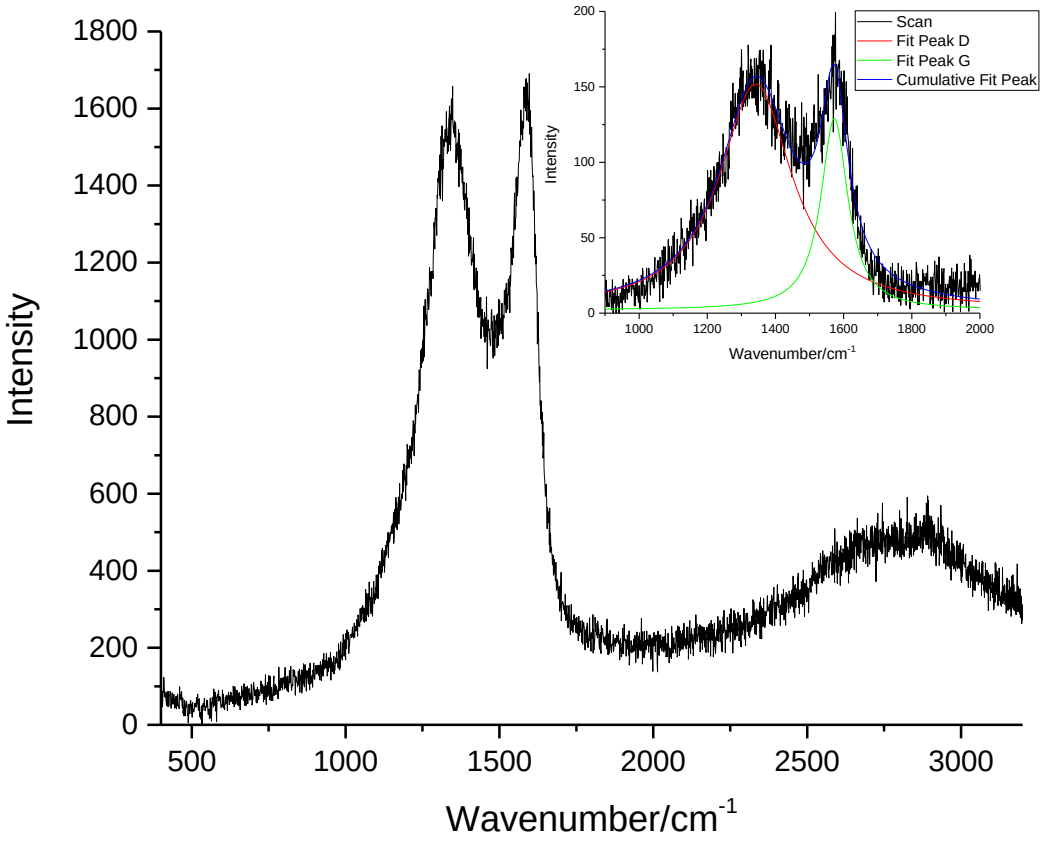

Figure 5.3 sample **CEP.5.4** Raman spectra collected between 400 – 3200 cm-1 with Lorentzian peak fitting between 900 – 2000 cm^{-1} (inset)

Despite using the electrospinning production method, more disorder was observed in **Figure 5.3** for sample **CEP.5.4** in all three parameters measured between 900-2000 cm^{-1}. This was thought to be caused by a majority beads in the pre-carbonised sample prohibiting the fibre formation which occurred in **CEP.5.3** due to a lower concentration of PEG. While **CEP.5.4** had an A_D/A_G value of 3.18, it's I_D/I_G value was comparable to **CSP.5.3**.

5.3.2 Brunauer Emmett Teller Theory (BET)

Electric double-layer capacitance mechanism proposes that no interactions between the electrolyte and the electrode surface occur but rather, the electrode surface possesses

charge density which must be balanced by the surrounding electrolyte ions to maintain neutrality, as such, a potential difference results across the interface. Using this model, the ideal capacitor electrode should possess a high surface area in order to generate a larger double-layer and thus a larger capacitance should be possible. In contrast Li-ion batteries, while also benefitting from a large accessible surface area rely on accessible pores into which lithium ions may intercalate into the material itself.

BET theory was used to describe characteristic surface features including surface area and porosity, as well as average pore diameter. By utilising physisorption of nitrogen molecules on the surface at specific pressures, the amount adsorbed onto the surface can be used to calculate the surface area of the sample. Values for adsorption surface area were calculated, as mentioned in Chapter 2, using the linear section of a plot of $\frac{1}{[Q(p^*/p-1)]}$ against $\frac{p}{p^*}$, where *Q* is the quantity of nitrogen adsorbed in mmol.g^{-1}, p is the equilibrium pressure, and p* is the saturation pressure of the adsorbates.

The gradient and y-intercept of this plot can be used to calculate the volume of gas required to form a monolayer. This value can be substituted into the ideal gas equation to find the number of nitrogen molecules on the surface at standard temperature and pressure and, using the cross-sectional area of a nitrogen molecule, the surface area can be calculated.

Table 5.4 Properties of CNFs as characterised by N_2 sorption analysis

Sample	Mass (g)	Pore Volume (cm^3/g)	Pore Radius (nm)	Adsorption Surface Area (m^2/g)
SP.5.3 (before carbonisation)	0.0816	0.953	24	31 ± 0.55
CSP.5.3	0.0694	0.0777	13	231 ± 2.01
CEP.5.3	0.0787	0.394	7	285 ± 8.47
CEP.5.4	0.0259	0.667	19	183 ± 0.33

Surface area values were calculated using a manually generated linear plot of the relative pressure and a function of relative pressure with quantity adsorbed. This ensured that the accepted linear plot values fell within a spread of >95% agreement with the linear trend value. Pore volume and pore radius were generated by ASAP 2020 software using BJH calculations.

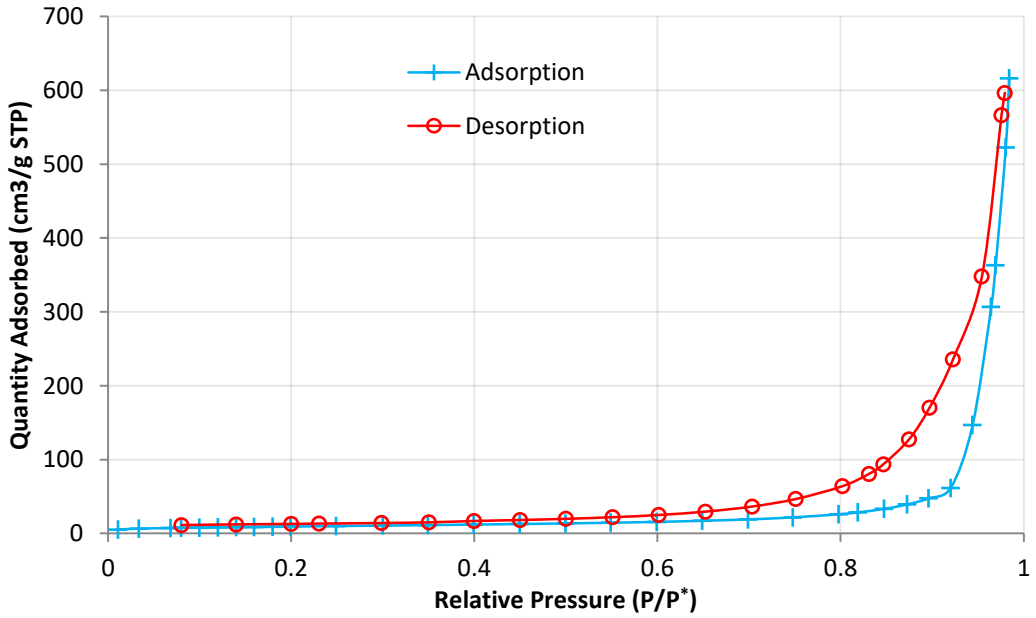

Figure 5.4 BET isotherm of non-carbonised sample **SP.5.3** using N_2 sorption.

PDI self-assembled fibres in **Figure 5.4** before carbonisation show a type III isotherm indicating a non-porous material with a low energy of adsorption.[32,33] Before carbonisation it is also possible to observe an increased adherence of nitrogen to the surface of the

material during desorption. The hysteresis loop in this isotherm was categorised as H3 which was recognized as a result of slit-like micropores which would naturally arise when dealing with π-π stacking of plate-like molecules. It was speculated that these slit-like pores arose due to stacking of plate-like PDI molecules.[32,33]

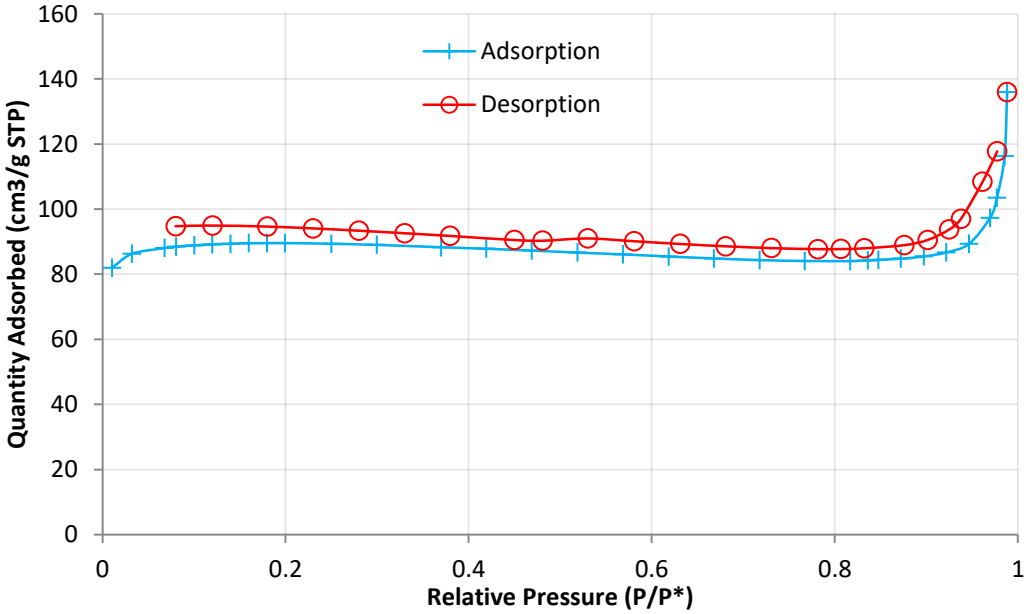

Figure 5.5 Sample **CSP.5.3** BET isotherm using N_2 sorption.

Figure 5.5 shows a Type II isotherm, also with a hysteresis loop resembling type H3. In this case, as the sample has formed CNFs after carbonisation, it is reasonable to assume the material is mimicking macroporosity due to the entangled nature of the initially formed fibres. BET pore size data differed from BJH pore radius by a large proportion, with BET calculations providing a pore width of 3.17 nm compared to 13.29 nm in **Table 5.4**. This discrepancy was again associated with the entangled nature of fibre formation through self-assembly causing some gaps between individual fibres to be mistaken for, and measured as, pores.

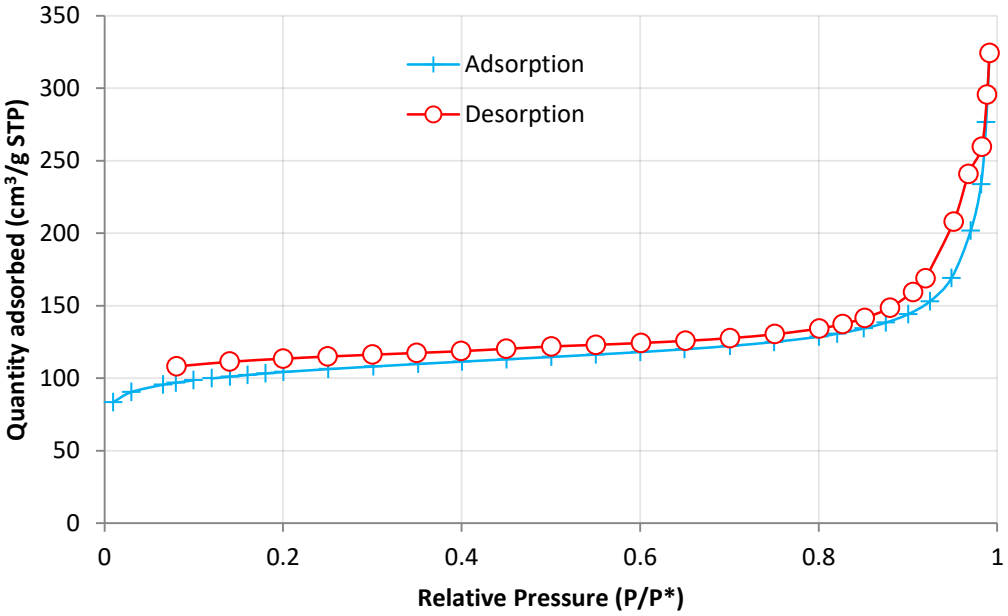

Figure 5.6 BET isotherm of sample **CEP.5.3** using N_2 sorption.

As with **Figure 5.5**, **Figure 5.6** shows a type II isotherm which indicates the material is non-porous, with an off-set desorption branch possibly describing an H3 loop or a greater energy of adsorption causing nitrogen molecules to be slow to desorb. The type II isotherm suggests a material with a higher energy of adsorption that is macroporous, in this case mimicking macroporosity between individual fibres. BJH pore radii were calculated at 6.34 nm, though a plot of pore volume against pore radii (Appendix **Figure A.3.4**) placed a population of pores around 2 nm in radii.

Compared to the self-assembled fibres analysed in **Figure 5.5**, a slightly higher surface area was measured for sample CEP.5.3. This was associated with the fibre production method, such that electrospinning PDI in a style reminiscent of evaporation-triggered self-assembly led to a greater proportion of fibres in the initial sample with less disorganised PDI aggregates. Since both types of fibre production appear to have resulted in mostly non-porous materials, it is likely that the discrepancy in sample surface area was a result of number of one-dimensional fibres.

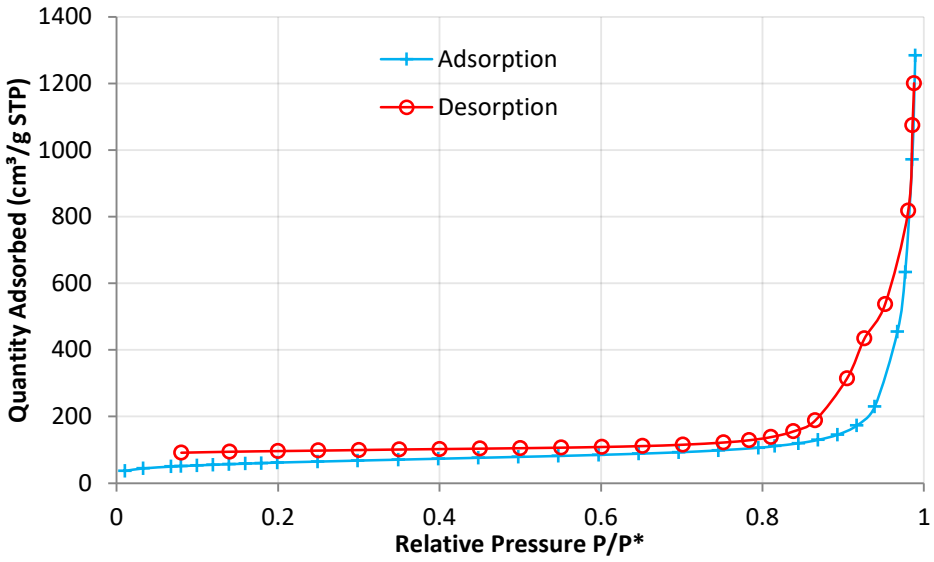

Figure 5.7 BET isotherm for sample **CEP.5.4** using N_2 sorption.

Contrasting with the type II isotherm of **CEP.5.3**, the isotherm for **CEP.5.4**, presented in **Figure 5.7**, appears more as a type III isotherm, similar to the pre-carbonised sample of **SP.5.3** in **Figure 5.4**. The values for quantity of nitrogen adsorbed are higher than those of the pre-carbonised material, as well as a small initial shelf at low relative pressure confirming the isotherm as actually type II. Overall surface area was comparable with **CSP.5.3** and **CEP.5.3** though lower than both samples due to structural differences.

Structural differences between **CEP.5.4** and **CEP.5.3** were attributed, as mentioned previously, to the lower concentration of PEG within the initial spinning solution causing thick cylinders of PDI to be spun which appeared to have inhibited discrete fibre formation, or prevented formations of accessible surfaces. Similarly, there is a slight H3 hysteresis which was again related to the simulated macroporosity caused by entangled fibre formation. An increase in measured surface area may be possible by reducing the sizes of the initial fibre formation, thereby reducing how much entanglement can occur, and freeing up more available surface.

5.3.3 Cyclic Voltammetry

As stated above, a three electrode system was used to study current as a function of applied potential. While the working electrode applied the potential to the electrolyte, a second, platinum, electrode was used as the other half of the cell which balanced the charge added or removed by the working electrode. A two-electrode system, however struggles with maintaining a constant potential while also passing current to the working electrode. As a result, a silver/silver chloride reference electrode with a known potential (-0.197 V) was employed allowing the counter electrode to solely provide electrons with no current flowing through it.[34,35]

The electrolytes used were aqueous based owing to environmental concerns. Three primary electrolytes were used to reduce solution resistance; neutral, sodium sulfate (1 M), alkali, potassium hydroxide (1 M), and acidic, sulfuric acid (1 M). Owing to the limited potential window of aqueous electrolytes without causing the electrolysis of water, the potential window used was limited to 1.2 V between -0.6 – 0.6 V, unless stated otherwise (**Table 5.5**).

The specific capacitance, C_{sp}, of each sample was calculated using the following equation:

$$C_{sp} = \frac{\int IdV}{\Delta V.v.m} \quad (1)$$

In which I relates to current, ΔV is the potential window, v is the scan rate, and m is the mass. Practically, from the cyclic voltammetry curve, the area underneath the current voltage curve is calculated using the average between consecutive specific current values and the difference between consecutive potential values. For the duration of the voltage window in a positive and negative scan direction, an average value of the total area is recorded and divided by the voltage window, giving the capacitance in $F.g^{-1}$.

Table 5.5 Cyclic voltammetry of measured capacitances for samples with sweep rates and electrolytes used in a voltage window of -0.6 – 0.6 V, unless stated otherwise.

Sample	Mass of active material(g)	Electrolyte	Sweep Rate (V/s)	Capacitance (F//g)
CSP.5.1	0.00100	H_2SO_4 (1 M)	0.1	0.14
(0.0 - -0.6 V)			0.001	104.01
CSP.5.2	0.00360	Na_2SO_4 (1 M)	0.1	0.64
			0.001	13.16
	0.00225	KOH (1 M)	0.1	4.39
			0.001	20.01
CSP.5.3	0.00288	Na_2SO_4 (1 M)	0.1	1.04
			0.001	51.02
	0.00225	KOH (1 M)	0.1	1.51
			0.001	14.97
	0.00225	H_2SO_4 (1M)	0.1	1.75
			0.001	247.06
CEP.5.1	0.00378	H_2SO_4 (1 M)	0.1	19.33
(0.0 - 0.9 V)				
CEP.5.2	0.00100	H_2SO_4 (1 M)	0.1	33.98
			0.001	350.85
CEP.5.3	0.00153	Na_2SO_4 (1 M)	0.1	7.58
			0.001	64.48
	0.00144	KOH (1 M)	0.1	8.38
			0.001	34.46
	0.00171	H_2SO_4 (1 M)	0.1	4.76
			0.001	426.82
CEP.5.4	0.00378	Na_2SO_4 (1 M)	0.1	2.49
			0.001	25.54

Using a voltage window of -0.6 – 0.6 V, samples were cycled through six times to allow for the electrode to stabilise. Ideal EDLC behaviour of an electrode is expressed in voltammetry by a rectangular shape, where the sign of the current is immediately reversed upon application of the opposite potential sweep. However, materials displaying

pseudocapacitance properties show less of a rectangular shape and can display redox peaks.

Capacitance values for **CSP.5.1** were 104.01 $F.g^{-1}$ for the slowest scan rate used (0.001 $V.s^{-1}$) which was attributed to the fused nature of the fibres observed inhibiting the amount of Helmholtz double layer able to be formed. **CSP.5.2** demonstrated very little ordered morphology after carbonisation, despite the presence of some graphene oxide. It was speculated though that the surface of the material would display some promising graphitic behaviour, though the calculated capacitance values did not reflect this.

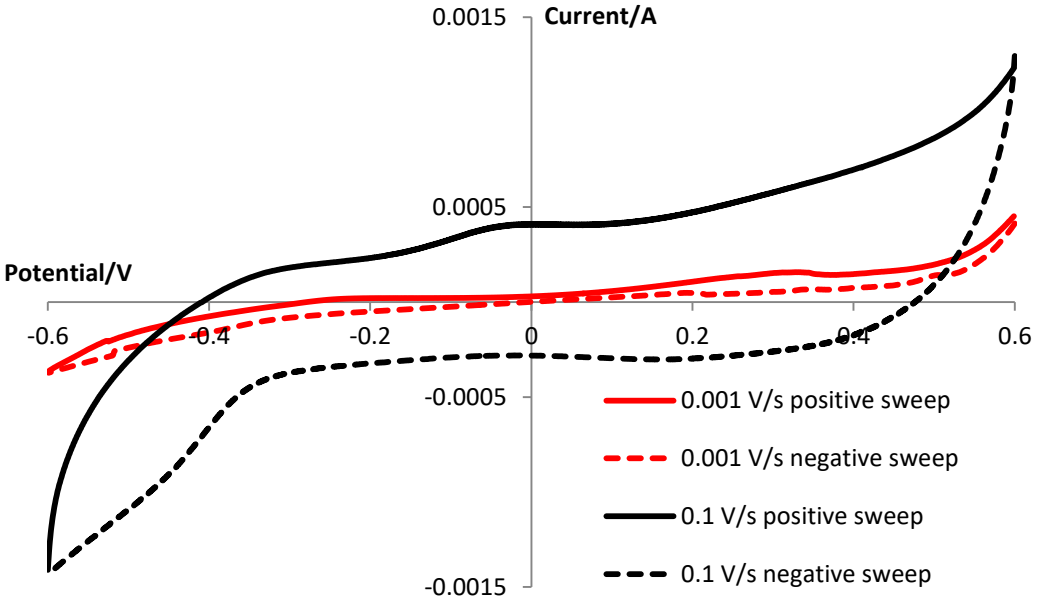

Figure 5.8 Cyclic voltammetry current/voltage curve of sample **CSP.5.3** in 1 M aqueous KOH at scan rates 0.001 (red) and 0.1 $V.s^{-1}$ (black).

The shape of the curve in **Figure 5.8** demonstrates relatively rapid charging with the change in potential sweep direction which is indicative of EDLC behaviour. With the more rapid sweep rate, there is a further current increase at the extreme measured potentials indicating a limiting pore structure which slows charge/discharge kinetics by impeding ion transport.[36,37] These large observed current inflections are predictably decreased when using a slower sweep rate which was due to a reduction of diffusion as the limiting factor.

Fast sweep rates lead to a decrease in the size of the diffusion layer resulting in higher current values. Slower sweep rates provide higher capacitance values, due to the system having more time to respond to the changes in potential.

As primary amines were used in the N-substitution of PTCDA, it was speculated that there was a presence of pyridinic Nitrogen in PDI which remained in the carbonised samples which could lead to a pseudocapacitance-type response. Indeed, CHNS analysis (**Appendix Table A.3.1**) revealed a 2.07% nitrogen presence after carbonisation. As mentioned in section **5.3.1**, a higher degree of disorder present in self-assembled samples could be due to the presence of non-ordered PDI aggregates present despite washing.

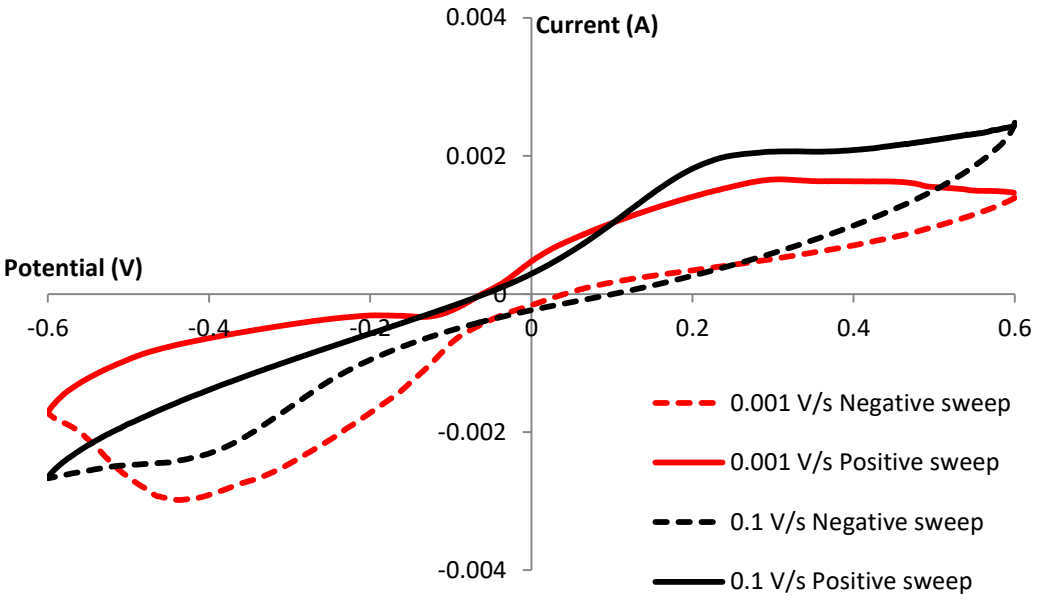

Figure 5.9 Cyclic voltammetry current/voltage curve of sample **CSP.5.3** in 1 M aqueous H_2SO_4 at scan rates 0.001 (red) and 0.1 $V.s^{-1}$ (black).

As can be seen from **Figure 5.9** (redox peak), the specific capacitance of the supercapacitor is composed of EDLC and pseudocapacitance in acid solution. The pseudocapacitance may be attributed to redox reactions of rich N, O functional groups in the electrode. Both N and O could be from the starting materials. The same is observed in **Figure 5.12**.

With a factor of 100 decrease in scan rate, the corresponding capacitance for **CSP.5.3** increased by a factor of ~140 when using sulfuric acid as an electrolyte rather than potassium hydroxide. This was attributed to sulphuric acid being more conductive at the same concentrations in water. A more conductive electrolyte decreases the diffusion limiting factor in potential sweeps, which affects pseudocapacitive interactions. A similar relationship has been observed for the different electrolytes with each sample. The shape of the curve however is more reminiscent of redox reactions occurring using cyclic voltammetry. The characteristic EDLC rapid switching of current is not present with a reverse in potential sweep direction.

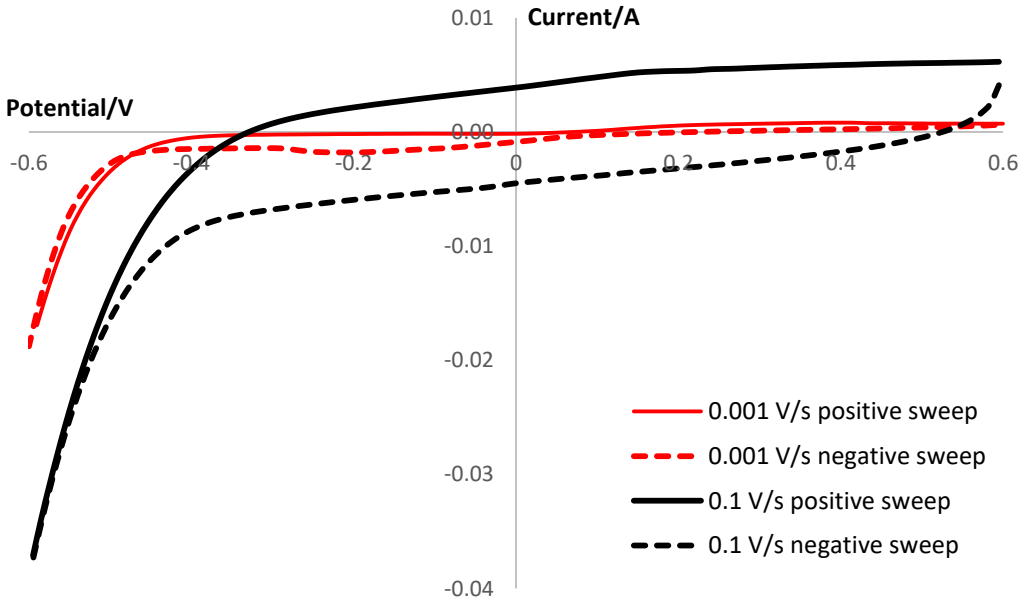

Figure 5.10 Cyclic voltammetry current/voltage curve of sample **CEP.5.2** in 1 M aqueous H_2SO_4 at scan rates 0.001 (red) and 0.1 $V.s^{-1}$ (black).

Figure 5.10 describes the behaviour of sample **CEP.5.2** between -0.6 – 0.6 V and shows more typical EDLC behaviour with a more rectangular curve shape. This shows almost immediate switching of the current with a reversed potential sweep which demonstrates solely ion adsorption at the electrode-electrolyte interface. At a more negative applied potential, the current increases in magnitude rapidly until the switching potential is

reached and the current reverses. Sample **CEP.5.1** showed lower capacitance for the scan rate 0.1 V.s^{-1} (Appendix Figure A.3.4) with a curve shape more reminiscent of EDLC behaviour, though the low capacitance was attributed to greater resistivity of the material.

At lower scan rates there was no clear demonstration of redox potential or other pseudocapacitive behaviour which is evidence that this material contains minimal PDI but rather is a majority PAN electrospun and carbonised material.

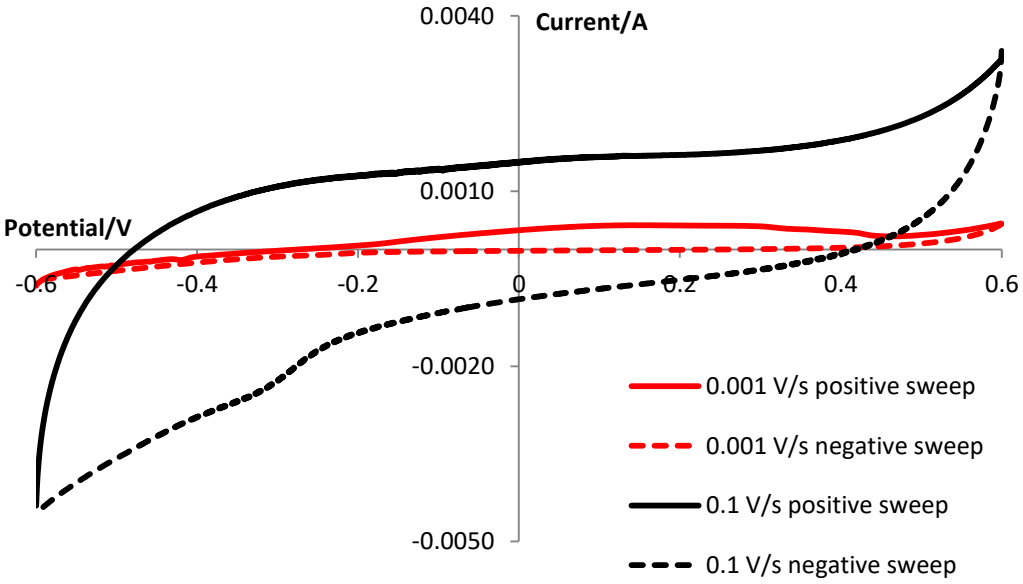

Figure 5.11 Cyclic voltammetry current/voltage curve of sample **CEP.5.3** in 1 M aqueous KOH at scan rates 0.001 (red) and 0.1 V.s^{-1} (black).

As stated in **Table 5.5**, sample **CEP.5.3** was measured using an alkali electrolyte solution. **Figure 5.11** shows delayed switching of current was observed with changing potential sweep direction for a fast scan rate. The slanted shape rather than a flat rectangle was attributed to resistivity in the material common with pseudofaradaic reactions. The delayed response after switching the potential sweep rate was connected to the slow kinetic process involved in charging the capacitance.[4]

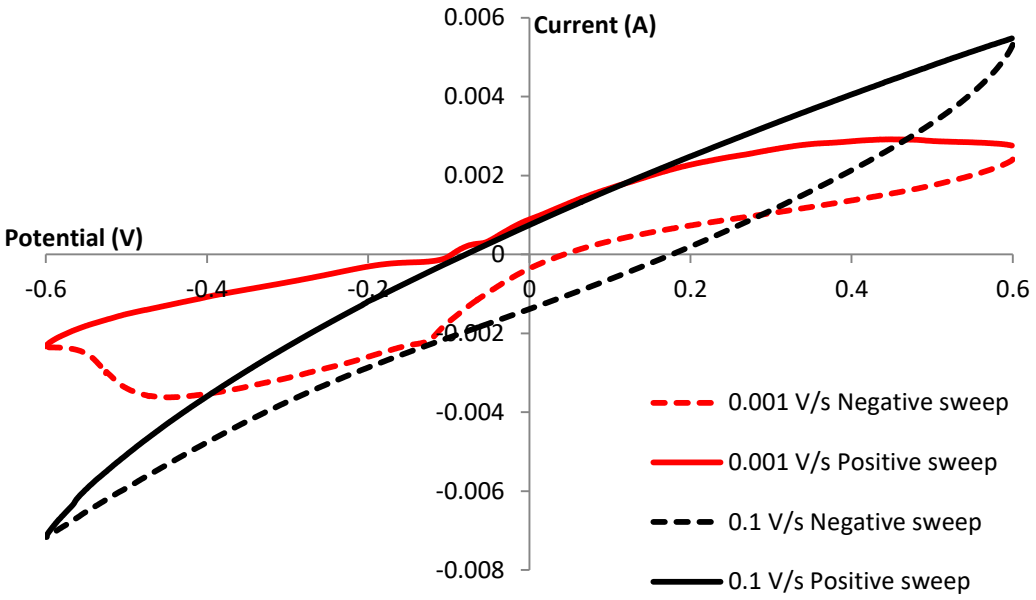

Figure 5.12 Cyclic voltammetry current/voltage curve of sample **CEP.5.3** in 1 M aqueous H_2SO_4 at scan rates 0.001 (red) and 0.1 $V.s^{-1}$ (black).

For sample **CEP.5.3** acidic electrolyte did not present with the traditional EDLC voltammetry behaviour (**Figure 5.12**) however there was also no clearly defined redox peaks. The shape of the curve was a result of a material with high resistivity resulting in a slanted curve rather than a more defined rectangular shape of a true EDLC. With a slower sweep rate, there appears more defined redox activity reminiscent of sample **CSP.5.3** which is consistent with two PDI-based materials.

5.3.4 Li-ion Battery Testing

As a final test to see if there was a more appropriate application as a battery electrode material was to deposit the CNFs onto a copper disc for placement into a lithium-ion cell. **CEP.5.3** showed good surface area and graphitic content of all previous samples, as well as possible micropore presence, and was chosen to be used as an anode material to test in a Li-ion cell.

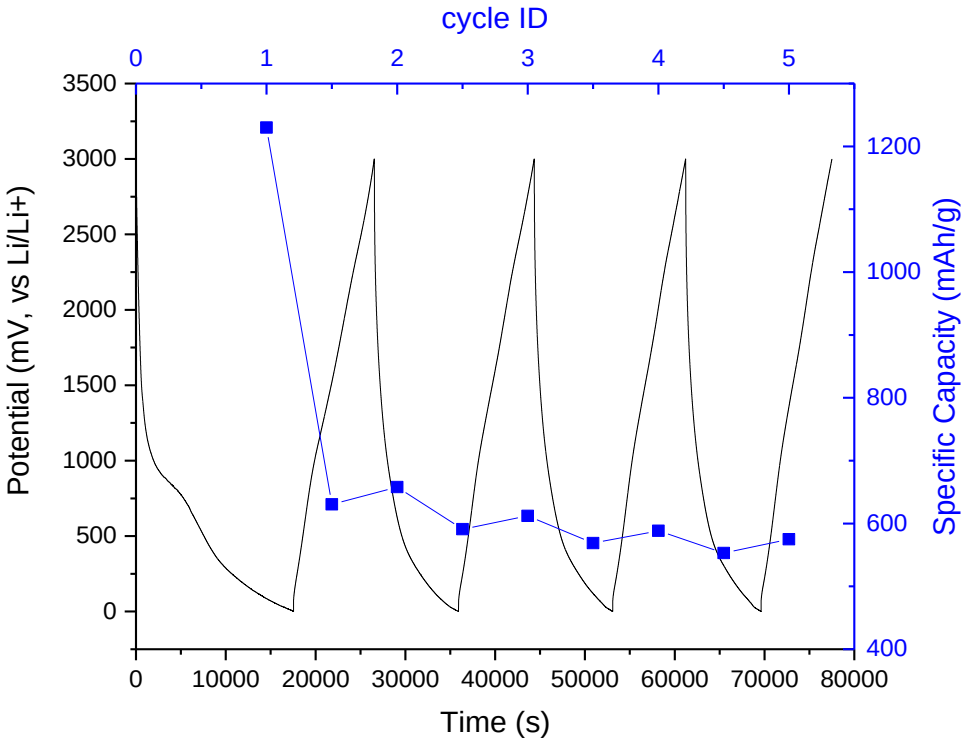

Figure 5.13 Sample **CEP.5.3** Li-ion battery cycling between 0.3 - 3000 mV (black), and capacitance recorded for each charge and discharge (blue) at 50 $mA.g^{-1}$.

Initial specific capacity was 1229.85 $mA.h.g^{-1}$ which subsequently dropped as expected to 630.53 $mA.h.g^{-1}$. Discharge capacity between cycles was slightly higher than the charging capacity due to only being able to observe the initial cycles in which the cell was still stabilising. After 6 cycles the charging capacity was 553.08 $mA.h.g^{-1}$ while the discharge capacity was 574.97 $mA.h.g^{-1}$, though further testing would be required to observe where the capacity value would stabilise.

The size of lithium ions within the context of intercalating into a carbon anode would suggest that too small pore sizes would be unfavourable towards allowing the material to store lithium ions for later reintegration with the cathode. However, the small micropores presented by the material CE063 appear able to provide space to successfully intercalate lithium ions. Further testing would be necessary to discover the material's reversibility and capacity retention at greater currents.

5.4 Conclusions

Materials presented in Chapter 3 were analysed for their potential application as electrodes in energy storage devices, primarily supercapacitors, using cyclic voltammetry. Ideal characteristics of materials were measured through Raman spectroscopy and BET surface area analysis since for a material to be effective as an electrode, graphitic content and surface area play an important role.

Self-assembled and electrospun fibres were analysed using Raman spectroscopy after carbonisation. Relative proportions of graphitic and disordered carbon were compared using Lorentzian peak fitting as well as measurements directly from the recorded spectra. For all recorded samples, a greater proportion of disordered carbon was observed with sample CEP.5.3 displaying the highest relative amount of graphitic or sp^2 carbon.

BET surface area analysis showed carbonised materials with reasonable surface areas though with minimal observable porosity. Pre-carbonised PDI fibres showed minimal energy of adsorption with a type III isotherm and hysteresis describing slit-like pores resulting from plate-stacked PDI molecules. Isotherms of carbonised materials primarily showed non-porous materials with high adsorption energy of nitrogen, though BJH desorption pore radii distribution suggested the presence of 2 nm micropores.

Cyclic voltammetry measurements were used to record capacitance values for each material in different electrolytes (alkaline, neutral, and acidic). Specific capacitance was calculated using the area under current vs potential curves at different sweep rates with maximum capacitance of 426.82 $F.g^{-1}$ for **CEP.5.3**. Materials with a measurable PDI content showed pseudocapacitive behaviour through slanted rectangular curves and a non-linear relationship between capacitance and sweep rate, as would be expected of a pure EDLC.

Sample CEP.5.3 was tested as a lithium ion battery electrode with good final capacitance of 553.08 $mA.h.g^{-1}$ after 6 cycles at 50 $mA.g^{-1}$. Further testing is necessary to determine reversibility and capacitance retention over many cycles. Overall PDI materials displayed promising characteristics of one-dimensional electrode materials and would benefit from further study into post-synthetic modification or activation to boost potential performance. Future research could explore binder-free electrodes formed through either self-assembly or electrospinning.

5.5 References

1 Y. Jiang and J. Liu, *ENERGY & ENVIRONMENTAL MATERIALS*, 2019, **2**, 30–37.

2 C. Costentin and J.-M. Savéant, *Chemical Science*, 2019, **10**, 5656–5666.

3 M. Winter and R. J. Brodd, *Chemical Reviews*, 2004, **104**, 4245–4269.

4 E. Frackowiak and F. Béguin, *Carbon*, 2001, **39**, 937–950.

5 S. R. S. Prabaharan, R. Vimala and Z. Zainal, *Journal of Power Sources*, 2006, **161**, 730–736.

6 S. Zhou, X. Li, Z. Wang, H. Guo and W. Peng, *Transactions of Nonferrous Metals Society of China*, 2007, **17**, 1328–1333.

7 E. Frackowiak, *Physical Chemistry Chemical Physics*, 2007, **9**, 1774–1785.

8 Y. Zhai, Y. Dou, D. Zhao, P. F. Fulvio, R. T. Mayes and S. Dai, *Advanced Materials*, 2011, **23**, 4828–4850.

9 X. Lu, C. Wang, F. Favier and N. Pinna, *Advanced Energy Materials*, 2017, **7**, 1601301.

10 C. Huang, S. Barlow and S. R. Marder, *The Journal of Organic Chemistry*, 2011, **76**,

2386–2407.

11 W. Herbst, K. Hunger, G. Wilker, H. Ohleier and R. Winter, *Industrial Organic Pigments*, Wiley, 3rd Ed., 2004.

12 M. Greene, in *High Performance Pigments*, Wiley-VCH Verlag GmbH & Co. KGaA, Weinheim, Germany, 2009, pp. 261–274.

13 K. Hunger and W. Herbst, in *Ullmann's Encyclopedia of Industrial Chemistry*, Wiley-VCH Verlag GmbH & Co. KGaA, Weinheim, Germany, 2000, pp. 379–423.

14 F. Würthner, *Chemical Communications*, 2004, **14**, 1564–1579.

15 K. Balakrishnan, A. Datar, T. Naddo, J. Huang, R. Oitker, M. Yen, J. Zhao and L. Zang, *Journal of the American Chemical Society*, 2006, **128**, 7390–7398.

16 G. Boobalan, P. K. M. M. Imran, C. Manoharan and S. Nagarajan, *J. Colloid Interface Sci.*, 2013, **393**, 377–383.

17 T. Guner, E. Aksoy, M. M. Demir and C. Varlikli, *Dyes and Pigments*, 2019, **160**, 501–508.

18 M. Z. Ongun, K. Ertekin, S. Nadeem and O. Birel, *Journal of Fluorescence*, 2016, **26**, 2311–2320.

19 A. Kayyar, J. Huang, M. Samiee and J. Luo, *Journal of Visualized Experiments*, 2012, **e4104**, 1–5.

20 S. Wang, L. Yang, L. P. Stubbs, X. Li and C. He, *ACS Applied Materials & Interfaces*, 2013, **5**, 12275–12282.

21 D. Lin-Vien, N. B. Colthup, W. G. Fateley and J. G. (Professor) Grasselli, *The Handbook of infrared and raman characteristic frequencies of organic molecules*,

Academic Press, 1991.

22 A. Sadezky, H. Muckenhuber, H. Grothe, R. Niessner and U. Pöschl, *Carbon*, 2005, **43**, 1731–1742.

23 N. B. Colthup, L. H. Daly and S. E. Wiberley, *Introduction to infrared and Raman spectroscopy*, Academic Press, 1975.

24 F. Tuinstra and J. L. Koenig, *The Journal of Chemical Physics*, 1970, **53**, 1126–1130.

25 I. Childres, L. A. Jauregui, W. Park, H. Cao and Y. P. Chen, *RAMAN SPECTROSCOPY OF GRAPHENE AND RELATED MATERIALS*, .

26 A. Fernández, P. Peretyagin, W. Solís, R. Torrecillas and A. Borrell, *Journal of Nanomaterials*, 2015, **2015**, 1–7.

27 S. Peng, L. Li, J. Kong Yoong Lee, L. Tian, M. Srinivasan, S. Adams and S. Ramakrishna, *Nano Energy*, 2016, **22**, 361–395.

28 H. M. Jeong, J. W. Lee, W. H. Shin, Y. J. Choi, H. J. Shin, J. K. Kang and J. W. Choi, *Nano Letters*, 2011, **11**, 2472–2477.

29 A. V. Melechko, V. I. Merkulov, T. E. McKnight, M. A. Guillorn, K. L. Klein, D. H. Lowndes and M. L. Simpson, *Journal of Applied Physics*, 2005, **97**, 41301.

30 Y. Wang, D. C. Alsmeyer and R. L. Mccreery, *Raman Spectroscopy of Carbon Materials: Structural Basis of Observed Spectra*, 1990, vol. 2.

31 A. Daraghmeh, S. Hussain, I. Saadeddin, L. Servera, E. Xuriguera, A. Cornet and A. Cirera, *Nanoscale Research Letters*, 2017, **12**, 639.

32 J. B. Condon, in *Surface Area and Porosity Determinations by Physisorption*, Elsevier, 2020, pp. 1–57.

33 M. Thommes, K. Kaneko, A. V. Neimark, J. P. Olivier, F. Rodriguez-Reinoso, J. Rouquerol and K. S. W. Sing, *Pure and Applied Chemistry*, 2015, **87**, 1051–1069.

34 T. J. Smith and K. J. Stevenson, in *Handbook of Electrochemistry*, Elsevier, 2007, pp. 73–110.

35 B. N. Popov, in *Corrosion Engineering*, Elsevier, 2015, pp. 29–92.

36 M. E. Suss, T. F. Baumann, M. A. Worsley, K. A. Rose, T. F. Jaramillo, M. Stadermann and J. G. Santiago, *Journal of Power Sources*, 2013, **241**, 266–273.

37 C. N. Satterfield, C. K. Colton and W. H. Pitcher, *AIChE Journal*, 1973, **19**, 628–635.

Chapter 6 Conclusions

In this thesis, the synthesis and characterisation of perylene-3,4,9,10-tetracarboxylic diimide-N,N'-isophthalic acid (PDI) was demonstrated as well as the production of carbon nanofibres from self-assembled PDI. The aims of the project were to provide a PDI molecule capable of controlled self-assembly into nanofibres using aqueous conditions. The formed nanofibres were to be capable of withstanding carbonisation treatment into carbon nanofibres, which could then be applied and tested as electrode materials in supercapacitors. Without assembling PDI, the fluorescence of the molecule was also to be exploited for potential sensing applications.

In chapter 3, PDI self-assembly was explored through two major methods, solution-based self-assembly through pH-triggering and interfacial assembly, and also electrospinning which mimicked evaporation-triggered self-assembly. Slow pH transition from pH 11 – pH 6 using a combination of weak base (imidazole) and weak acid (glucono-δ-lactone) was found to be the most effective in forming one-dimensional nanofibres. Washing fibres formed through self-assembly proved necessary to remove residual imidazole from the material to preserve structure after carbonisation, though this proved unnecessary with electrospinning. By using a carrier polymer, polyethylene glycol, PDI could be electrospun in an aqueous solution containing imidazole for solubility, and yet retain its structure after carbonisation, without additional washing of the initial electrospun fibres. This shows the first aim of the project was successful and CNFs were produced from self-assembled and electrospun PDI molecules, but further research could be conducted to incorporate functional materials such as metal ions or other active species.

Chapter 4 presented PDI as an aqueous solution-based turn-off sensor for metal ion sensing using optical spectroscopy. Initial fluorescent measurements displayed a large signal-to-

noise ratio which inhibited precise measurements from being recorded, though UV-Vis spectroscopy was capable of measuring the progressive quenching of PDI with additions of metal ion solutions. PDI solution was able to measure concentration of metal ions in solution, though the accuracy of these measurements appeared to be dependent on the counter ions used with the metal, in that dissociation played a role in the speed at which peak absorption was affected. The range of metal concentration capable of being measured was recorded as well as a unique, identifying peak position formed by PDI after sufficient metal addition. This identifying peak position was established for metal ions: Ti^{3+}, $Fe^{2+/3+}$, Co^{2+}, Cu^{2+}, and Zn^{2+} in aqueous solutions. Further research is required to test the reversibility and reliability of the suggested sensor.

CNFs produced in Chapter 3 were tested in Chapter 5 for their applications as electrode materials. Characterisation of CNFs was conducted using BET analysis and Raman spectroscopy to evaluate potentially attractive qualities in produced materials before cyclic voltammetry was used to calculate specific capacitances of materials in an alkaline, neutral, and acidic electrolyte. CNFs showed a non-linear relationship between capacitance and scan rate within a potential window which was not due to pure EDLC and instead demonstrated some pseudocapacitive behaviour. A maximum capacitance of 426.82 $F.g^{-1}$ was recorded at 1 $mV.s^{-1}$ in acidic pH. The same material also demonstrated a promising capacitance of 553.08 $mA.h.g^{-1}$ when used as the anode in an assembled Li-ion battery cell. Further research would be required to improve materials surface areas to capitalise upon a pseudocapacitive response, while additional research would be recommended into potential Li-ion battery applications, including cycling stability.

Overall, thesis aims laid out in Chapter 1 were achieved with varying degrees of success. This preliminary research could be expanded upon using alternative PDI molecules to achieve different sensing responses, or fibrous structures. Additionally, modifications after

fibre production and carbonisation could be explored including impregnation with metal ions or other dopants to increase activity and etching to increase surface and attach functional surface groups. PDI is particularly interesting due to its high level of tunability which can affect its many potential applications.

Appendix A Appendix

A.1 Self-Assembly and Electrospinning of Perylene Diimide Derived Carbon Nanofibres

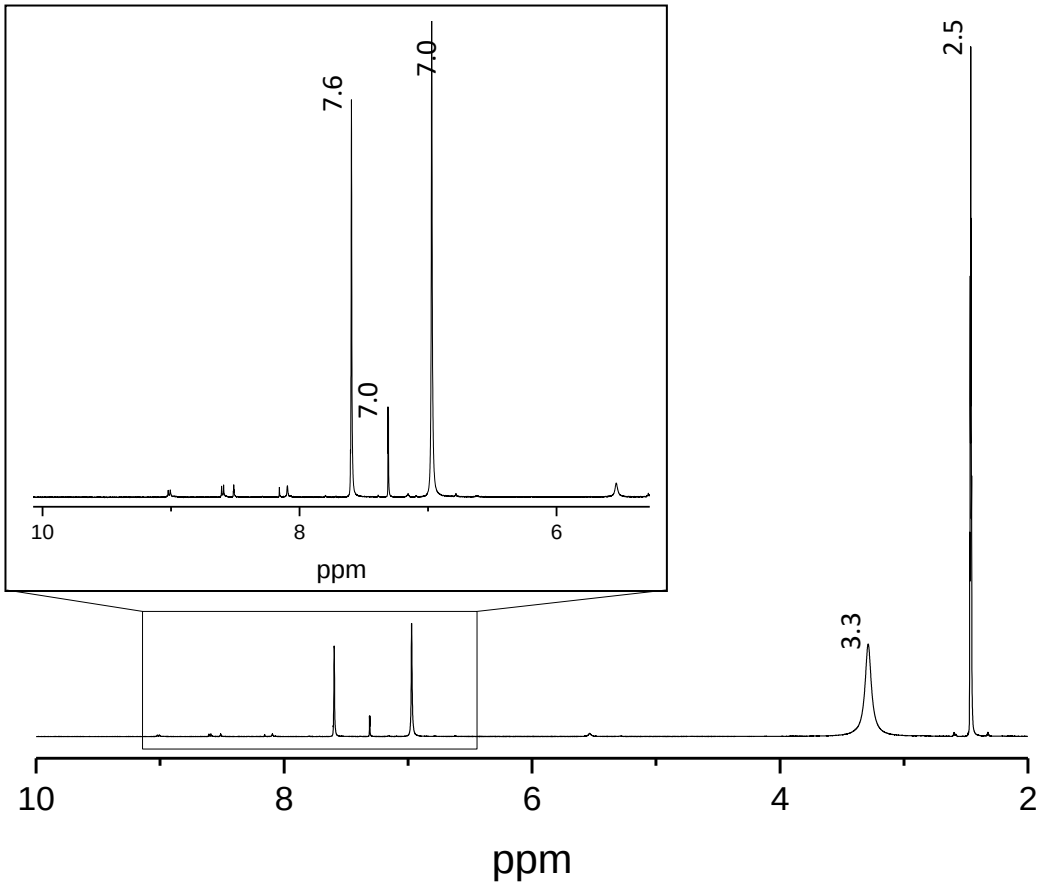

Figure A.1 1H NMR of impure PDI after only washing with ethanol after synthesis

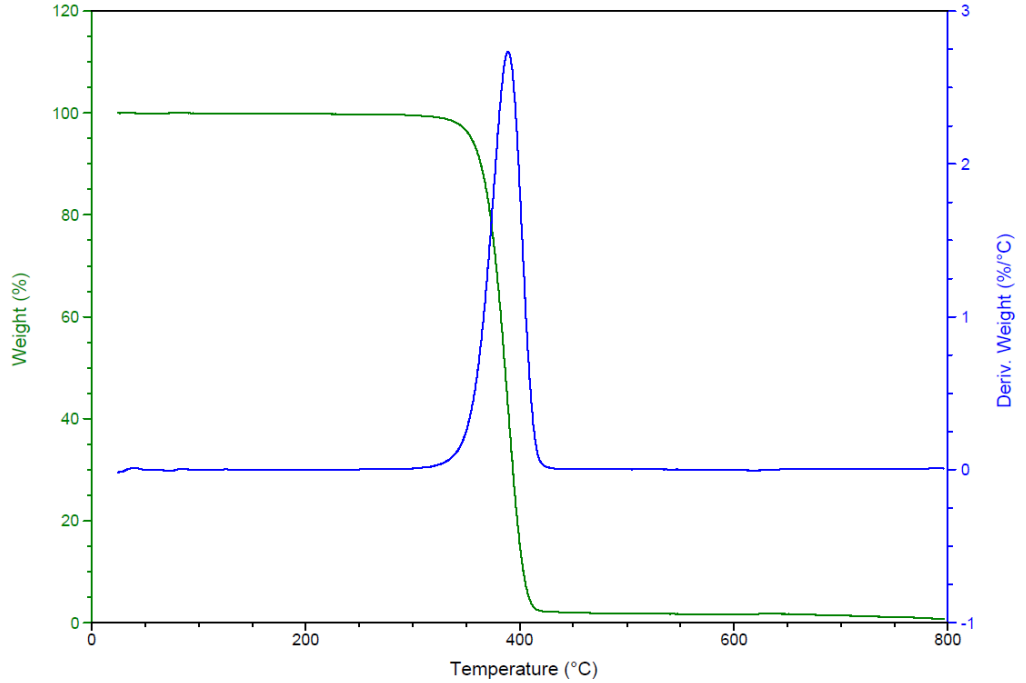

Figure A.2 Thermogravimmetric analysis graph of thermal decomposition of Poly(ethylene) glycol MW 400 000 g.mol-1 in nitrogen atmosphere

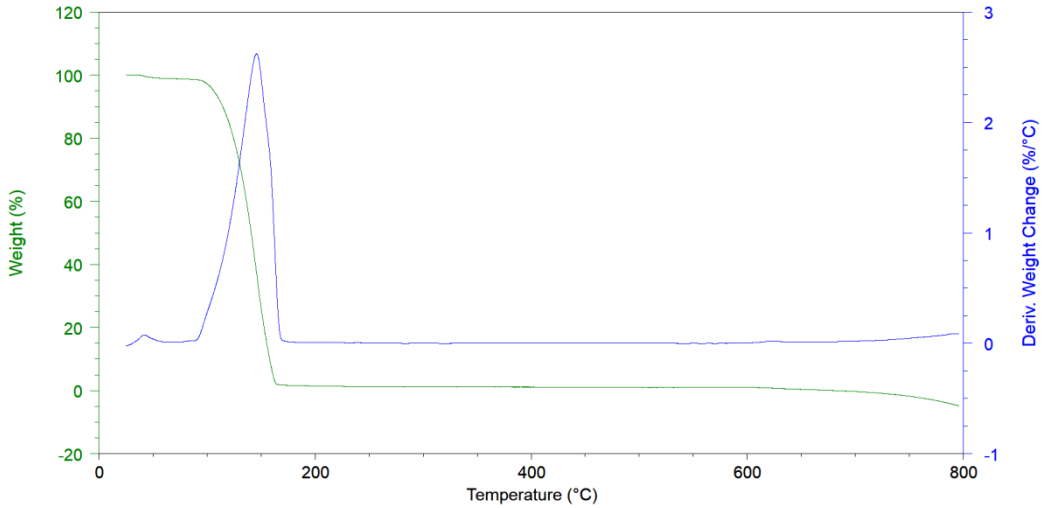

Figure A.3 TGA graph of thermal decomposition of imidazole in nitrogen atmosphere

A.2 Perylene Diimide Solutions Used for Low-Concentration Metal Ion Sensing Using Low-Cost UV-Vis Spectroscopy

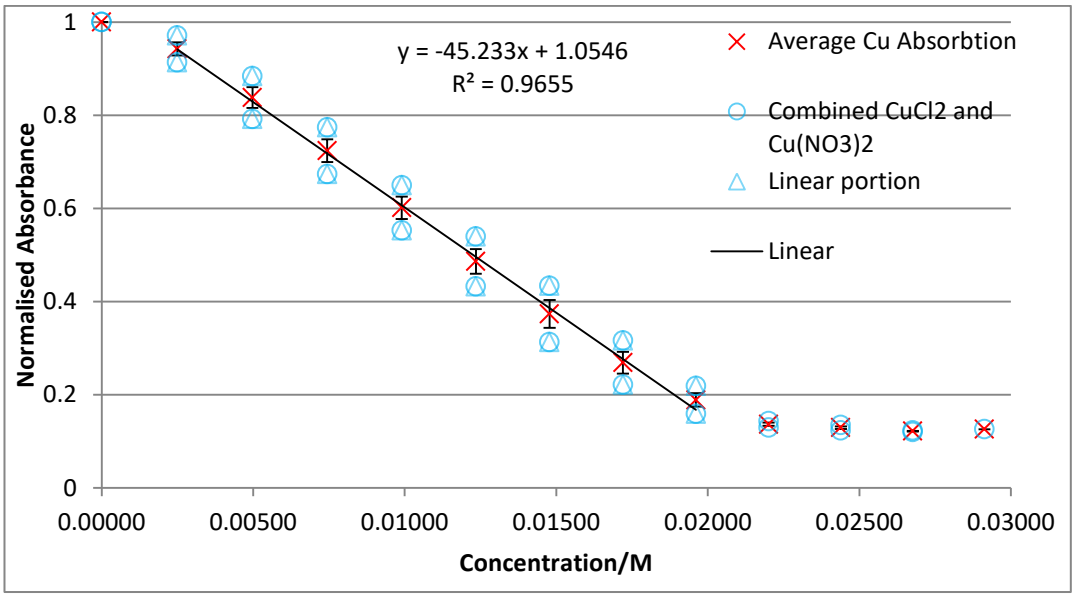

Figure A.4 Graph of normalised absorbance vs concentration for $CuCl_2$ and $Cu(NO_3)_2$.

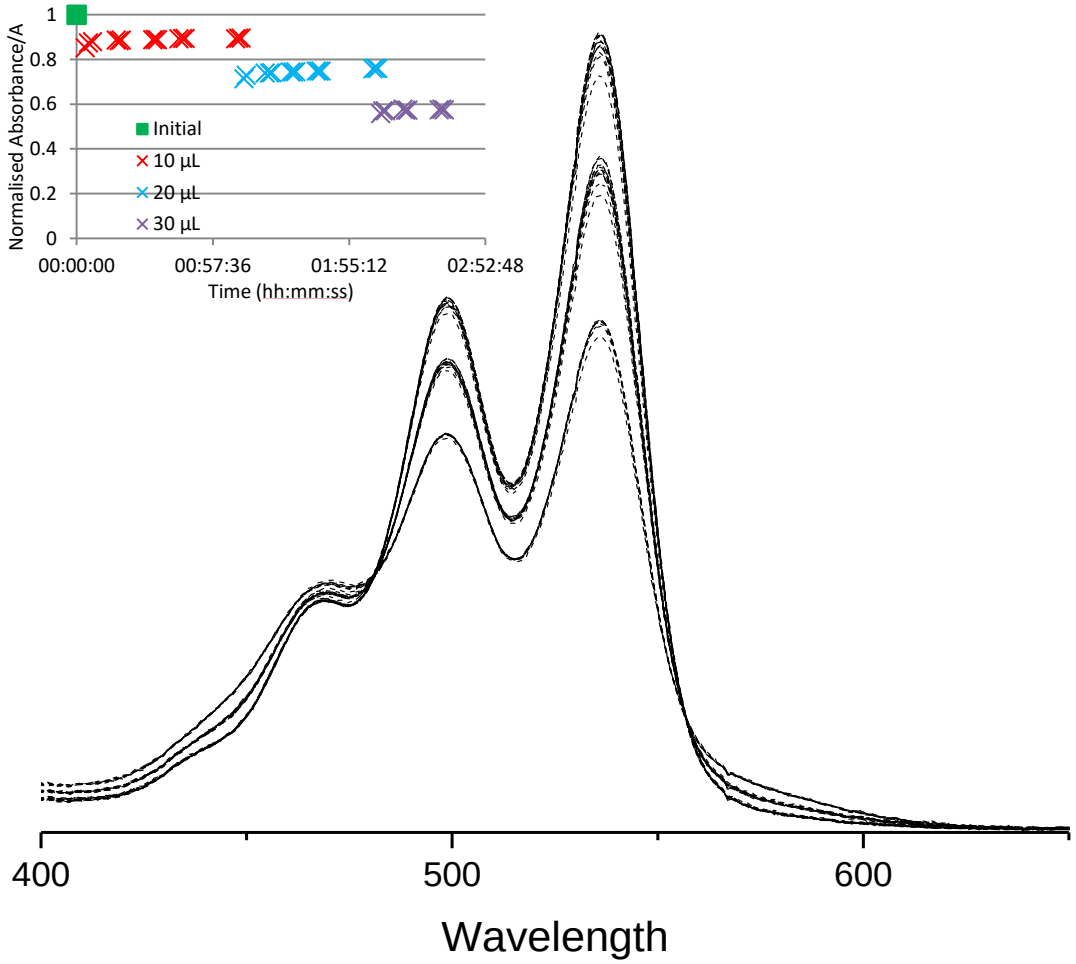

Figure A.5 Iron (II) nitrate additions (1 µM, 10 µL) to PDI solution with measurements over time graph (inset)

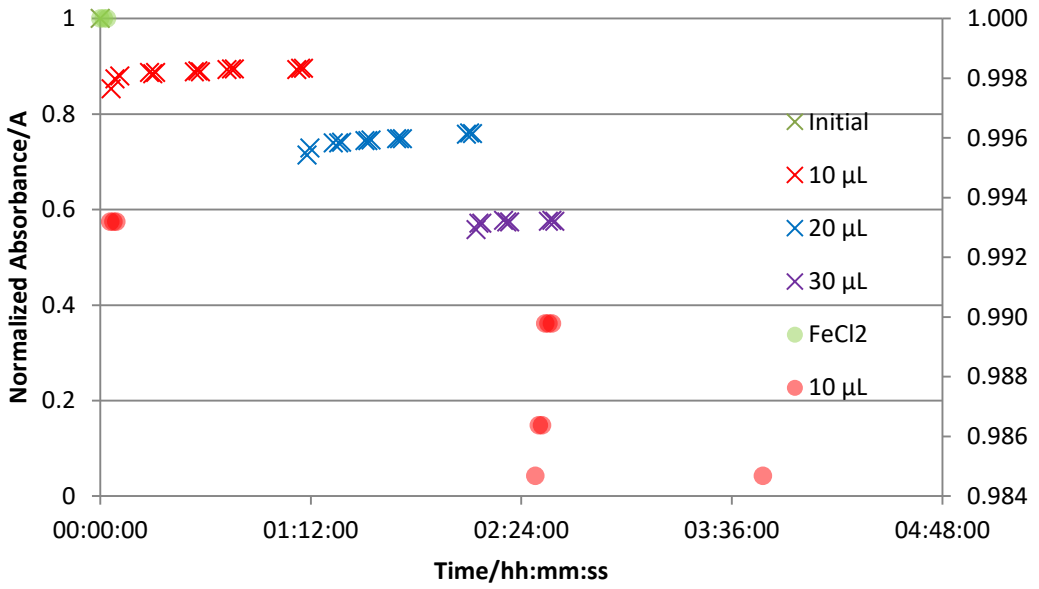

Figure A.6 Graph of Absorbance at 536 nm with additions of $Fe(NO_3)_2$ or $FeCl_2$ in 1 µM, 10 µL increments with spectra recorded over time.

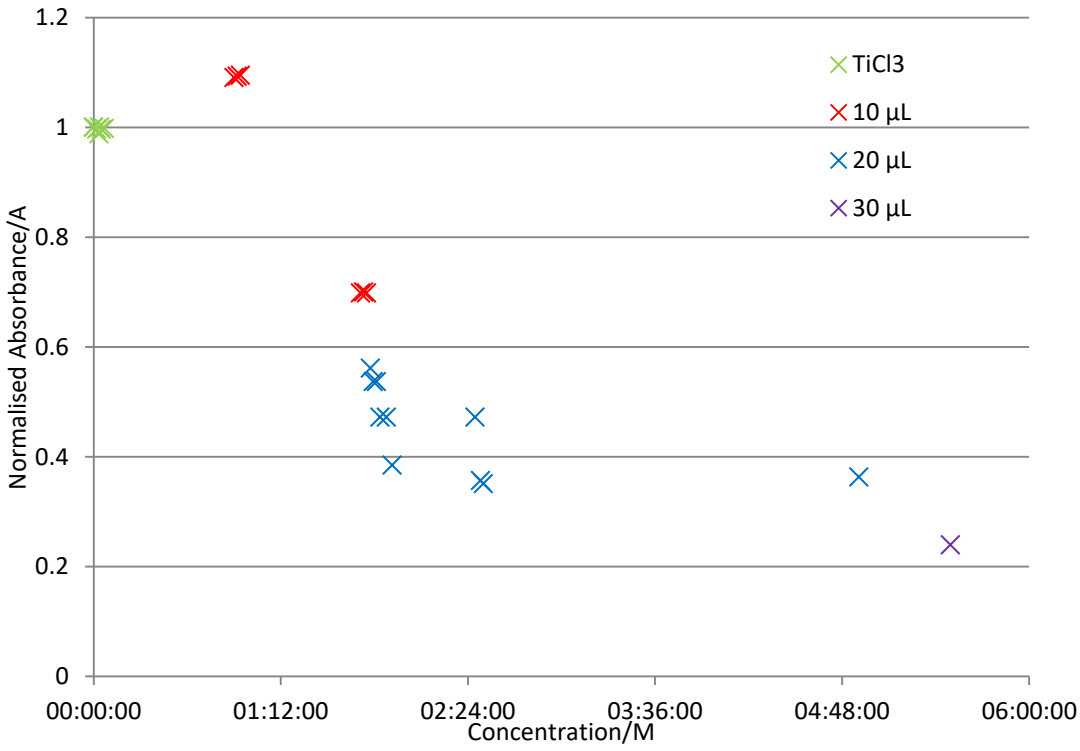

Figure A.7 Graph of absorbance at 536 nm with additions of $TiCl_3$ in 1 µM, 10 µL increments with spectra recorded over time.

A.3 Perylene Diimide Derived Nanofibres as Electrode Materials

Table A.3.1 Table of CHN values measured by elemental analysis

Sample	% Carbon	% Nitrogen	% Hydrogen
PDI	88.65	7.15	4.18
SP.5.3	91.68	3.06	2.07
EP.5.3	94.42	4.29	1.30
EP.5.4	92.54	4.64	2.82

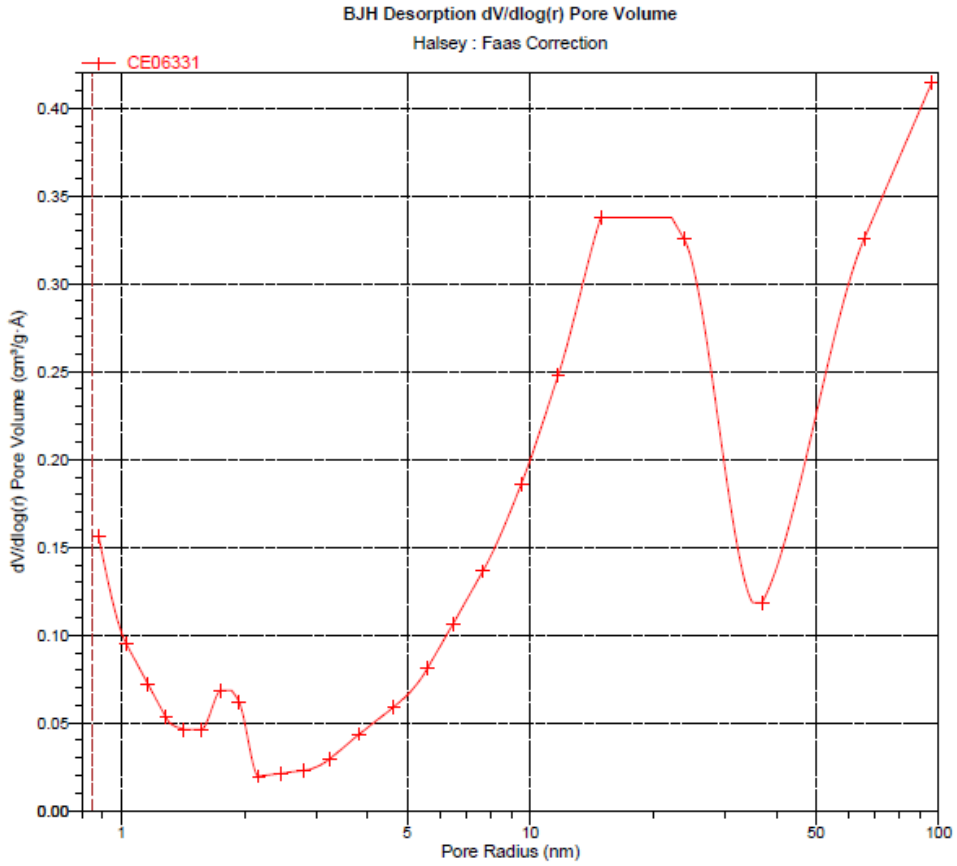

Figure A.8 Graph of BJH desorption pore volumes at measured radii.

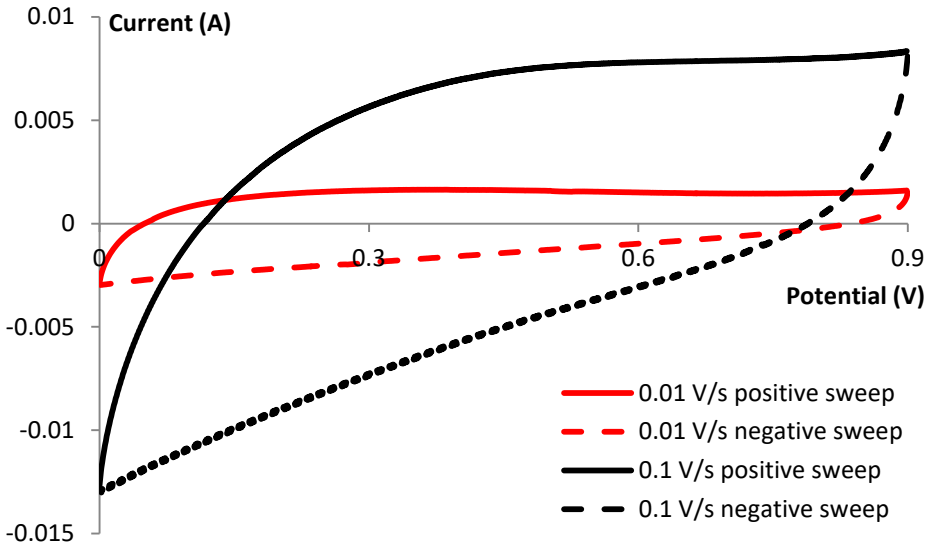

Figure A.9 Cyclic voltammetry of EP.5.1 between 0.0 - 0.9 V